



Faculty of Science and Technology

BACHELOR THESIS

Study program:	Spring semester 2024
Bachelor in Mechanical Engineering	<u>Open</u> or Confidential
Author(s): Stian Kornberg Oskar Samuelsson Caspar Aarlie	
Subject manager: Dimitrios Pavlou Supervisor(s): Dimitrios Pavlou, Adugna Deressa Akessa	
Title of thesis: Rocket Fuselage Development using Composite Filament Winding Technology	
Study points: 20	
Subject words: Rocket, Composite materials, Manufacturing, Filament winding, FEA	Number of pages: 75 + attachments: 27 Stavanger, May 14, 2024

Contents

Acknowledgements	iv
Abstract	v
Abbreviations	vi
1 Background	1
1.1 About UiS Aerospace	2
1.1.1 Core Values	3
1.2 The Borealis Program	4
1.2.1 Previous launch	5
1.2.2 Overarching goals for this years launch	6
1.3 Explanation of functions on Borealis II	6
1.3.1 Outer Components	7
1.3.2 Inner components	8
1.4 Launch Rail	9
2 Introduction	10
2.1 Project Description	11
2.2 Justification for the Thesis	11
2.2.1 Glass fiber	11
2.2.2 Process of Filament Winding Production	11
2.3 Project Specifications	12
2.4 Structure of the report	12
3 Basic Theory	13
3.1 Mechanics of Composite Materials	14
3.1.1 Step-by-Step Optimal Angle Analysis	15
3.1.2 Generalization of Hooke's law	15
3.1.3 Plate Theory Simplification	16
3.1.4 Transformation Matrix	18
3.1.5 Classical Lamination Theory	19
3.1.6 Kirchhoff Isotropic Plate Theory	20
3.1.7 ABD-matrix	22
3.1.8 Boundary Conditions due to Dynamic Pressure	23
3.1.9 Tsai-Wu Failure Criterion	23
3.2 Dynamic Pressure	25

4	Mandrel	26
4.1	Design	27
4.1.1	Dimensions of mandrel components	29
4.2	Failure Analysis	29
4.2.1	Extraction tool failure analysis	29
4.2.2	FEA of the Mandrel	30
5	Filament Winding	32
5.1	Understanding Filament Winding	33
5.2	Winding Machine	34
5.2.1	Spool Creel	34
5.2.2	Carriage Unit	34
5.2.3	Collection Assembly Platform	35
5.3	CADWIND	36
5.3.1	Mandrel Creation	36
5.3.2	iWind	37
6	Fiber Angle Optimization	40
6.1	Calculating Max Q using OpenRocket	41
6.2	Python Code for Optimal Angle Determination	42
6.2.1	Explaining the code	42
6.3	The Calculated Values	48
6.4	Manufacturing consideration	49
6.5	Angle Determination	49
7	Structural Analysis	51
7.1	Step by Step Utilizing Ansys Workbench	52
7.1.1	ACP(pre)	52
7.1.2	Static Structural	53
7.1.3	ACP(post)	53
7.2	FEA on the Fuselage	54
7.2.1	Failure Analysis	54
7.2.2	Deformation Analysis	54
7.3	Addressing the Assumptions	55
8	Manufacturing	56
8.1	Setup	57
8.1.1	Changes to the Angle	57
8.2	Winding	58
8.2.1	Dry Winding	58
8.2.2	Wet winding	59
8.3	Hardening	59
8.4	Extraction	60
8.5	Preparation	61
9	Results	62
9.1	Testing	63
9.2	Launch day	63
9.3	Results from launch	66
9.3.1	Dynamic Pressure from collected data	67

10 Discussion and Conclusion	68
10.1 Production Process & Filament Winding	69
10.1.1 Production process	69
10.1.2 Filament Winding & Mandrel Use	69
10.2 The Fuselage	70
10.2.1 Geometry	70
10.2.2 Structural integrity	70
10.2.3 Practicality	70
11 Further Work	71
11.1 Nose cone	72
11.2 Multiple layers/fiber angles	72
11.3 Panels in the fuselage	73
Bibliography	74
A Tables	76
B Python Code	79
C Technical Drawings	86
D Equations	91
D.1 Engineering Constants	92
D.2 Material constants	92
D.3 Strain Transformation	93
D.4 Inverse Transformation Matrix	94
D.5 Strain-displacement relations	94
E Calculations	95
E.1 Reaction Forces	96
E.2 Deflection	96
E.3 Welds	101
E.4 Tensile capacity of the extraction tool bolts	102

Acknowledgements

We are deeply grateful to all those who have supported and inspired us throughout the journey of completing this thesis. Their guidance, encouragement, and unwavering support have been invaluable and have contributed significantly to the completion of this work.

Firstly, a big thank you to our supervisors, Dimitrios Pavlou and Adugna Deressa Akessa, for all the invaluable help with the theory and general structure of the project.

Secondly, we would like to thank [OPS Composite Solutions](#). From the start they have aided us with everything we needed to know about the filament winding process, lending us their time and resources, and providing essential assistance in winding the fuselage at their facility in Kristiansand. We also extend our heartfelt gratitude to the skilled technicians at their facility, who provided significant help and expertise, throughout the visit.

The Faculty of Science and Technology, and the workshop personnel at UiS has helped us tremendously throughout not just this thesis, but for UiS Aerospace as a whole. They deserve all the best, and are the reason why we can do all the incredible things we do. Thank you so much for supporting us!

We would also like to thank [Material](#) for sponsoring us with the CADWIND software, making the filament winding process possible.

Additionally, we also express our appreciation to the sponsors of [UiS Aerospace](#).

Lastly, we would like to give special thanks to those individuals that have stood out for their remarkable assistance: Emil Mannes Surnevik (UiS workshop), Christopher William Rydland Hovdan (UiS workshop), Sebastian Dobler Hamre (OPS), Kjetil Sevenius (OPS), Daniel Cau Varming (UiS Aerospace). We're so grateful for you all.

Undertaking this research has been a privilege, and we are thankful for the opportunity to delve into our academic interests and make meaningful contributions to our field of study. The journey has been enriching and rewarding, and we look forward to applying the knowledge and skills gained as we embark on new chapters in our professional and academic lives.

Abstract

This bachelor thesis is written in collaboration with the student organization UiS Aerospace, focusing on the production of the rocket fuselage for the Borealis program. The optimal production method was determined to be a combination of glass fiber and filament winding, which became the central focus of this thesis. The combination provides exceptional weight-to-strength ratio, and the ability to transmit and receive electronic signals.

In order to produce the glass fiber fuselage, a cylindrical mandrel was required. The mandrel was designed and manufactured in-house. Once mounted on the winding machine, the mandrel undergoes rotation around its central axis, subjected to a pull force estimated at 30kg, in addition to its specific weight. The main design consideration revolves around deformation, with a maximum allowable limit set at 2-3mm deformation. To predict the deformation, a simulation was conducted using Ansys. The resulting deformation was found to be 0.88mm, which was within the acceptable range for mandrel production.

The optimal fiber angle for the anisotropic glass fiber was assessed through a structural analysis using classical lamination theory. Where the structural analysis was specifically designed against the predicted dynamic pressure, calculated using OpenRocket and Python simulations. This resulted in a graph showing that the optimal fiber angle is close to 90 degrees. This graph was compared with the manufacturing parameters, and the desired angle was found determined to be 70 degrees through the use of CADWIND. This orientation was further used in a Tsai-Wu Analysis, using Ansys, where the moment with the most dynamic pressure was used. The resulting Failure Index amounted to $FI = 0.019$, where $FI \geq 1$ defines failure. This indicated that the structural integrity of the fuselage will uphold.

Before conducting the filament winding process, some of the winding parameters were changed, resulting in a change in the fiber angle from 70 to 81 degrees. Based on the earlier simulations, it was concluded that this angle is closer to optimal, yielding a lower FI and a higher factor of safety.

The launch of Borealis II took place at Helleland Spaceport, UiS Aerospace's private launch site, on April 27th. Despite a misfire and necessary rewiring of the launch mechanism, Borealis II successfully launched, reaching an altitude of 2100 meters and a maximum velocity of 950 km/h. The parachute deployed at apogee instead of the intended 1 km height, resulting in a spike in acceleration and the loss of the aft airframe due to undersized screws. Nevertheless, the fuselage performed admirably, enduring dynamic pressure, meeting all product specifications and carrying the avionics to a safe landing.

Abbreviations

FEA - Finite Element Analysis

FEM - Finite Element Method

FI - Failure Index

CNC - Computer Numerical Control

UiS - University in Stavanger

GF - Glass Fiber

Max Q - Maximum Dynamic Pressure

Chapter 1

Background



Figure 1.1: UiS Aerospace

The purpose of this introductory chapter of is to present UiS Aerospace and its Borealis Program. Thereafter, it will be given a brief introduction to the central parts of Borealis II and its systems.

About UiS Aerospace

UiS Aerospace is an interdisciplinary student organization at the University of Stavanger that constructs rockets for research and educational purposes. The organization aims to provide its members with relevant expertise, particularly through participation in the development, testing, and launching of rockets. Our goal is to offer valuable experience in the field while fostering engagement in STEM (science, technology, engineering, and mathematics) subjects. Additionally, UiS Aerospace serves as a bridge between the University of Stavanger and the aerospace industry in Norway through unique collaborations across the country.

Following an impressive recruitment period in the fall of 2023, UiS Aerospace has expanded to an impressive 85 members divided into two programs. These programs, named Borealis and X, offer distinct opportunities within the organization. Borealis serves as the foundational program where new students can engage in constructing and launching model rockets from Spaceport Helleland, UiS Aerospace’s dedicated launch site. While X represents a more experimental venture with the ambitious goal of reaching space using a self-designed liquid propulsion rocket and its associated engine, Berserkr. In addition to these technical endeavors, UiS Aerospace also functions as a social platform, fostering a sense of belonging and enjoyment among its members. Notably, UiS Aerospace stands as the largest technical student organization at the University of Stavanger.

As UiS Aerospace continues to evolve, it is evident that the organization is not merely about achieving technical milestones but also about nurturing the human capital that will drive the space industry forward. The emphasis on a solid organizational framework and mental well-being signifies a holistic approach to education and professional development. It is this combination of technical prowess, safety consciousness, and community spirit that will enable UiS Aerospace to make a lasting impact in the aerospace domain and beyond.

The organizational structure of UiS Aerospace during the 2023/2024-school year is as shown in Figure 1.2.

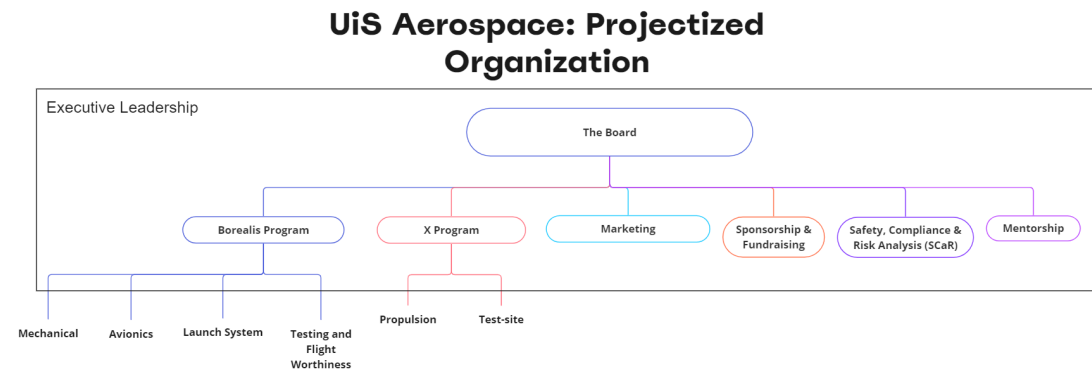


Figure 1.2: UiS Aerospace Organizational Structure 2023/2024

Executive leadership is comprised of all the leaders, and gives them the right to be a part of the board meeting, though they have no authority.

Core Values

UiS Aerospace works within 5 core values to ensure a healthy organization.

Safety

Failure to provide ample safety during the entire process of constructing, testing, and launching rockets, their engines and satellites can lead to death. Ensuring the safety of our members and any other people directly or indirectly involved in our activities is paramount to UiS Aerospace.

By complying to laws and safety regulations and cultivating awareness of the responsibility each member has to safeguard themselves and others UiS Aerospace seeks to develop solid safety procedures to ensure our mission in the space industry is done as safely as possible.

Innovation

By being bold and engaging in ambitious projects UiS Aerospace believe that we can inspire future generations to enter the space industry by showing that daring projects are possible. We believe that the more ambitious a project is, the more attention it will generate.

Balance

Balancing ambition and technical level are important to ensure progression in the organization. Projects cannot be too ambitious or they might never be realized, nor can they be boring and lazy.

"It's not rocket science"

At the core of UiS Aerospace's development strategy is the MVP (Minimum Viable Product) which aims to quickly produce functioning prototypes that are simplified versions of their intended use.

Given the high technical complexity of the rocket business it is essential to simplify where you can, and optimize where you have to.

Unity

The organization believes in making a positive impact by creating an arena for members to develop their skills as well as providing a social network of people for them to rely on. This is beneficial to students' mental well-being by offering membership in a group in which they feel a sense of belonging and unity.

The Borealis Program

Borealis is a 4-meter-long sounding rocket that is launched annually at the organization’s test launch site near Helleland. UiS Aerospace plans to launch the rocket Borealis II sometime between April 20 and May 5, 2024. This rocket is a direct evolution of the previous rocket launched at the same location in the school year 2022/2023. The estimated altitude the rocket is expected to reach is around 3500 meters.

Several bachelor theses are part of the project:

1. ***Flight Computer (Electronics, Data):***
Data acquisition, State estimation, and Control in Rocket
2. ***Recovery (Electronics):***
Parachute System and Sensor Monitoring Onboard Rocket
3. ***Telemetry (Electronics, Computer Science):***
Radio Communication and Data Transmission Between Rocket and Ground Station
4. ***GUI (Computer science):***
Data Processing and Visualization in Graphic User Interface (GUI)
5. ***Fuselage (Machine):***
Use of composite materials and filament winding machine



Figure 1.3: Borealis II

Previous launch

Borealis I, was the first rocket in the Borealis Program, and was launch the 22. of April 2023. The whole launch was streamed through [YouTube](#), and was a huge success.



Figure 1.4: Borealis accelerates along the 15 meter long launch rail at Helleland.

The radio communication with the rocket verified that all onboard electronics operated as planned, and the parachutes were successfully deployed at the peak of the rocket's trajectory. Nevertheless, it was subsequently revealed that an unknown error led to the parachutes failing to deploy correctly despite the separation and the brake shield deployment. Consequently, the rocket descended without the parachutes adequately reducing its speed. Shortly after launch, the rocket was discovered completely destroyed.

Though the rocket crashed and all the data was lost, the rocket soared the highest of any UiS Aerospace rocket to date with a height of 3266 meters above sea (10 594 foot).



Figure 1.5: Borealis soaring skywards

Overarching goals for this years launch

UiS Aerospace establishes its launch goals internally, with the organization collectively agreeing on these objectives. These self-defined goals must strike a balance between being realistic and challenging, encouraging members to grow and develop as engineers. For this years launch the following goals were set:

1. **Safety is maintained**
Safety must always be upheld to prevent harm to both individuals and property.
2. **Do not exceed altitude limit**
The rights to launch the rocket at Helleland have been granted by the Norwegian Aviation Authority. This authorization comes with an altitude restriction due to air traffic in the area. The altitude restriction is set to a maximum of 12,000 feet above mean sea level, or around 3,658 meters.
3. **Functional Recovery**
Given the previous year's issue with recovery, this year's objective is to ensure successful deployment of the parachutes and safely land the rocket within the property boundaries.
4. **Data acquisition and storage**
Throughout its flight, the rocket will continuously transmit data to the ground station. It is imperative that the rocket's location be determined and that it be recovered.

Explanation of functions on Borealis II

Borealis is a complex system comprising multiple projects that must work together to achieve a common goal. As a sounding rocket, Borealis is designed to collect measurement data through its payload. This data is crucial and needs to be preserved, which is why it is both sent to a ground station in real-time and stored locally on the rocket. However, the successful retrieval of locally stored data is contingent upon the safe landing of the rocket, ensured by a parachute system that deploys based on various factors, including the rocket's estimated altitude. These functionalities form the foundation of the electronic projects integrated into the Borealis system:

- **Power Unit**
The task of the power unit is to deliver power to all of the systems in the rocket, with the correct voltage. There will be sufficient amount of power stored for the countdown procedure, flight and rescue.
- **Telemetry**
Telemetry has the main responsibility to ensure that data gets transferred to the Ground Station in real-time. In addition to this, provision must be made for communication from the Ground Station to the rocket, this is called two-way communication.
- **Sensor and altitude estimation**
The main area of responsibility for the sensor system is the acquirement of measurement. The data will, among other things, be used to estimate the rocket's altitude.
- **Recovery**
"Recovery" is a collective term for everything that involves parachute release, locating and retrieving the rocket after it has been launched. The responsibility of this feature is therefore the recovery of the rocket, in it's entirety.

Outer Components

The rockets outer components are mainly made by the machine group. All of the components are designed by UiS Aerospace, and thereafter manufactured by members, employees at UiS or sponsors. The rockets outer components are described in the following points:

- **Nose Cone**

Material: *Carbon fiber, ABS plastic & Alu 6081 T6*

The nosecone is comprised of three separate parts that are bound or glued together. There is an eye-bolt connected to the nose to keep it in place, and at the same time create a connection point for the elastic parachute lines.

- **Main Fuselage**

Material: *Glass fiber*

The main fuselage is the one covering the electronics bay. This is, for the first time, made out of glassfiber to enable telemetry to a higher degree then earlier rockets. This is made with the filament winding technology.

- **Lower Fuselage**

Material: *Carbon fiber*

The lower fuselage is made of carbon fiber, bought from Carbon Composites in Germany, and customized in the workshop.

- **Coupler**

Material: *Alu 6081 T6*

The coupler is made from to separate parts and is located at the top part of the rocket. The coupler itself, and the bulkhead. the idea is a simpler was to assemble the rocket, with removing much of the screw holes that was needed in last years rocket. The assembly is easily done by screwing the coupler unto the bulkhead.

- **Radax**

Material: *Alu 6081 T6*

The radax is a new addition, and works to separate the electronics from the motor. With this solution it is possible to assemble the motor and electronics at the same time before screwing them both together to make the finished rocket. The radax also works to hold the motor in place during the descend.

- **Fins**

Material: *Alu 6081 T6 & ABS plastic*

The fins works as stabilizers of the rocket and are made of aluminium. The base of the fins are printed in ABS, as last year, because of the complex geometry. The fins are located at the aft of the rocket to place the center of pressure behind the center of gravity.

- **Boat tail**

Material: *Alu 6081 T6*

The Boat tail has two main purposes: (1) supporting the engine at the rocket's base to direct forces upwards along the fuselage, and (2) decreasing air resistance by narrowing towards the aft end of the rocket, thus reducing its aerial footprint.

Inner components

The inner components consist of the parts mounted on the interior of the rocket.

MAVION

Standing for Main Avionics Unit. Avionics cover the self-developed electronic system in the Borealis II rocket, addressing data collection, radio communication, and parachute deployment to ensure a controlled descent after launch. The electronic system in the rocket is powered by two batteries controlled by a power supply system. On the ground station, collected data is presented in a user interface, GUI. Data is transferred from the rocket module to the ground station, and the ground station can send commands to the rocket module.

Rideshare

As part of UiS Aerospace's educational initiative, space within the rocket is allocated for what is known as rideshares. These rideshares accommodate projects involving high school groups, with each group assigned a space of 1U. A standard unit of measurement for satellites, 1U describes a 10x10x10 mm cube. For Borealis II, three groups—two from Bryne High School and one from Vardheia Middle School—were selected. These groups will collect data and film the launch.

Pro98 Motor

The rocket's propulsion is provided by a reusable Pro98 6G rocket motor. For the April 2024 launch, it was loaded with a fuel package containing four charges of solid rocket propellant, primarily composed of ammonium perchlorate (NH_4ClO_4) and aluminium. Manufactured by Cesaroni Technologies, the motor can deliver a total impulse of 10,366.9 Ns and an average thrust of approximately 1600 N.

Launch Rail

UiS Aerospace operates a test launch site at Støla near Helleland, located north-northeast of Egersund. The site is equipped with threaded rods embedded in the bedrock to facilitate the installation of a 15-meter-high launch rail, developed by the Launch System group, as seen in Figure 1.6. This launch rail plays a critical role in ensuring the rocket's trajectory remains stable, guiding it sufficiently far from the launch area to minimize the risk of potential impacts during descent. This objective is primarily achieved through two key methods:

1. Launch Angle

The launch angle is carefully calculated to ensure that, regardless of wind conditions, the rocket lands at a safe distance from the launch site. For instance, for the Borealis project, a safety distance of 500 meters was established. Considering a simulated flight altitude of approximately 3000 meters, an 80-degree launch angle was determined as optimal, resulting in a landing zone 529 meters away from the launch site in a direct line. This calculation is based on the formula where h_s represents the simulated altitude, and θ signifies the launch angle, yielding a distance denoted as a of roughly 529 meters.

$$\frac{h_s}{\tan(\theta)} = a$$

$$\frac{3000}{\tan(80)} = 528.9\text{m}$$

2. Rail system

In the initial phase of flight, the rocket lacks directional stability. This instability persists until the aerodynamic forces acting on the fins become sufficiently strong to prevent significant deviations, even when subjected to external forces like wind. The height of the launch rail is based on the height at which the rocket reaches a stable velocity.



Figure 1.6: Launch Rail at Støla

Chapter 2

Introduction



Figure 2.1: Borealis Program Poster

This bachelor thesis focuses on the manufacturing of the fuselage for the rocket Borealis II. The introduction explores the challenges and specifications associated with the rocket.

Project Description

This thesis, titled "Rocket fuselage development using composite filament winding technology", delves into various technical aspects related to rocket development. It encompasses mandrel design and production, FEM strength calculations, and the production of the rocket's body through collaborations with industry partners, utilizing a filament winding machine.

The primary objective of this research is to comprehensively investigate and analyze critical components and processes within the realm of rocket design and production. By employing theoretical analysis, computer-aided design, and FEM simulations, the project aims to enhance our understanding of the structural considerations involved in rocket development. This research is particularly valuable for UiS Aerospace, as it provides crucial insights that can contribute to the efficiency, safety, and overall performance of rocket systems.

Justification for the Thesis

Glass fiber

UiS Aerospace has selected glass fiber as the optimal material for the fuselage. The glass fiber material was specifically chosen due to its exceptional weight-to-strength ratio, rendering it optimal for aerospace applications. Additionally, its ability to efficiently transmit and receive electronic signals makes it ideal for the avionic unit, MAVION, situated within the fuselage.

This choice results in a significantly lighter fuselage compared to non-fiber materials of similar strength, thereby optimizing flight performance. Importantly, it addresses a key issue encountered with the previous rocket, Borealis I, where transmitting radio signals through the carbon fiber fuselage proved challenging.

Process of Filament Winding Production

Filament winding emerges as the optimal method for the manufacturing of cylindrical shaped fiber materials, by virtue of the seamless symmetrical rotation of cylindrical shapes, allowing the machine's carriage to work as intended.

This method of production facilitates the customization of the fiber angle. Fiber angles are fundamental variables for optimizing fuselage utilization because fiber materials exhibit greater strength when aligned with the fiber orientation.

The machine operates by rotating the mandrel around its main axis, while a non-rotating carriage feeds the mandrel with fiber material. This carriage travels parallel to the cylinder's main axis in a back-and-forth motion. Forming a pattern containing numerous helices of filament around the mandrel, these filament helices shape a solid body of composite material, taking the mandrel's shape.

UiS Aerospace plans to utilize the fuselage across multiple iterations of the Borealis program, aiming to streamline the fuselage design process for future projects. With consistent dimensions in diameter and thickness for the Borealis Program, creating a new fuselage will be simplified due to the pre-existing mandrel constructed as part of this thesis. As a result, in the event of a crash landing leading to fuselage damage or deformation, the production of a replacement will be significantly accelerated and cost-effective.

Project Specifications

The target specifications and definitive specifications set by UiS Aerospace, along with the production process, encompass design parameters and predetermined variable values. To design the Fuselage, the following criteria are considered:

- The fuselage will be in the shape of a cylindrical tube.
- The outer diameter of the fuselage will be $d_{out} = 155mm$
- The inner diameter of the fuselage will be $d_{inn} = 150mm$
- The length off the fuselage will be $l_{total} = 2000mm$
- The fuselage must withstand the dynamic pressure that arise during flight.

The specifications resulting from the production process and OPS Composite Solutions are:

- The mandrel will be exposed to a pulling force, estimated to 30kg, placed at the middle of the mandrel during the production process.
- The geometries for the Winding Adapter is predetermined by the geometry of the winding machine.
- The maximum deformation of the mandrel is $\epsilon_{max} = 2mm$
- The length from the winding zone to the winding-machine itself should be larger than $s_{from} = 500mm$
- The glass fiber-epoxy mix that will be used is SE3030 and Ampreg 31. Material data in Table A.1
- The total bandwidth, of filament wound unto the mandrel, must be set to somewhere between 10 and 25 mm in the CADWIND software.

Structure of the report

The thesis is structured around theoretical calculations and simulations due to the impracticality of reading structural and numerical results from the usage of the finalized product. These impracticalities comes from the nature of testing rockets. The tests are often destructive with little data to review the work upon. Since UiS Aerospace is limited both in production capacity and money, it is a direct consequence that this project is restricted to manufacturing one fuselage composed of glass fiber. Therefore the Simulations and calculations will be essential in predicting the strength and practicality of the fuselage which will be tested on launch. Because of the theoretical importance, the thesis is structured around multiple theoretical analyses.

The analyses will be organized from a production perspective. This means that the calculations will be structured in such a way that those required for the production process will be prioritized. Production calculations will encompass a comprehensive structural analysis of the mandrel, encompassing both welds and overall structure within the anticipated production environment.

To optimize the finalized product, simulations of the fiber angle will be developed. Optimizing the fiber angle aims to determine the ideal fiber angles that meet the product specifications, which will then be employed in a conclusive structural analysis of the glass fiber-based fuselage.

Further on, the manufacturing will be explained and the launch results will be presented, followed by a discussion of these findings and the conclusion of the work, including potential enhancements and further work.

Chapter 3

Basic Theory

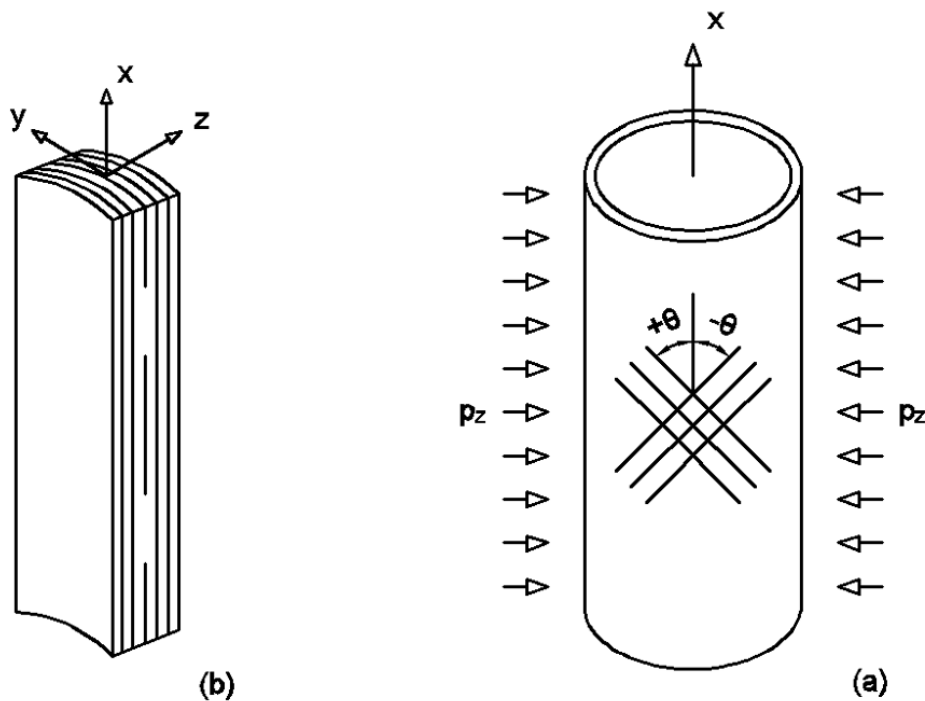


Figure 3.1: Simplified figure of the fuselage problem [1]

Having a basic understanding of how a structure composed of composite materials works is crucial to this thesis. This chapter will therefore introduce the basic theory behind laminae and laminates of composite material, while also defining what dynamic pressure is and how it affects this specific project.

Mechanics of Composite Materials

Composite materials are widely utilized in the industry and renowned for their high strength-to-weight ratio. Due to various manufacturing methods, composites are applicable in numerous situations. The manufacturing process and calculations for composites are more demanding than for traditional materials, making them ideal for optimization purposes.

Composite materials refer to multi-phase materials that are artificially produced, as opposed to naturally occurring materials. Most fiber-reinforced composites comprise of two distinct phases: the Matrix phase and the Dispersed phase, illustrated in Figure 3.2. These phases must be chemically dissimilar and separated by a clear interface. The dispersed phase is in this context the fiber while the matrix phase is the epoxy. [1]

Fiber-reinforced composites high strength and stiffness relative to their weight, is achieved through a structure composed of two-dimensional sheets containing continuous fibers called laminae. When these laminae are stacked, they form a multi-layered structure known as a laminate, with each layer retaining its individual preferred high-strength direction [2]. This results in directional dependency in the properties of each layer, with the highest stiffness and strength aligning with the fiber direction of each laminae. Consequently, the orientation and concentration of laminae significantly impact the strength and strongest direction of the laminate as a whole [1]. An illustration of the orientations of laminate can be seen in Figure 3.3.

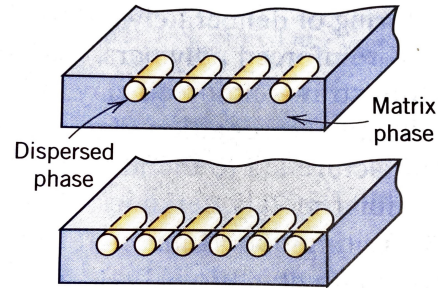


Figure 3.2: Fiber-Reinforced Composites Structure [2]

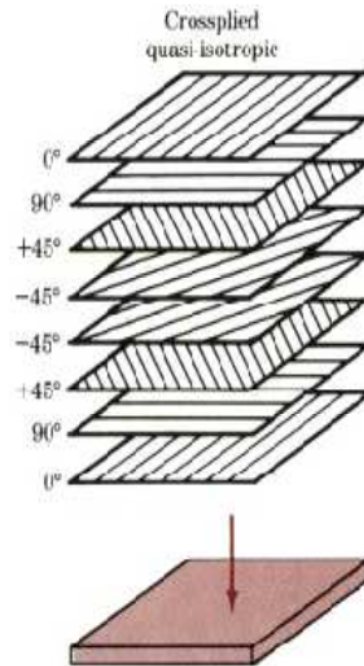


Figure 3.3: Schematic Illustration of Laminae combined to form a Laminate [3]

Step-by-Step Optimal Angle Analysis

The procedure, in Figure 3.4, can be used to find the allowable pressure for a given angle, θ . And by proxy, find the optimal angle [1]. In this section, all the steps of the procedure will be explained, starting from the $\sigma_1, \sigma_2, \tau_{12}$ and going backwards, in reference to Figure 3.4. The failure criterion will be explained at the end, as a good understanding of laminae theory is needed for this step.

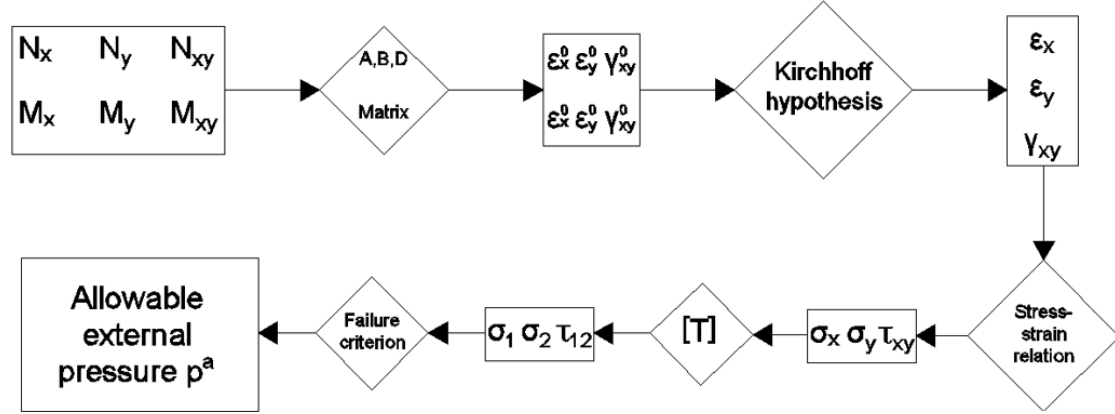


Figure 3.4: Procedure to find the allowable external pressure, p^a [1]

Generalization of Hooke's law

To understand how fiber materials works, a general expression of the stress and strain for the laminae is constructed. Considering that the material properties are anisotropic, it is advantageous to employ a local coordinate system where one axis aligns with the fibers' direction. This coordinate system, depicted in Figure 3.5, includes the axes x_1, x_2, x_3 , with x_1 oriented parallel to the fibers. Each direction x_1, x_2, x_3 corresponds to its own elastic modulus E_1, E_2, E_3 , respectively [1].

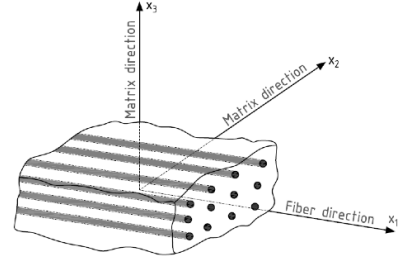


Figure 3.5: Principle Coordinate System [1]

The relationship between strain and stress can be expressed according to the x_1, x_2, x_3 coordinate system, resulting in a matrix equation involving the Compliance matrix $[S]$, equation 3.1 [1]. The equations giving the engineering constants S_{ij} can be found in appendix D.1.

$$\begin{Bmatrix} \epsilon_1 \\ \epsilon_2 \\ \epsilon_3 \\ \gamma_{23} \\ \gamma_{13} \\ \gamma_{12} \end{Bmatrix} = \begin{bmatrix} S_{11} & S_{12} & S_{13} & 0 & 0 & 0 \\ S_{21} & S_{22} & S_{23} & 0 & 0 & 0 \\ S_{31} & S_{32} & S_{33} & 0 & 0 & 0 \\ 0 & 0 & 0 & S_{44} & 0 & 0 \\ 0 & 0 & 0 & 0 & S_{55} & 0 \\ 0 & 0 & 0 & 0 & 0 & S_{66} \end{bmatrix} \begin{Bmatrix} \sigma_1 \\ \sigma_2 \\ \sigma_3 \\ \tau_1 \\ \tau_2 \\ \tau_3 \end{Bmatrix} \quad (3.1)$$

This can be written in a shorthand notation as the following

$$\{\epsilon\} = [S] \{\sigma\} \quad (3.2)$$

The relationship between stress and strain can be derived from equation 3.1, This results in a generalization of Hooke's law with the stiffness matrix $[C]$. The values in the stiffness matrix are material constants, C_{ij} for $(i,j) \in [1,6]$. The equations for calculating C_{ij} can be found in appendix D.2. [1].

$$\begin{Bmatrix} \sigma_1 \\ \sigma_2 \\ \sigma_3 \\ \tau_1 \\ \tau_2 \\ \tau_3 \end{Bmatrix} = \begin{bmatrix} C_{11} & C_{12} & C_{13} & 0 & 0 & 0 \\ C_{21} & C_{22} & C_{23} & 0 & 0 & 0 \\ C_{31} & C_{32} & C_{33} & 0 & 0 & 0 \\ 0 & 0 & 0 & C_{44} & 0 & 0 \\ 0 & 0 & 0 & 0 & C_{55} & 0 \\ 0 & 0 & 0 & 0 & 0 & C_{66} \end{bmatrix} \begin{Bmatrix} \varepsilon_1 \\ \varepsilon_2 \\ \varepsilon_3 \\ \gamma_{23} \\ \gamma_{13} \\ \gamma_{12} \end{Bmatrix} \quad (3.3)$$

For shorthand notation

$$\{\sigma\} = [C] \{\varepsilon\} \quad (3.4)$$

The calculation of the engineering constants, denoted as S_{ij} , and the material constants, denoted as C_{ij} , relies on the material properties such as Young's modulus (E), Poisson's ratio (ν), and shear modulus (G) given by the manufacturer. Detailed tables for these constants can be found in appendix D.

Plate Theory Simplification

For further calculations, some simplifications can be applied to reduce the matrix sizes. One of these simplifications is due to plate theory. In plate theory, a plate, as a structural element, is defined by two metrics; (1) it possesses geometrical dimensions within the plane that are significantly larger than its thickness, and (2) it is subject to loads inducing bending deformation as well as stretching. Typically, the thickness of a plate does not exceed one-tenth of its smallest in-plane dimension. Due to this relatively small thickness, complex 3D elasticity equations may not be necessary for modeling the structure. Instead, simplified 2D plate theories can be formulated to analyze the deformation and stress distribution in plate structures. [4]

Viewing the laminae as a plate, the compliance and stiffness matrices can be simplified. According to plate theory, the in-plane stress will be significantly larger than the stresses normal to the plate. Hence, the stress components normal to the plate can be ignored, resulting in $\sigma_3 = 0, \tau_{13} = 0, \tau_{23} = 0$. This simplification leads to a reduction of the compliance Matrix $[S]$ 3.1, and yields the following equation [1]:

$$\begin{Bmatrix} \varepsilon_1 \\ \varepsilon_2 \\ \gamma_{12} \end{Bmatrix} = \begin{bmatrix} S_{11} & S_{12} & 0 \\ S_{21} & S_{22} & 0 \\ 0 & 0 & S_{66} \end{bmatrix} \begin{Bmatrix} \sigma_1 \\ \sigma_2 \\ \tau_{12} \end{Bmatrix} \quad (3.5)$$

In addition to this, the matrix equation can be further simplified using the Maxwell-Betti Reciprocal Theorem. The following relations between the material properties are then obtained [1]:

$$\frac{\nu_{12}}{E_1} = \frac{\nu_{21}}{E_2} \quad (3.6)$$

$$\frac{\nu_{13}}{E_1} = \frac{\nu_{31}}{E_3} \quad (3.7)$$

$$\frac{\nu_{23}}{E_2} = \frac{\nu_{32}}{E_3} \quad (3.8)$$

This yield the following relation

$$S_{21} = S_{12} \quad (3.9)$$

making the reduced compliance matrix look like this:

$$\begin{Bmatrix} \epsilon_1 \\ \epsilon_2 \\ \gamma_{12} \end{Bmatrix} = \begin{bmatrix} S_{11} & S_{12} & 0 \\ S_{12} & S_{22} & 0 \\ 0 & 0 & S_{66} \end{bmatrix} \begin{Bmatrix} \sigma_1 \\ \sigma_2 \\ \tau_{12} \end{Bmatrix} \quad (3.10)$$

These simplification also leads to a simplified version of the stiffness matrix [C], Equation 3.3:

$$\begin{Bmatrix} \sigma_1 \\ \sigma_2 \\ \tau_{12} \end{Bmatrix} = \begin{bmatrix} Q_{11} & Q_{12} & 0 \\ Q_{12} & Q_{22} & 0 \\ 0 & 0 & Q_{66} \end{bmatrix} \begin{Bmatrix} \epsilon_1 \\ \epsilon_2 \\ \gamma_{12} \end{Bmatrix} \quad (3.11)$$

Where, using the engineering constants, the reduced stiffness members Q_{ij} lead to these relations, when combined with the equations D.1 - D.21, and D.24 - D.25:

$$Q_{11} = \frac{E_1}{1 - \nu_{12}\nu_{21}} \quad (3.12)$$

$$Q_{12} = \frac{\nu_{12}E_2}{1 - \nu_{12}\nu_{21}} = \frac{\nu_{21}E_1}{1 - \nu_{12}\nu_{21}} \quad (3.13)$$

$$Q_{22} = \frac{E_2}{1 - \nu_{12}\nu_{21}} \quad (3.14)$$

$$Q_{66} = G_{12} \quad (3.15)$$

Transformation Matrix

As previously discussed, composite materials are composed of multiple layers of laminae. Since these layers have different directions there is need for a coordinate system to unify the local coordinate systems. To ensure alignment across different layers, local coordinates must be transformed into a global coordinate system. The global coordinate system encompasses the entire system with common axes denoted as X , Y , and Z . The different axes are depicted in Figure 3.6. The transformation of local coordinate systems to a unified global coordinate system is achieved with the following equation: [1]

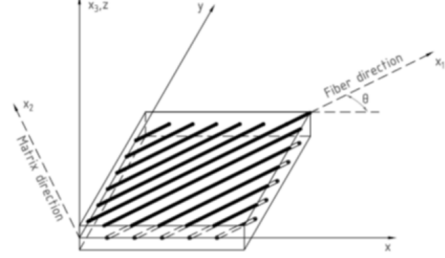


Figure 3.6: Transformation from local to global coordinate system [1]

$$\begin{Bmatrix} \sigma_1 \\ \sigma_2 \\ \tau_{12} \end{Bmatrix} = [T] \begin{Bmatrix} \sigma_x \\ \sigma_y \\ \tau_{xy} \end{Bmatrix} \quad (3.16)$$

where the matrix $[T]$ is the transformation matrix, which is equal to

$$[T] = \begin{bmatrix} \cos^2\theta & \sin^2\theta & 2\sin\theta\cos\theta \\ \sin^2\theta & \cos^2\theta & -2\sin\theta\cos\theta \\ -\sin\theta\cos\theta & \sin\theta\cos\theta & \cos^2\theta - \sin^2\theta \end{bmatrix} \quad (3.17)$$

the angle θ , is the angle from the global x axis to the specific fiber orientation of the laminae. [1] For strains, the transformation equation is:

$$\begin{Bmatrix} \epsilon_1 \\ \epsilon_2 \\ \frac{1}{2}\gamma_{12} \end{Bmatrix} = [T] \begin{Bmatrix} \epsilon_x \\ \epsilon_y \\ \frac{1}{2}\gamma_{xy} \end{Bmatrix} \quad (3.18)$$

By combining equations 3.11, 3.16 and 3.18 the transformed reduced stiffness matrix, \bar{Q} , can be constructed. This matrix combines the stiffness and compliance matrices to a single matrix. Using this matrix, the correlation between the stress and strain of the laminae can be calculated using the fiber angle and the material properties of the fiber. [1] The matrix is written as following:

$$\begin{Bmatrix} \sigma_x \\ \sigma_y \\ \tau_{xy} \end{Bmatrix} = \begin{bmatrix} \bar{Q}_{11} & \bar{Q}_{12} & \bar{Q}_{16} \\ \bar{Q}_{12} & \bar{Q}_{22} & \bar{Q}_{26} \\ \bar{Q}_{16} & \bar{Q}_{26} & \bar{Q}_{66} \end{bmatrix} \begin{Bmatrix} \epsilon_x \\ \epsilon_y \\ \gamma_{xy} \end{Bmatrix} \quad (3.19)$$

where

$$\bar{Q}_{11} = Q_{11}m^4 + 2(Q_{12} + 2S_{66})n^2m^2 + Q_{22}n^4 \quad (3.20)$$

$$\bar{Q}_{12} = (Q_{11} + Q_{22} - 4Q_{66})n^2m^2 + Q_{12}(n^4 + m^4) \quad (3.21)$$

$$\bar{Q}_{16} = (Q_{11} - Q_{12} - 2Q_{66})nm^3 + (Q_{12} - Q_{22} + 2Q_{66})n^3m \quad (3.22)$$

$$\bar{Q}_{22} = Q_{11}n^4 + 2(Q_{12} + 2Q_{66})n^2m^2 + Q_{22}m^4 \quad (3.23)$$

$$\bar{Q}_{26} = (Q_{11} - Q_{12} - 2Q_{66})n^3m + (Q_{12} - Q_{22} + 2Q_{66})nm^3 \quad (3.24)$$

$$\bar{Q}_{66} = (Q_{11} + Q_{22} - 2Q_{12} - 2S_{66})n^2m^2 + Q_{66}(n^4 + m^4) \quad (3.25)$$

using notations $m = \cos\theta$ and $n = \sin\theta$. The parameters Q_{ij} are called reduced stiffnesses.

Classical Lamination Theory

On this point, all the calculations for a single laminae is completed. From here, all the properties of all laminae layers will be added together to complete the stack, a laminate. The total number of layers is denoted as N . Such a stack can be seen in Figure 3.7

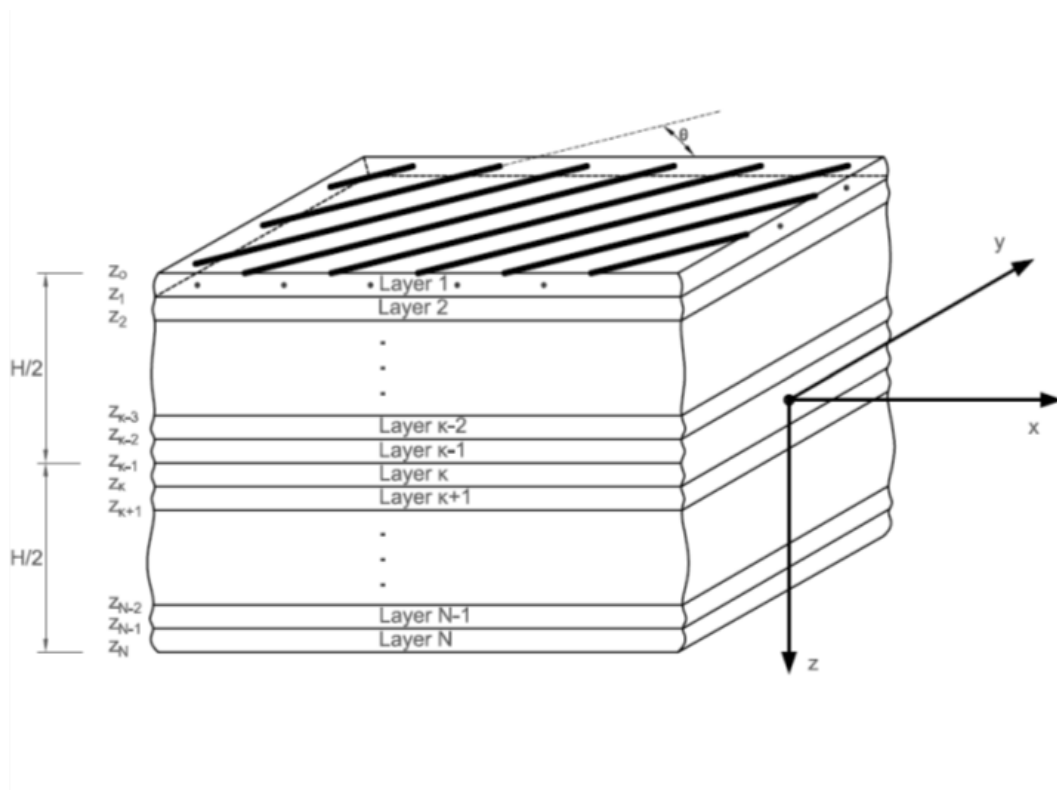


Figure 3.7: Laminae stacked [1]

Kirchhoff Isotropic Plate Theory

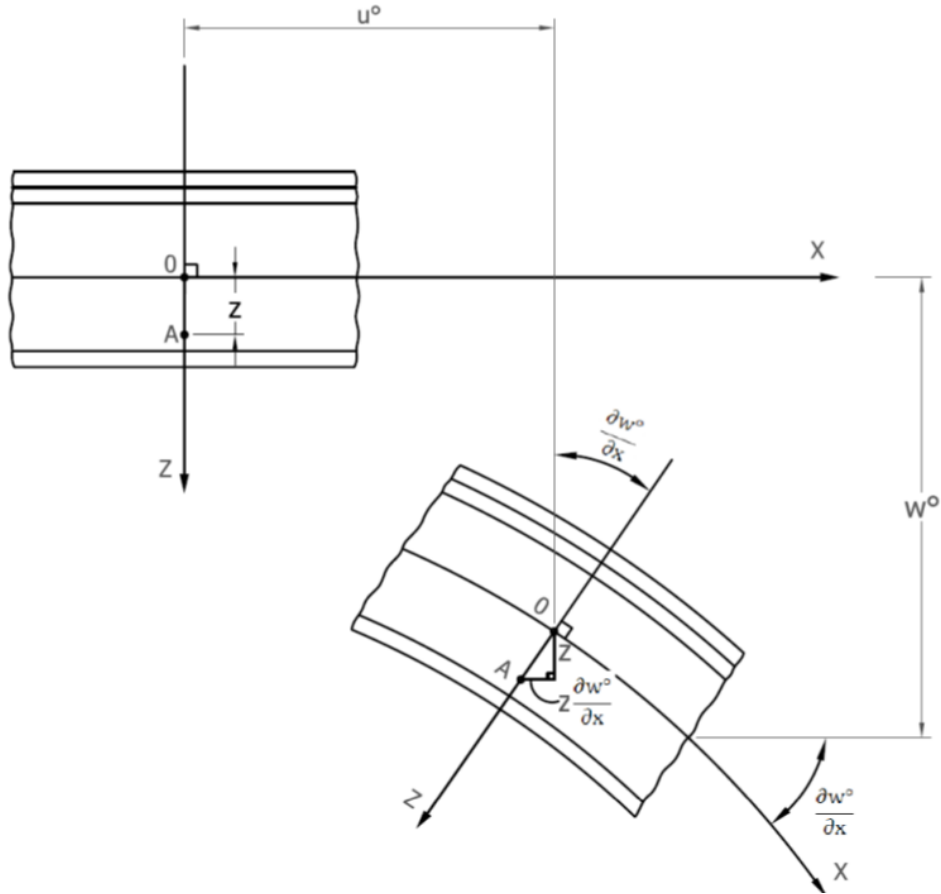


Figure 3.8: Undeformed and deformed geometry of a plate considering Kirchhoff assumptions [1]

Classical plate theory, as previously discussed, relies on the Kirchhoff hypothesis. This implies that the Kirchhoff isotropic plate theory can be utilized to account for deformation curvature as long as the assumptions of the theorem are satisfied. [4]

As the laminate is considered a plate, the Kirchhoff plate theory can be applied. It consists of the following three statements [4]. Figure 3.8 illustrates the statements.

1. Straight lines perpendicular to the mid-surface before deformation remain straight after deformation.
2. The transverse normals do not experience elongation.
3. The transverse normals rotate such that they remain perpendicular to the middle surface after deformation.

Using these statements and the common strain-displacement relations, shown in appendix D.5, both the transverse shear and transverse normal effects can be neglected, resulting in [1]:

$$\varepsilon_x = \varepsilon_x^0 + zk_x^0 \quad (3.26)$$

$$\varepsilon_y = \varepsilon_y^0 + zk_y^0 \quad (3.27)$$

$$\varepsilon_z = 0 \quad (3.28)$$

$$\gamma_{xy} = \gamma_{xy}^0 + zk_{xy}^0 \quad (3.29)$$

$$\gamma_{xz} = 0 \quad (3.30)$$

$$\gamma_{yz} = 0 \quad (3.31)$$

where

$$\varepsilon_x^0 = \frac{\partial u}{\partial x} \quad (3.32)$$

$$\varepsilon_y^0 = \frac{\partial v}{\partial y} \quad (3.33)$$

$$\gamma_{xy}^0 = \frac{\partial v^0}{\partial x} + \frac{\partial u}{\partial y} \quad (3.34)$$

$$k_x^0 = -\frac{\partial^2 w^0}{\partial x^2} \quad (3.35)$$

$$k_y^0 = -\frac{\partial^2 w^0}{\partial y^2} \quad (3.36)$$

$$k_{xy}^0 = -2\frac{\partial^2 w^0}{\partial x \partial y} \quad (3.37)$$

Replacing the strains, in the transformed reduced stiffness matrix, with these new values:

$$\begin{Bmatrix} \sigma_x \\ \sigma_y \\ \tau_{xy} \end{Bmatrix} = \begin{bmatrix} \overline{Q}_{11} & \overline{Q}_{12} & \overline{Q}_{16} \\ \overline{Q}_{12} & \overline{Q}_{22} & \overline{Q}_{26} \\ \overline{Q}_{16} & \overline{Q}_{26} & \overline{Q}_{66} \end{bmatrix} \begin{Bmatrix} \varepsilon_x^0 + zk_x^0 \\ \varepsilon_y^0 + zk_y^0 \\ \gamma_{xy}^0 + zk_{xy}^0 \end{Bmatrix} \quad (3.38)$$

The strains ε_x^0 , ε_y^0 , and γ_{xy}^0 represent the surface extensional strain in the x and y directions and the surface in-plane shear strain, respectively. These values describe how much the material stretches or deforms in different directions when subjected to loads. [4]

The quantities k_x^0 and k_y^0 signify the curvature of the reference surface in the x and y directions, respectively. These values indicate how much the surface curves or bends along these axes.[4]

Finally, k_{xy}^0 refers to the reference twisting curvature, which describes the tendency of the surface to twist or deform in a rotational manner. [4]

ABD-matrix

These variables, ε^0 , γ^0 , k^0 , are found from the forces and moments, N and M respectfully, through ABD matrix. Written in matrix form, this is [1]:

$$\begin{Bmatrix} N_x \\ N_y \\ N_{xy} \\ M_x \\ M_y \\ M_{xy} \end{Bmatrix} = \begin{bmatrix} A_{11} & A_{12} & A_{16} & B_{11} & B_{12} & B_{16} \\ A_{12} & A_{22} & A_{26} & B_{21} & B_{22} & B_{26} \\ A_{16} & A_{26} & A_{66} & B_{16} & B_{26} & B_{66} \\ B_{11} & B_{12} & B_{16} & D_{11} & D_{12} & D_{16} \\ B_{12} & B_{22} & B_{26} & D_{12} & D_{22} & D_{26} \\ B_{16} & B_{26} & B_{66} & D_{16} & D_{26} & D_{66} \end{bmatrix} \begin{Bmatrix} \varepsilon_x^0 \\ \varepsilon_y^0 \\ \gamma_{xy}^0 \\ k_x^0 \\ k_y^0 \\ k_{xy}^0 \end{Bmatrix} \quad (3.39)$$

where the A,B and D are defined as [1]:

$$A_{ij} = \sum_{k=1}^N \overline{Q_{ij_k}} (z_k - z_{k-1}) \quad (3.40)$$

$$B_{ij} = \frac{1}{2} \sum_{k=1}^N \overline{Q_{ij_k}} (z_k^2 - z_{k-1}^2) \quad (3.41)$$

$$D_{ij} = \frac{1}{3} \sum_{k=1}^N \overline{Q_{ij_k}} (z_k^3 - z_{k-1}^3) \quad (3.42)$$

where z is the distance from the top of the stack, $z = 0$.

From here, the abd matrix is needed. This can be calculated from inverting the ABD matrix like this [1]

$$\begin{bmatrix} A_{11} & A_{12} & A_{16} & B_{11} & B_{12} & B_{16} \\ A_{12} & A_{22} & A_{26} & B_{21} & B_{22} & B_{26} \\ A_{16} & A_{26} & A_{66} & B_{16} & B_{26} & B_{66} \\ B_{11} & B_{12} & B_{16} & D_{11} & D_{12} & D_{16} \\ B_{12} & B_{22} & B_{26} & D_{12} & D_{22} & D_{26} \\ B_{16} & B_{26} & B_{66} & D_{16} & D_{26} & D_{66} \end{bmatrix}^{-1} = \begin{bmatrix} a_{11} & a_{12} & a_{16} & b_{11} & b_{12} & b_{16} \\ a_{12} & a_{22} & a_{26} & b_{21} & b_{22} & b_{26} \\ a_{16} & a_{26} & a_{66} & b_{16} & b_{26} & b_{66} \\ b_{11} & b_{12} & b_{16} & d_{11} & d_{12} & d_{16} \\ b_{12} & b_{22} & b_{26} & d_{12} & d_{22} & d_{26} \\ b_{16} & b_{26} & b_{66} & d_{16} & d_{26} & d_{66} \end{bmatrix} \quad (3.43)$$

Boundary Conditions due to Dynamic Pressure

Boundary conditions for laminae can be hard to decide / estimate, as the space on which is calculated is finitely small. The boundary conditions for this thesis can however be simplified due to there only being one force, the force from the dynamic pressure during flight. Taking this into consideration, the fuselage can be considered a long pipe, with diameter D , thickness h and stacking sequence $[\pm\theta]$. In order to determine the external forces acting to the pipe's wall, the equilibrium equation (equation. 3.44) of the half pipe shown in Figure 3.9 should be used [1]:

$$2N_y L = pDL \text{ or } N_y = \frac{1}{2}pD \tag{3.44}$$

where p is the dynamic pressure.

Because of the absence of external loads in directions x and xy , N_y is the only load acting on the laminate. This yield the following equations from, the inverse ABD matrix, denoted in [1]:

$$\varepsilon_x^0 = a_{12}N_y \tag{3.45}$$

$$\varepsilon_y^0 = a_{22}N_y \tag{3.46}$$

$$\gamma_{xy}^0 = a_{26}N_y \tag{3.47}$$

$$k_x^0 = b_{21}N_y \tag{3.48}$$

$$k_y^0 = b_{22}N_y \tag{3.49}$$

$$k_{xy}^0 = b_{26}N_y \tag{3.50}$$

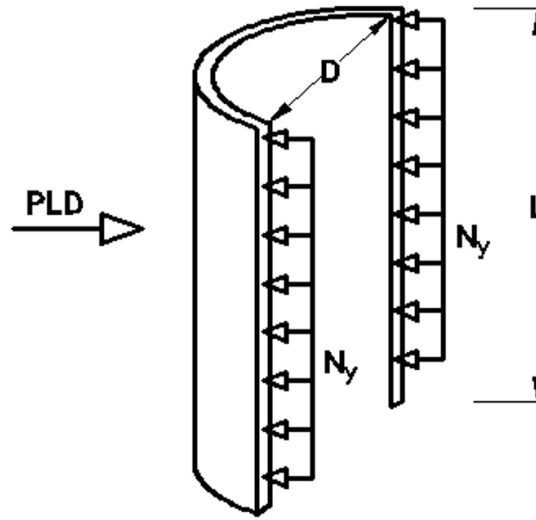


Figure 3.9: Equilibrium of a half-pipe [1]

From here, it is possible to start calculating the stresses, σ_1, σ_2 & τ_{12} as shown in the calculation procedure in Figure 3.4.

Tsai-Wu Failure Criterion

The final phase in the process involves applying the Tsai-Wu Criterion, a pivotal step particularly in assessing failure in composite material laminates. This criterion is extensively employed for failure calculations. It predicts failure when the failure index FI within a laminate equals one. [5] Using the previously mentioned plane-stress assumption, FI can be expressed as follows [1]:

$$FI = F_1\sigma_1 + F_2\sigma_2 + F_{11}\sigma_1^2 + F_{22}\sigma_2^2 + F_{66}\tau_{12}^2 - \sqrt{F_{11}F_{22}}\sigma_1\sigma_2 = 1 \tag{3.51}$$

where σ_1, σ_2 and τ_{12} denotes the stress components at failure and where the F_{ij} are expressed in terms of the experimentally determined strength values of the material in tension, compression, and shear. The F_{ij} are given by [5]:

$$F_1 = \frac{1}{\sigma_1^T} + \frac{1}{\sigma_1^C} \quad (3.52)$$

$$F_2 = \frac{1}{\sigma_2^T} + \frac{1}{\sigma_2^C} \quad (3.53)$$

$$F_{11} = -\frac{1}{\sigma_1^T \sigma_1^C} \quad (3.54)$$

$$F_{22} = -\frac{1}{\sigma_2^T \sigma_2^C} \quad (3.55)$$

$$F_{66} = \left(\frac{1}{\tau_{12}^C}\right)^2 \quad (3.56)$$

The variables of σ & τ are material properties given by the manufacturer, found in Appendix A.2.

The criterion can also be expressed in terms of a safety factor η , which is equal to the scalar load multiplier λ that results in the onset of failure. [5] Doing so, σ can be expressed as

$$\bar{\sigma} = \lambda \sigma = \lambda \{\sigma_1 \quad \sigma_2 \quad \tau_{12}\}^T \quad (3.57)$$

The inhomogeneous Tsai-Wu criterion can now be written as

$$\lambda^2(F_{11}\sigma_1^2 + F_{22}\sigma_2^2 + F_{66}\tau_{12}^2 - \sqrt{F_{11}F_{22}}\sigma_1\sigma_2) + \lambda(F_1\sigma_1 + F_2\sigma_2) - 1 = 0 \quad (3.58)$$

The load multiplier at failure, λ , can then be calculated using [5].

$$\lambda = \frac{-b \pm \sqrt{b^2 + 4a}}{2a} \quad (3.59)$$

with

$$a = F_{11}\sigma_1^2 + F_{22}\sigma_2^2 + F_{66}\tau_{12}^2 - \sqrt{F_{11}F_{22}}\sigma_1\sigma_2 \quad (3.60)$$

and

$$b = F_1\sigma_1 + F_2\sigma_2 \quad (3.61)$$

Since the Tsai-Wu is a second order algebraic equation, two values of λ will be obtained. The factor of safety η will be the lowest positive number of the two.

Dynamic Pressure

Maximum dynamic pressure, commonly known as Max Q, is one of the most important variables used to dimension the fuselage of a rocket. Max Q is the moment of peak mechanical stress on the rocket and depends on the speed of the rocket and air density around it. It is common to throttle down the engine to lower the Max Q, but since this is not possible with the configuration of Borealis II the fuselage must be calculated according to the Max Q from the simulations of the flight.

The dynamic pressure is given by [6]

$$q = \frac{1}{2} \rho v^2 \quad (3.62)$$

where ρ is, here, the density of the air given in kg/m^3 and v is the velocity of the rocket given in m/s .

The density of air differs depending on the temperature, moisture and altitude. For this thesis it is assumed a constant temperature of 20 degrees Celsius (293.15 K) and exclude the moisture. The density of air can then be expressed as [6]

$$\rho = \frac{P}{RT} \quad (3.63)$$

where R is the universal gas constant (287.05 J/kg-K), T is the temperature in Kelvin, and P is the pressure given by the equation below [7],

$$P = P_0 \left(1 - \frac{L \cdot z}{T_0}\right)^{\frac{g \cdot M}{R \cdot T}} \quad (3.64)$$

$L = 0.0065K/m$, $T_0 = 293.15K$, $M =$, molar mass, $0.028965kg/mol$, R , universal gas constant, $= 8.314J/K \cdot mol$, $P_0 = 101325 Pa$, $g = 9,82m/s^2$ [6]. Inserting the variables into the equation,

$$P = 101325 \cdot (1 - z \cdot 0.0000225577)^{5.2559} \quad (3.65)$$

where z is the altitude. From this, the density of the air can be calculated as a function of altitude. The formula is then given by

$$\rho(z) = \frac{101325 \cdot (1 - z \cdot 0.0000225577)^{5.2559}}{287.05 \cdot 293.15} = 1.20412 \cdot (1 - z \cdot 0.0000225577)^{5.2559} \quad (3.66)$$

Using equation 3.62 and 3.66, the dynamic pressure can be written as a function of altitude and velocity.

$$q(z, v) = \frac{1}{2} \rho(z) v^2 \quad (3.67)$$

Chapter 4

Mandrel

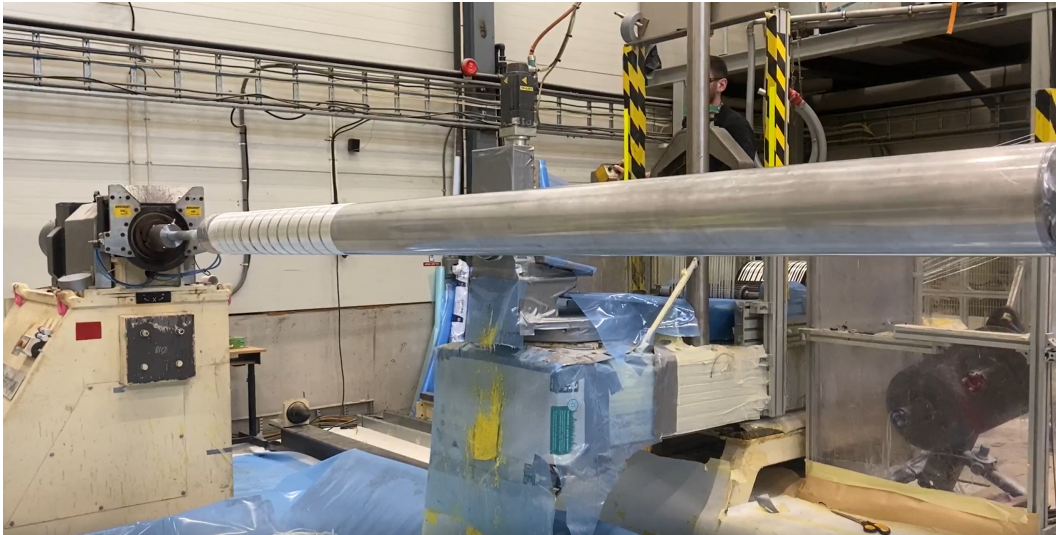


Figure 4.1: picture of the mandrel in use

The mandrel is the shape of which the glass fiber is wound upon during the filament winding process. This chapter will describe the design and structural calculation for the mandrel.

Design

In order to use the manufacturing company's winding machine, a custom designed mandrel, Figure 4.2 is needed, which needs to adhere to the specifications of this project. Firstly, the mandrel must have an outer diameter of 150mm through its entirety to get an inner diameter of 150mm, since the glass-fiber material get winded directly on the mandrel. Secondly, in order to get the desired length of 2 meters, the mandrel has to be slightly longer. This is due to the fact that the machine will need to readjust its angle of operations when turning. By adding 0.5 meters of clearance on both sides of the mandrel, the machine will get the length needed to readjust the angle so that the machine can operate at the desired angle through the entirety of the desired part.



Figure 4.2: Mandrel Assembly

A winding adapter, Figure 4.3, is necessary in order to connect the mandrel to the machine. The winding adapter adheres to certain specifications defined by the manufacturing company. The requirements that are in place define most of the geometry of the adapter, especially the end, that integrates with the machine. While the majority of the adapters shape is dictated by the requirements, the other end, meant for the mandrel, allows for certain design alterations. The design alterations encompass the addition of a hole to accommodate a shaft, and the installation of a side-mounted bolt for securing the shaft.



Figure 4.3: Winding adapter

The shafts function with a dual purpose - each filling a necessary 0.5 meter gap, collectively allocating the mandrel within the carriage's effective range, while also serving as connectors between the mandrel and the winding adapters. These shafts are dimensioned to a length of 0.6 meters to compensate for length lost from shaft connections. To connect the shafts to the mandrel, a method using a reduction liner, Figure 4.4(a), and a connector flange, Figure 4.4(a) is utilized. The reduction liners are welded just inside the ends of the mandrel, Figure 4.4(b). The shafts are welded to the connector flange, Figure 4.4(a). Following that, the connector flange is placed onto the reduction liner using screws, forming a secure connection.

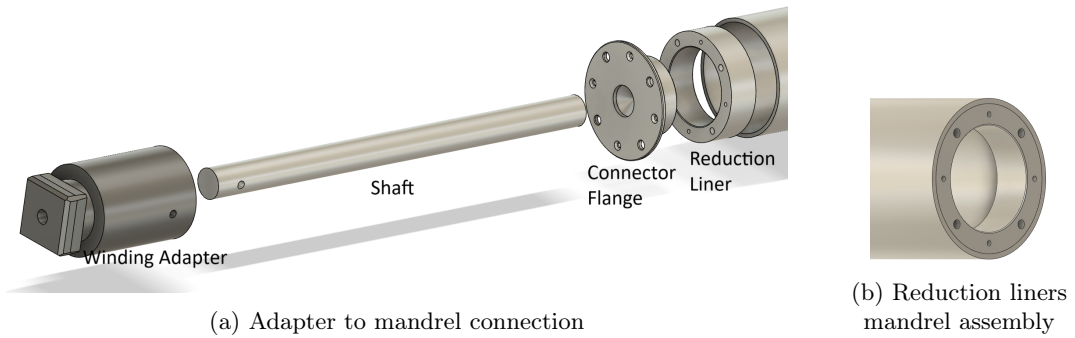


Figure 4.4: Detailed mandrel representation

To facilitate the extraction of the laminate from the mandrel upon completion of the winding process, an extraction tool, Figure 4.5, is integrated to the mandrel assembly. Designed with an inner diameter closely matching that of the mandrel, the extraction tool ensures a tight fit to prevent any space for the laminate, Figure 4.6. By utilizing bolts connected to the mandrel's reduction liner, the extraction tool applies significant force onto the end of the glass-fiber laminate. There are a total of 4 bolts, that are placed in a symmetric pattern, in order to generate a uniformly distributed force, ensuring that the extraction tool will push the laminate uniformly off the mandrel.



Figure 4.5: Extraction tool

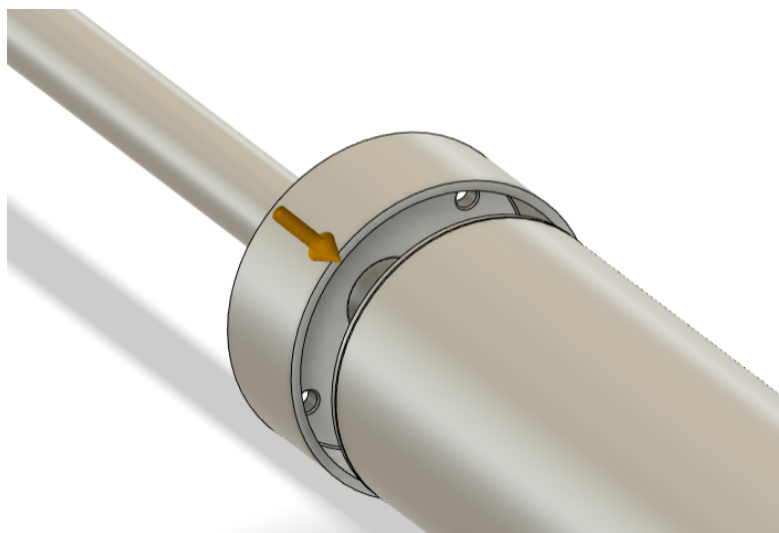


Figure 4.6: Extraction tool mandrel application

Dimensions of mandrel components

The shaft's diameter is dimensioned according to strength calculations, ISO 286-1 [8], and ISO 286-2 [9]. The strength calculations, particularly regarding deflection and shaft welds, confirmed the feasibility of using 40mm shaft diameter. The initial selection of this diameter stemmed from the availability of 40mm rods at the workshop. See appendix for the calculations, E.2 and E.3, respectively.

For the shaft connections, particularly those to the winding adapter and the mandrel, holes were assigned an E11 tolerance range of +60 to +250 μm , while shafts were assigned an E13 tolerance range of -50 to -440 μm , ensuring a good fit, according to [8] and [9].

Failure Analysis

Extraction tool failure analysis

The extraction tool is designed to endure significant bending and shear stresses during the extraction process. It is essential that the tool is capable of generating the required force for extraction. The Von Mises stress failure criteria, Figure 4.7, is utilized in order to determine its viability. A total force of 20kN was estimated for the analysis, evenly distributed among the 4 bolts. The safety factor varies primarily between 1.6 to 8, depending on the analysed location, with the lowest values located near the bolt connections. This implies that the extraction tool will be capable of exerting a force of 20 kN, while maintaining a safety factor of 1.6. The bolts will be in full tension due to other forces being negligible by comparison. This means that the bolts will not fail before the tensile capacity is reached, which was determined as 18.56kN [10] for each bolt. This means that bolts utilized for generating the force of the extraction tool will be amply adequate. For Calculations of the tensile capacity see appendix E.4. Hand calculations regarding how the connector flange weld is affected from the usage of the extraction tool is listed in appendix E.3.

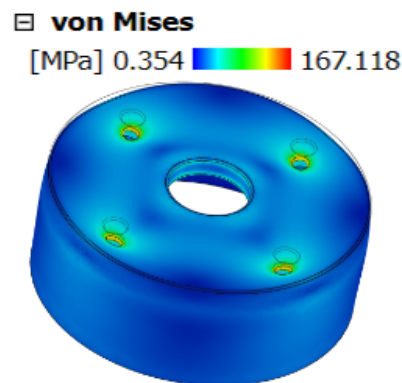


Figure 4.7: Von Mises stress analysis on the extraction tool

FEA of the Mandrel

To finalise the calculations of the mandrel an Ansys simulation of the production process is a good presentation if the structural integrity of the assembly is strong enough. This includes The assembly of all parts including welds and an estimate of the environment in which the production will take place.

Deflection Analysis

From this analysis the relevant results is the maximum deformation, the reason being the target specifications from the manufacturer described in Section 2.3. The specified maximum deformation allowed is 2-3mm, which is larger than the maximum deformation resulting from the deformation analysis which is given as 0.88327mm, see Figure 4.8. This is a positive result indicating that the structural integrity of the mandrel is strong enough to be utilized in the manufacturing of the fuselage. For deflection hand calculations see appendix E.2.

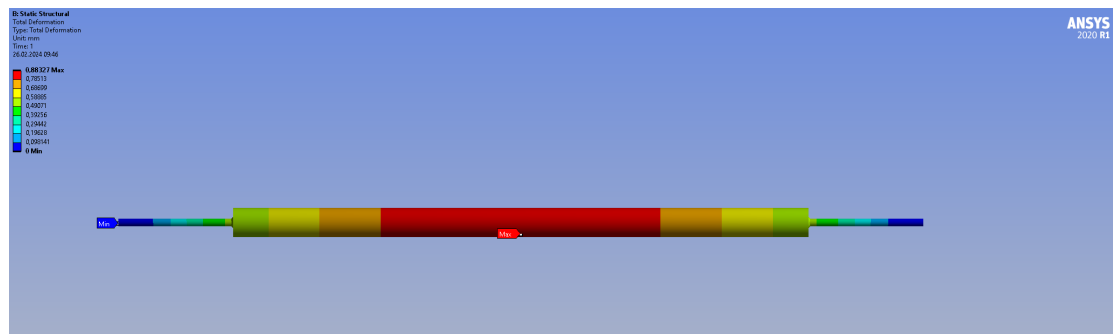


Figure 4.8: Deformation Analysis in Ansys

Stress Analysis

The maximum equivalent stress depicted in Figure 4.9, $\tau_{max} = 9.18MPa$, remains within the permissible limits for the welds, set by weld failure criteria, Table A.3, for assured yield strength and assured ultimate tensile strength of $0.4S_y = 96MPa$ and $0.3S_{ult} = 88.5MPa$, respectively. In comparison to the failure criteria on the shaft, such as bending, this equivalent stress is negligible, indicating no risk of failure for the shaft and mandrel. For weld hand calculations see appendix E.3.

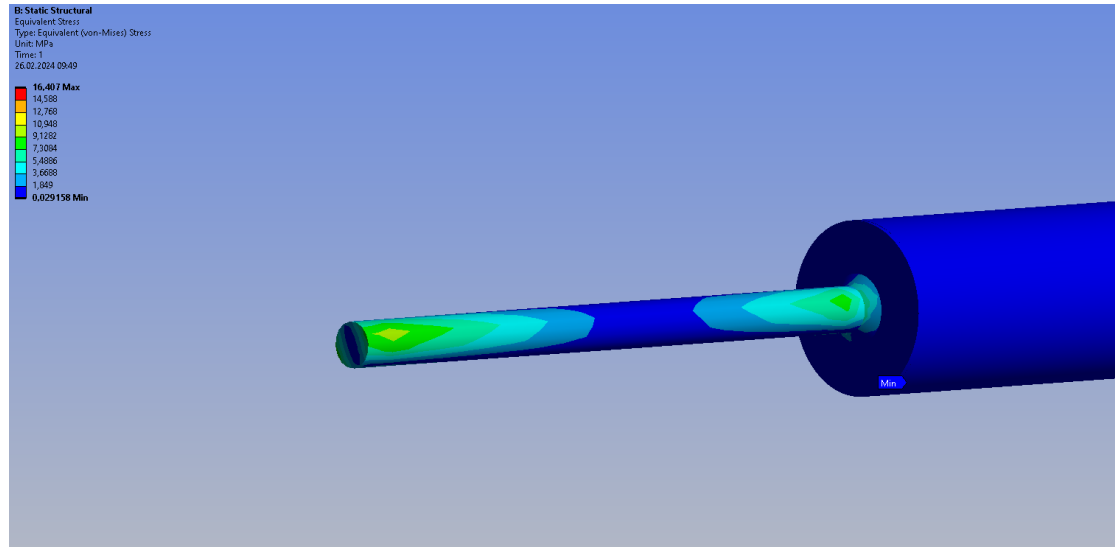


Figure 4.9: Equivalent Stress analysis of the Flange & shaft

Chapter 5

Filament Winding

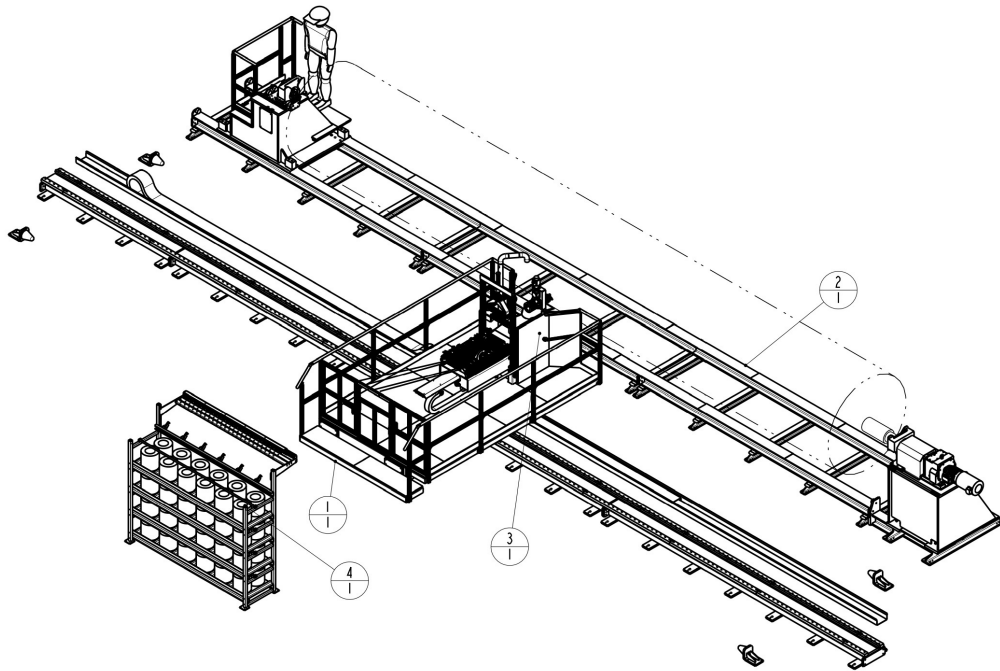


Figure 5.1: Winding Machine [11]

Filament winding is a specific method of making composite filament structures. It is widely used in industry for things like piping, rotors, pressure vessels, and rockets. [12] The winding machine is a large industrial machine consisting of multiple independently moving systems. These systems need to work cohesively to obtain the desirable structural integrity and dimensions. Several software applications specialize in generating patterns for filament winding, creating the path that the machine will follow. This chapter will explore the filament winding method, the machine used in the method and give an introduction to CADWIND.

Understanding Filament Winding

In filament winding, fiber spools are spooled together to form a total bandwidth before being wetted by a resin and then uniformly and regularly wound around a rotating mandrel. The payout eye and resin impregnation is part of the carriage unit which travels along a pre-described path parallel to the mandrel, see Figure 5.2. The speed of the carriage unit and the angular velocity of the mandrel determines the pattern in which the fiber is applied. [12]

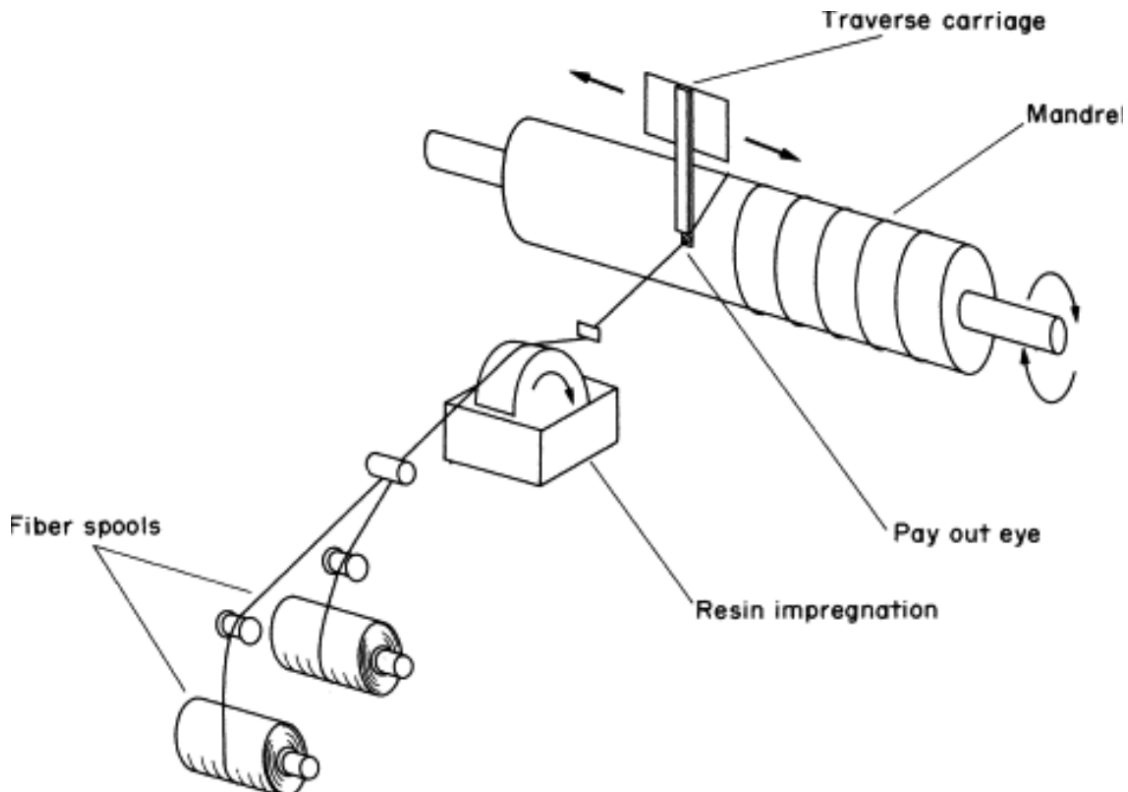


Figure 5.2: Filament Winder [12]

After the winding is done, the composite is cured by heating at a given temperature in an oven, autoclave or by exposure to IR radiation. During this process the filament will contract significantly, leading to a considerable pressure between the laminate and the mandrel. From here it is possible to remove the cured composite from the mandrel [12]. Some composites will stay on the mandrel throughout its life, but this will not be the case for this thesis. The removal will be done by a special self-produced extraction tool described in Chapter 4.

The principal advantage of filament winding over other methods for composite fabrication is the possibility of adopting automation and robotic procedures. The greatest disadvantage is the geometric limitation of available tools, including the inability to wind on negatively curved, concave, surfaces. [12]

Winding Machine

Spool Creel

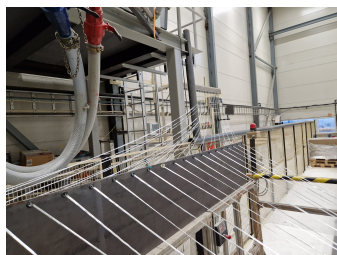
The process starts with the glass fiber coiled up in a spool creel, the spool creel is utilized as a small storage for glass fiber whilst it simultaneously is completely prepared to be unwound from the coils in order to prepare it for the composite filament winding process. These fibers make up the dispersed phase of the composite material that is made and shaped during the production process. For the glass fiber to be used further in the process the fibers are directly connected to the winding machine from the spool creel. To keep the fibers separated, the fibers are guided upwards from the coils whilst they are being pulled out of the spool creel.



Figure 5.3: Spool Creel [11]

Carriage Unit

The carriage unit is comprised of two primary components: the carriage unit Y (labeled 1.1) and the collection group (labeled 3.1) in Figure 5.1. While in use the carriage unit is mobile across tracks that are laid parallel to the mandrel. It traverses the tracks at a certain speed set by the CNC. The carriage unit Y shown in Figure 5.4a is necessary to keep the glass fiber in small amounts of tension for the ease of handling during the winding process. From the carriage unit Y, the glass fiber is impregnated with epoxy using the impregnation device, Figure 5.4b. This process involves guiding the glass fiber into a small container filled with epoxy, ensuring they do not overlap or intertwine. Before the glass fiber is wound on the mandrel it passes through the fiber delivery equipment, Figure 5.4c, consisting of delivery rings, payout eye and the delivery comb. This ensures the glass fiber is kept separate and in tension to ensure the winding process is as accurate as possible.



(a) Carriage Unit Y



(b) Resin Impregnation Device



(c) Fiber Delivery Equipment

Figure 5.4: Carriage Unit

Collection Assembly Platform

The collection assembly platform is where the filament winding process takes place. It consists of apparatuses designed for securing and rotating the mandrel. This platform features two spindle drives, Figure 5.5, on which the mandrel is mounted, along with the platform itself which is intended to collect potential drippage. To fasten the mandrel, standard-sized fasteners are utilized, shaped to fit the Winding Machine Adapter illustrated in Figure 4.3. An electric motor powers one of the spindle units, enabling mandrel rotation. The mandrel's rotation speed is closely tied to the carriage unit's velocity. Consequently, these speeds are carefully controlled by the CNC to ensure precise winding execution and maintain the desired relationship between these variables.



Figure 5.5: Collection assembly platform

CADWIND

CADWIND is a specialized software designed for generating part programs tailored for filament winding machines. It not only generates these programs but also offers simulation capabilities to detect errors prior to program deployment on the machine. For this thesis, the "Circular cross-section" mode is used in CADWIND, and therefore, this mode will also be utilized in this step-by-step explanation of how part programs are created.

Mandrel Creation

The first step in making a part-program, is making a mandrel to revolve around. To do this, use the drop-down menu and select "New Mandrel". A menu will then be opened with some parameters that needs to be filled out, see Figure 5.6b.

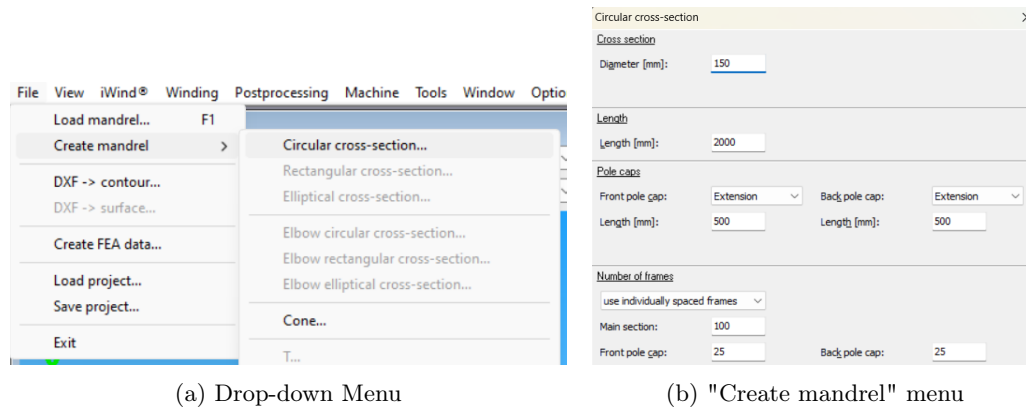


Figure 5.6: Create mandrel

The cross section and length are the first things to decide. These are the physical dimensions of the mandrel.

The pole caps are the area designated for turning. This means that this area is primarily meant to be used as a space for the carriage to slow down and reverse the angle. Here, the pole caps are extensions of the mandrel, both 500mm long, making the total length of the mandrel 3 meters.

The numbers of frames defines how many sections the mandrel is pieced into. 100 frames for the main section, and 25 frames for each pole cap is chosen for this thesis. Making the total amount of frames 150.

After finishing this step, a window with the finished mandrel will appear, example of such a view, with filament, can be seen in Figure 5.10.

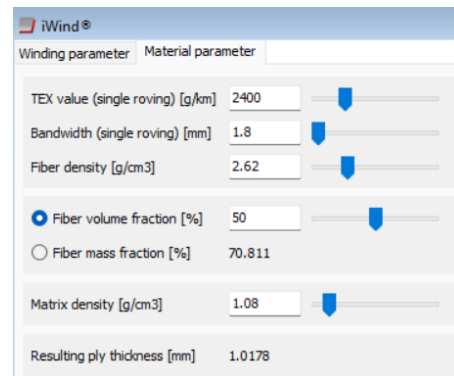
iWind

iWind is the part of CADWIND that computes the optimal path of the winding machine. Using the material parameters shown in Figure 5.7, and the winding parameter in Figure 5.8, the program can compute all the different patterns live. The material parameters are provided by the manufacturer, while the winding parameters are tailored to the mandrel specifications.

Material properties

When first opening iWind from the top menu, flip to the "Material parameter"-tab. Here, the material properties must be entered for the program to compute correct patterns.

The TEX value, bandwidth for a single roving, and fiber density are manufacturer-provided parameters specific to the glass fiber used, aiming for a fiber volume fraction of 50-55% and a matrix density of 1.08 g/cm^3 . These settings result in a ply thickness of approximately 1 mm, aligning with the specific fiber used, SE 3030, see Figure A.1.



Winding parameter	Material parameter
TEX value (single roving) [g/km]	2400
Bandwidth (single roving) [mm]	1.8
Fiber density [g/cm3]	2.62
<input checked="" type="radio"/> Fiber volume fraction [%]	50
<input type="radio"/> Fiber mass fraction [%]	70.811
Matrix density [g/cm3]	1.08
Resulting ply thickness [mm]	1.0178

Figure 5.7: iWind - Material Parameters

Winding Parameter

The winding parameters gives the information needed to generate patterns. Starting from the top left on Figure 5.8, the starting frame and position gives the position, on the mandrel, on which to start the pattern. This number is given in the range of the number of frames on the mandrel. The turning zones, in the top right, describes where the turning zones will be.

Following that, the winding angle, friction factor, and total bandwidth require adjustment. The winding angle dictates both the filament's angle of application onto the mandrel and its resulting strength. The friction factor represents the resistance between the filament and the mandrel during winding, typically ranging from 0.12 to 0.16 according to the manufacturer OPS Composite Solutions, while the total bandwidth specifies the filament's width upon application to the mandrel, set between 10 and 25 as detailed in Section 2.3. Lastly, the coverage range, in the bottom right, determines the extent to which the mandrel will be covered upon completion of the winding process.

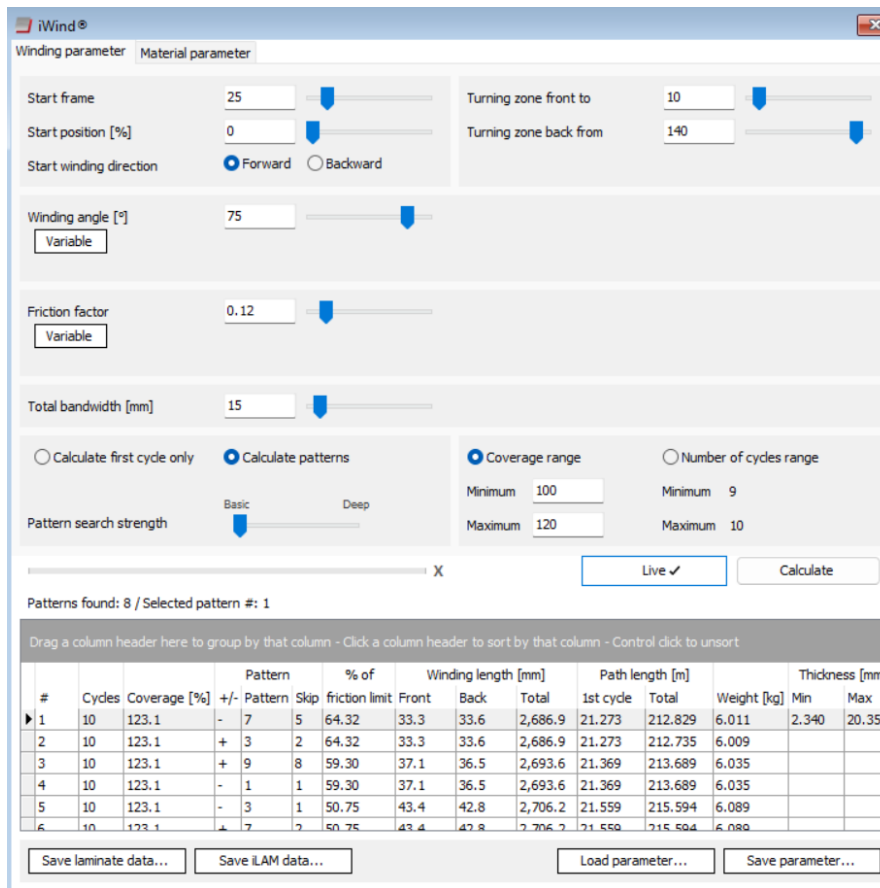


Figure 5.8: iWind - Winding Parameters

Machine parameter

Adding the machine parameters are also important. As many machines are different it is vital to simulate the path and speed of the carriage with the right parameters to make sure the program will work. The parameters were given by the manufacturer, but some can also be found in, the machine manual [11].

Post-Process

When all parameters are given, and the wanted pattern is picked, the post-processing can begin. By clicking the Post-processing menu at the top, shown in 5.9, the pattern can be simulated using the "Control data" feature. This will save the pattern and show the simulation in the mandrel view.

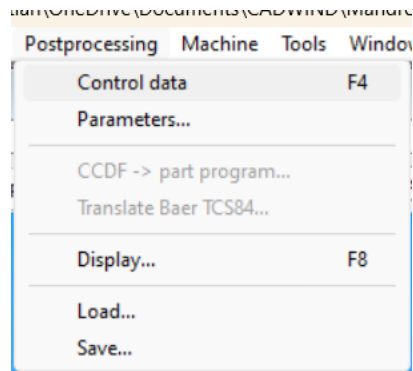


Figure 5.9: Post-processing menu

The Figure 5.10 below, shows the final view of the mandrel with the filament applied. This figure additionally shows the laminate thickness throughout the mandrel. It is visible that the ends, or turning zones, have the thickest stack of laminates.

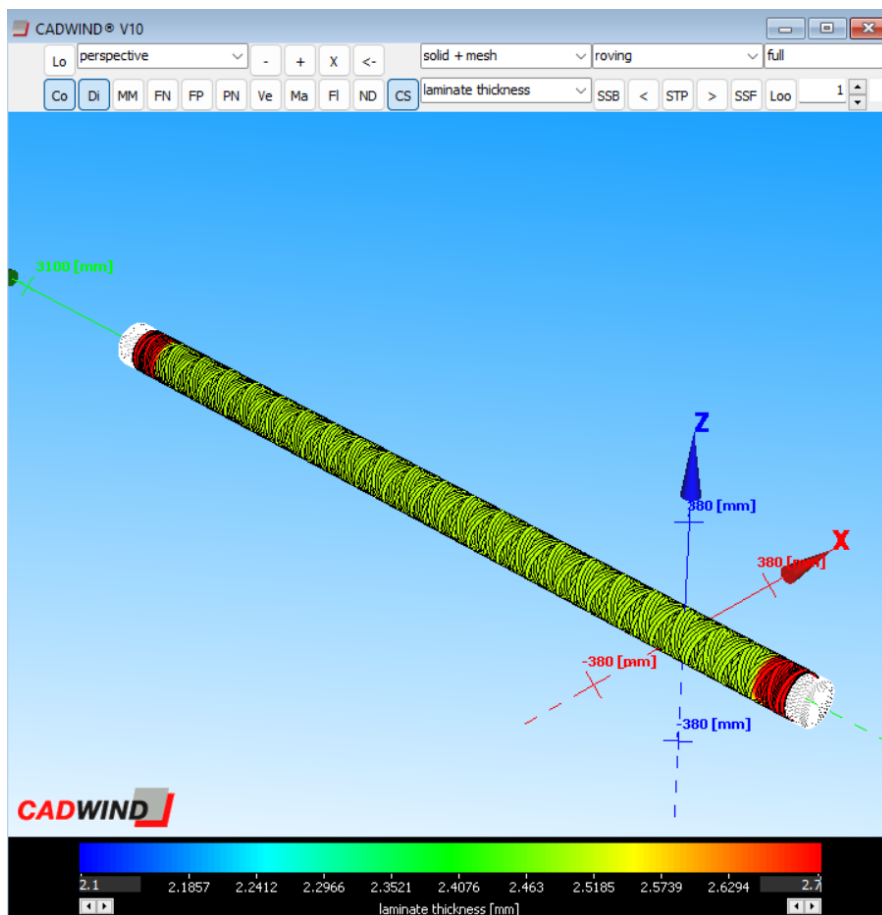


Figure 5.10: Filament thickness on a mandrel

Chapter 6

Fiber Angle Optimization

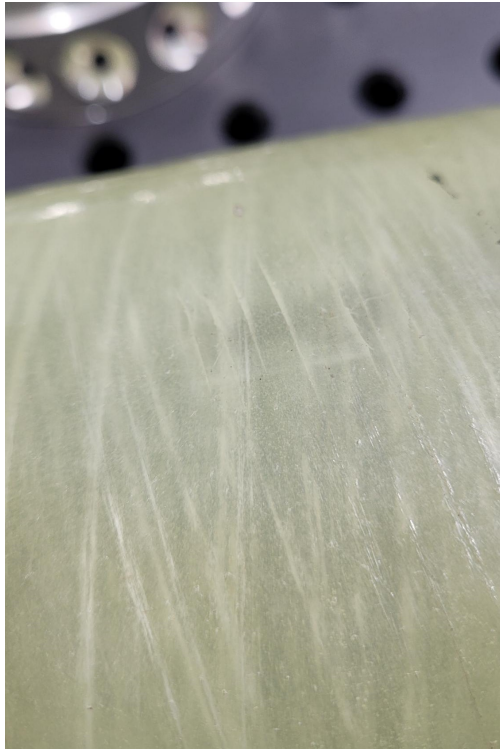


Figure 6.1: Picture of the fuselage, showing the fibers within

The alignment of fibers stands as a fundamental parameter in delineating the structural integrity of the framework. As the fuselage strength in this thesis hinges on dynamic pressure calculations, the initial focus of this chapter is placed on determining the Max Q. Subsequently, the impact of fiber angles on both the Tsai Wu Failure Index and Factor of Safety is investigated through Python simulations and the manufacturing software CADWIND.

Calculating Max Q using OpenRocket

By using the free software OpenRocket the flight of the rocket can be simulated to an acceptable degree. Adding all the different parameter for the rocket, as it is projected, one will get a graph of the flight itself with all the different parameter chosen.

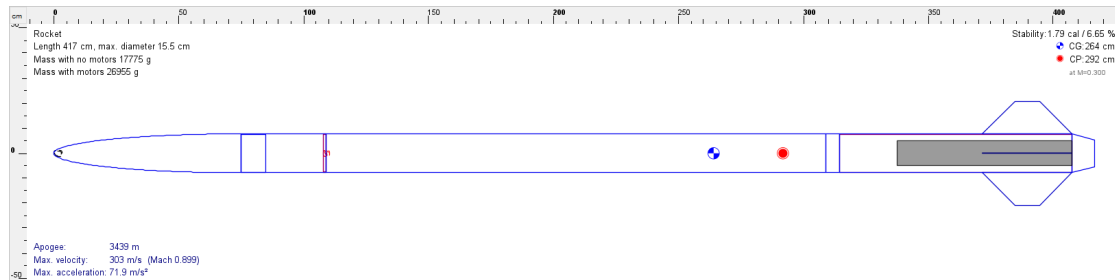


Figure 6.2: OpenRocket model

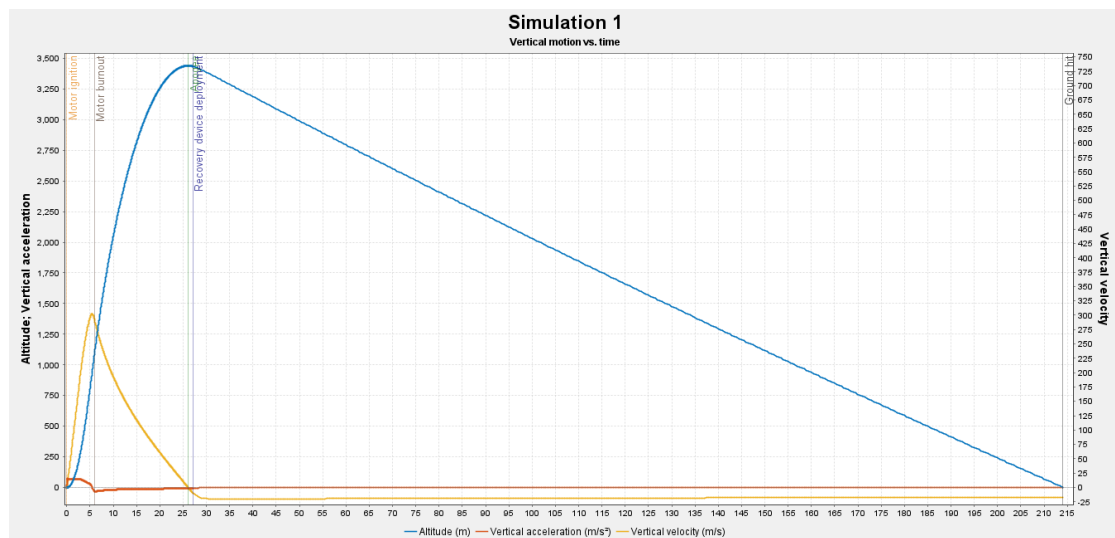


Figure 6.3: OpenRocket graph

The data from the simulation can be used alongside the dynamic pressure equations from Section 3.2, integrated into a python script, Figure B.1, yielding the dynamic pressure calculated to be 51.496 kPa.

```
Max Q is: 51496.46 Pa. Which is 50.82% of the static pressure
```

Figure 6.4: Output of Python program for estimating maximum dynamic pressure

Python Code for Optimal Angle Determination

A python code is constructed to exploit the usage of computing power to help define the usability of different fiber angles. 10000 different fiber angles from 0 to 90 degrees are calculated and utilized to plot both the Tsai-Wu FI and factor of safety. These values are chosen because they speak of the reliability of the fuselage when the production is completed. These relationships are then explored with the manufacturing process in mind to conclude the optimal fiber angle. The code is listed in its entirety in figures B.2 & B.3.

Explaining the code

The initial lines of the code define geometric and load values that are calculated and listed in chapters 2.3 & 3.2, such as the diameter, number of plies, thickness and the dynamic pressure. The material properties and stress limits are then defined by the manufacturer in tables A.1 & A.2. These values are then applied to define the force from the external pressure.

```
1 p = 51496.46      #pressure
2 dia = 0.15        #diameter
3 NP = 2           #nr of plies
4 h = 2*10**(-3)   #thickness
5
6 #material properties
7 E_1 = 41.05*(10**9)
8 E_2 = 6.43*(10**9)
9 v_12 = 0.325
10 G_12 = 2.38*(10**9)
11
12 #orthotropic stress limits
13 sigma_1_T = 963.7*(10**6)
14 sigma_1_C = 574.7*(10**6)
15 sigma_2_T = 19.93*(10**6)
16 sigma_2_C = 26.36*(10**6)
17 tou_12_F = 40.46*(10**6)
18
19 z = [] #Creates a list of length, z, for each layer, from the top.
20 for i in range(0,3):
21     z.append(i*10**(-3))
22
23 N_y = 1/2 * p * dia #Force from external pressure on a pressure vessel
```

Further on it was necessary to construct a list with all the angles to be used in further calculations. This list contains 10000 angles from 0 to 90 degrees. The angles will be used in the calculations one by one to collect points that can be further used to create a spline showcasing the different relationships.

```
1 angle = np.linspace(0,(np.pi / 2) , 10000) """creates a list with 10000
2                                     values from 0 to 90 degrees"""
```

To begin the calculations there are necessary engineering constants that can be calculated from the material properties. These are calculated with the equations in the appendix D.1, D.2, D.5 and D.12. Further the reduced stiffness members are calculated with equations in the appendix D.26 - D.28.

```
1 #engineering constants
2 S11 = 1 / E_1
3 S12 = - (v_12 / E_2)
4 S22 = 1 /E_2
5 S66 = 1 / G_12
6
7 # reduced stiffness members
8 Q11 = S22 / ((S11 * S22) - (S12 * S12))
9 Q12 = - S12 / ((S11 * S22) - (S12 * S12))
10 Q22 = S11 / ((S11 * S22) - (S12 * S12))
```

The definition of a function is used to make use of one of their properties, which is the ability to utilize these calculations through multiple iterations and through different angles. First, define a list with the variable phi. This is to make sure both the positive and negative angle is available for use in further calculations. In the definition of this function multiple variables are defined as zero, these are not intended to stay at zero and will change through the calculations. It is important that these variables are defined outside of the upcoming for-loop to avoid them being reset to zero for every iteration of the loop.

```
1 def Local_Stresses(phi):
2     x = [phi, -phi]
3     A11 = 0; A12 = 0; A16 = 0; A22 = 0; A26 = 0; A66 = 0
4     B11 = 0; B12 = 0; B16 = 0; B22 = 0; B26 = 0; B66 = 0
5     D11 = 0; D12 = 0; D16 = 0; D22 = 0; D26 = 0; D66 = 0
```

The for-loop, shown below, is based on the number of plies, in this case it will loop twice because of the two layers. This loop is necessary to define the final stiffness matrix that are dependent on both plies. The calculations is structured to make use of the positive angle for the first iteration of the loop, and the negative angle for the second iteration. The equations used to calculate the transformed reduced stiffness members are equations 3.20 - 3.25.

```

1  for k in range(NP):
2      QQ11 = Q11 * (m.cos(x[k])**4) + 2 * ((Q12 + 2 * Q66) * (
3          m.sin(x[k])**2) * (m.cos(x[k])**2)) + Q22 * m.sin(x[k])**4
4      QQ12 = (Q11 + Q22 - 4*Q66)*(m.sin(x[k])**2) * (
5          m.cos(x[k])**2) + Q12*(m.sin(x[k])**4 + m.cos(x[k])**4)
6      QQ16 = (Q11 - Q12 - 2*Q66)*(m.sin(x[k]))*(m.cos(x[k])**3) + (
7          Q12 - Q22 + 2*Q66)*(m.sin(x[k])**3)*(m.cos(x[k]))
8      QQ22 = Q11*(m.sin(x[k])**4) + 2*(Q12 + 2*Q66)*(m.sin(x[k])**2)*(
9          m.cos(x[k])**2) + Q22*(m.cos(x[k])**4)
10     QQ26 = (Q11 - Q12 - 2*Q66)*(m.sin(x[k])**3)*m.cos(x[k]) + (
11         Q12 - Q22 + 2*Q66)*m.sin(x[k])*m.cos(x[k])**3)
12     QQ66 = (Q11 + Q22 - 2 * Q12 - 2 * Q66)*(m.sin(x[0])**2)*(
13         m.cos(x[k])**2) + Q66 * ((m.sin(x[k])**4) + m.cos(x[k])**4)

```

The code below creates the ABD matrix used in equation 3.39, enabling the creation of a relation that goes from forces and moments, to strain and transverse strain. These permanent additions are necessary to complete the sums from equations 3.40 - 3.42. This marks the end of the for-loop and the first section the angle has been used in the function.

```

1  #calculating values for the ABD matrix
2  A11 += QQ11 * (z[k+1] - z[k])
3  A12 += QQ12 * (z[k+1] - z[k])
4  A16 += QQ16 * (z[k+1] - z[k])
5  A22 += QQ22 * (z[k+1] - z[k])
6  A26 += QQ26 * (z[k+1] - z[k])
7  A66 += QQ66 * (z[k+1] - z[k])
8
9  B11 += (1/2) * QQ11 * (z[k+1]**2 - z[k]**2)
10 B12 += (1/2) * QQ12 * (z[k+1]**2 - z[k]**2)
11 B16 += (1/2) * QQ16 * (z[k+1]**2 - z[k]**2)
12 B22 += (1/2) * QQ22 * (z[k+1]**2 - z[k]**2)
13 B26 += (1/2) * QQ26 * (z[k+1]**2 - z[k]**2)
14 B66 += (1/2) * QQ66 * (z[k+1]**2 - z[k]**2)
15
16 D11 += (1/3) * QQ11 * (z[k+1]**3 - z[k]**3)
17 D12 += (1/3) * QQ12 * (z[k+1]**3 - z[k]**3)
18 D16 += (1/3) * QQ16 * (z[k+1]**3 - z[k]**3)
19 D22 += (1/3) * QQ22 * (z[k+1]**3 - z[k]**3)
20 D26 += (1/3) * QQ26 * (z[k+1]**3 - z[k]**3)
21 D66 += (1/3) * QQ66 * (z[k+1]**3 - z[k]**3)

```

The previously calculated values are thereafter used to construct an array. Arrays can be utilized as a matrix in the python environment because of the similar features. This array is therefore interchangeable to the ABD matrix. The ABD array is then subsequently inverted for further usage.

```

1      #creates the ABD array
2      ABD = np.array([[A11, A12, A16, B11, B12, B16],
3                     [A12, A22, A26, B12, B22, B26],
4                     [A16, A26, A66, B16, B26, B66],
5                     [B11, B12, B16, D11, D12, D16],
6                     [B12, B22, B26, D12, D22, D26],
7                     [B16, B26, B66, D16, D26, D66]])
8
9      abd = np.linalg.inv(ABD) #invertes the ABD array

```

Through simplifications, the equations 3.45 - 3.50 can be used to assess the surface extensional strain, ε_x^0 , ε_y^0 , and the surface in plane shear strain γ_{xy}^0 . The strains are further used to calculate the quantities k_x^0 and k_y^0 . These variables are subsequently used to calculate the strains ε_x , ε_y and γ_{xy} from equations 3.26 - 3.37.

```

1      #strains
2      epsilon_x0 = abd[0,1] * N_y
3      epsilon_y0 = abd[1,1] * N_y
4      gamma_xy0 = abd[2,1] * N_y
5      k_x0 = abd[3,1] * N_y
6      k_y0 = abd[4,1] * N_y
7      k_xy0 = abd[5,1] * N_y
8
9      epsilon_x = epsilon_x0 + (h/2) * k_x0
10     epsilon_y = epsilon_y0 + (h/2) * k_y0
11     gamma_xy = gamma_xy0 + (h/2) * k_xy0

```

Further on, in the code below, a reduced stiffness matrix is constructed with the reduced stiffness parameters previously calculated. These are values that correspond only to the negative angle phi. This is a simplification made due to the fact that the optimal angle for one single ply will correspond to the optimal angle with two plies. This occurs because the angles are constructed of equal scale, the only difference is one ply will have the negative value of the other.

```

1      QQ = np.array([[QQ11, QQ12, QQ16],
2                    [QQ12, QQ22, QQ26],
3                    [QQ16, QQ26, QQ66]])

```

From equation 3.38 the stresses can be calculated using the code below. The function that completes the matrix multiplication is imported from numpy. Further, a transformation matrix T is constructed as an array with equation 3.17.

```

1     [sigma_x, sigma_y, tou_xy] = np.matmul(QQ,
2                                         [epsilon_x, epsilon_y, gamma_xy])
3
4     T = np.array([[m.cos(phi)**2, m.sin(phi)**2, 2* m.cos(phi) * m.sin(phi)],
5                  [m.sin(phi)**2, m.cos(phi)**2, -2 * m.cos(phi) * m.sin(phi)],
6                  [-m.cos(phi) * m.sin(phi), m.cos(phi) * m.sin(phi),
7                  m.cos(phi)**2 - m.sin(phi)**2]])

```

To present the stresses they are transformed from global to local coordinates before being returned. The stresses are presented in local due to the nature of how Tsai-Wu Failure Criteria is calculated.

```

1     [sigma_1, sigma_2, tou_12] = np.matmul(T, [sigma_x, sigma_y, tou_xy])
2
3     return [sigma_1, sigma_2, tou_12]

```

A function that can calculate the Tsai-Wu FI from equation 3.51 is then defined to be used further. This function is intended to utilize the numerical results from the Local_Stresses function.

```

1     def Tsai_wu(stress):
2         return (F_1 * stress[0]) + (F_2 * stress[1]) + (F_11 * (stress[0]**2)) + (
3         F_22 * (stress[1]**2)) + (F_66 * (stress[2]**2)) - (
4         m.sqrt(F_11 * F_22) * stress[0] * stress[1])

```

To calculate the safety factor from equations 3.59 - 3.61, these values are to be further sorted to only enable the usage of the smallest positive value for plotting. The safety factor is also dependent on the stress values.

```

1     def Quad_safe(stress):
2         a = (F_11 * (stress[0]**2)) + (F_22 * (stress[1]**2)) + (
3         F_66 * (stress[2]**2)) - (m.sqrt(F_11 * F_22) * stress[0] * stress[1])
4         b = (F_1 * stress[0]) + (F_2 * stress[1])
5         d = (b**2) + (4*a)
6         sol1 = (-b-m.sqrt(d))/(2*a)
7         sol2 = (-b+m.sqrt(d))/(2*a)
8         return [sol1, sol2]

```

The empty lists created are lists that will contain the numerical solutions. The list named "failure" is intended to accommodate all the numerical solutions for the safety factor, this includes both the possible numerical solutions from the quadratic equation 3.59. The lists Tsai-Wu1 and Tsai-Wu2 are intended for the Tsai-Wu FI and the Safety factor, respectively. The list containing all solutions for the failure index is then sorted into Tsai-Wu1 with only the smallest positive solution being appended.

```
1 #creating necessary empty lists
2 tsai_wu1 = []
3 tsai_wu2 = []
4 failure = []
5 #loop to calculate all angles
6 for phi in angle:
7     failure.append(Quad_safe(Local_Stresses(phi)))
8     tsai_wu2.append(Tsai_wu(Local_Stresses(phi)))
9
10 """only utilizing the smallest positive solution
11 for the failure index"""
12 for solution in failure:
13     if min(solution) <= 0:
14         tsai_wu1.append(max(solution))
15     else:
16         tsai_wu1.append(min(solution))
```

The numerical values that is included in the plot, is the lists Tsai-Wu1 and Tsai-Wu2 as well as the list containing all angles. These values are further plotted by the code in Figure B.3.

The Calculated Values

From Figures 6.5 and 6.6, it is evident that the optimal fiber angle against external pressure for this particular problem is 90 degrees, where the safety factor is high and the failure index is low. Additionally, the Tsai-Wu failure index satisfies the equation $FI < 1$ for all given angles, concluding that there is no precedence for predicted failure. This also matches nicely with the safety factor plot, as it never dips below one. This facilitates the incorporation of the product specifications, as there are no restrictions on the fiber angle parameter.

Optimal Angle by Safety Factor and Tsai-Wu

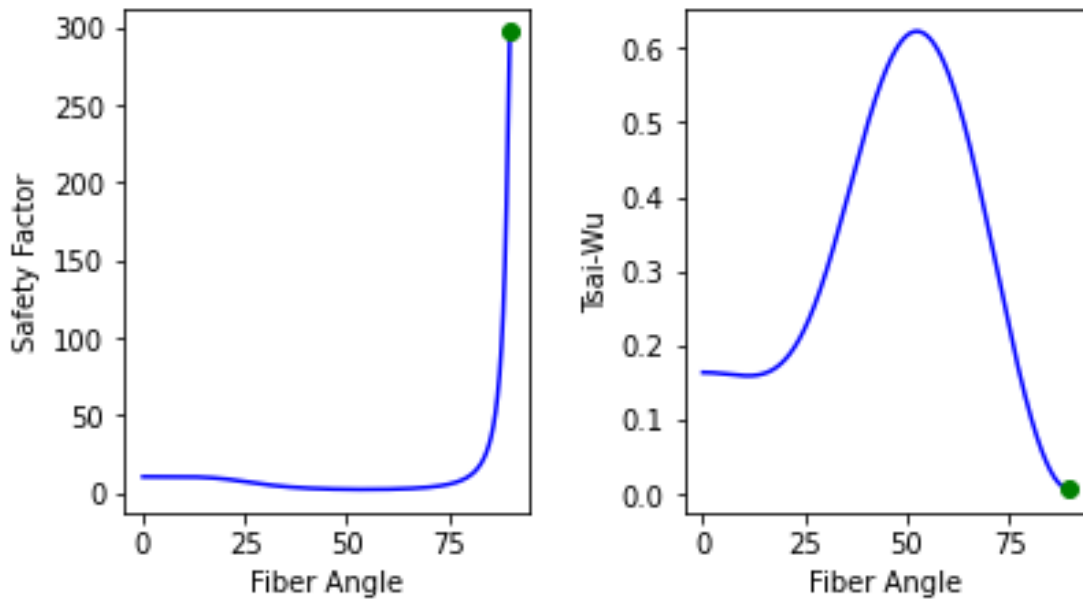


Figure 6.5: Python Script, Optimal Angle Plot

```
The optimal angle is 90.00000000 degrees
The safety factor here is 297.59974440 with a Tsai-Wu of 0.00535734
```

Figure 6.6: Python Script, Optimal Angle Print

Manufacturing consideration

The impact of changing the angle on the design parameters of the fuselage is illustrated in Figure 6.7. This change is reflected in the dimensions of the fuselage pattern. When the angle is adjusted to 20 degrees, the thickness of the fuselage is altered, resulting in an estimated thickness of 2.117mm. Resulting in the outer diameter of the fuselage shifting to 154.234 mm, which deviates from the specified 155 mm, and contradicting the product specifications. This particular pattern does not wind the glass fiber close to the ends of the mandrel, thereby affecting the functionality of the extraction tools. After a process of iteration through CADWIND simulations it seems like an angle of 70 degrees and a bandwidth of 20mm is the best for manufacturing.

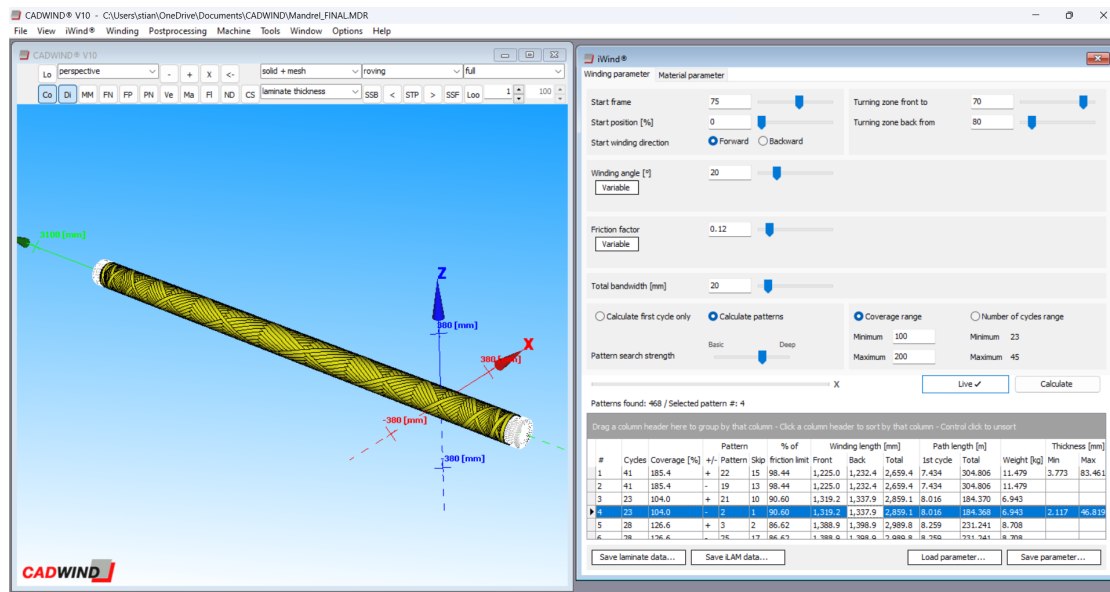


Figure 6.7: 20 degree fiber angle

Angle Determination

Seeing that the absolute minimal safety factor, according to Figure 6.5, is 2.6, it can safely be concluded that even if the worst angle is chosen the structure would still hold. Given this, the external pressure will be held. Because of the limitations of the filament winding technique the angle chosen for manufacturing ended up being 70 degrees with a bandwidth of 20mm. When applying loads at the ends of the fuselage the lower angles are more optimal, compared to the 90 degrees optimal for absorbing external pressures. This is a result because of the material properties of composite materials containing continuous fibers. The chosen parameters is shown in Figure 6.8.

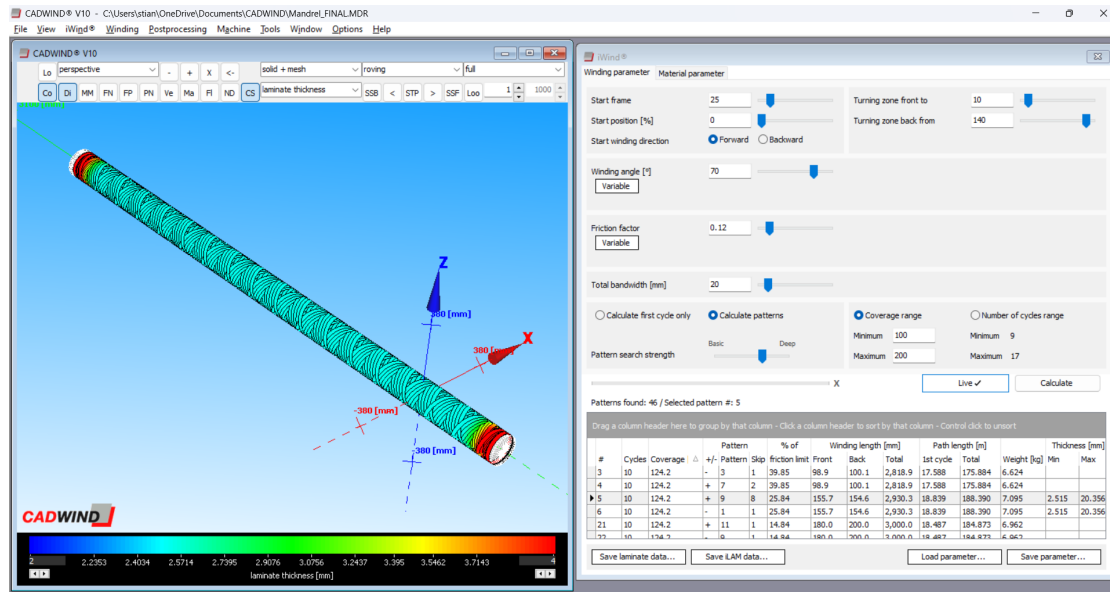


Figure 6.8: Parameters for manufacturing of the fuselage

There are multiple reasons for choosing these parameters. From section 2.3, both the bandwidth and total thickness of the fiber stack is given, between 10-25mm and 2.5mm, respectively. Looking at the pattern selected in Figure 6.8 the thickness is minimum 2.515mm, while the max is 20.256mm. The highest thickness will be at the ends, where the extraction tool will be placed to push off the wound fiberglass. The extra thickness on the ends is perfect, considering the extraction process, and will hopefully make the extraction process go smoothly. The bandwidth is within the specifications, and the thickness is as close as one could possibly hope to achieve. Considering all of this, there is likely no better pattern, considering the given parameters from the manufacturer, UIS Aerospace and the material itself.

Both the allowable pressure and safety factor for the pattern was also calculated. Figure 6.9 is calculated with the Mathematica program that comes with [1] and gives the allowable pressure for a given angle. It takes the material properties and Tsai-Wu into consideration, the same as the Python script for calculating the optimal angle. The safety factor for this angle is shown in Figure 6.10.

```
Out[2267]=
3.22544 × 10-6 p - 2.24575 × 10-12 p2

Out[2268]=
{{p → 452 767.}, {p → 983 476.}}
```

Figure 6.9: Allowable pressure for 70 degrees in pascal

The safety factor at 70 degrees is 3.539

Figure 6.10: Safety factor at 70 degrees

Chapter 7

Structural Analysis

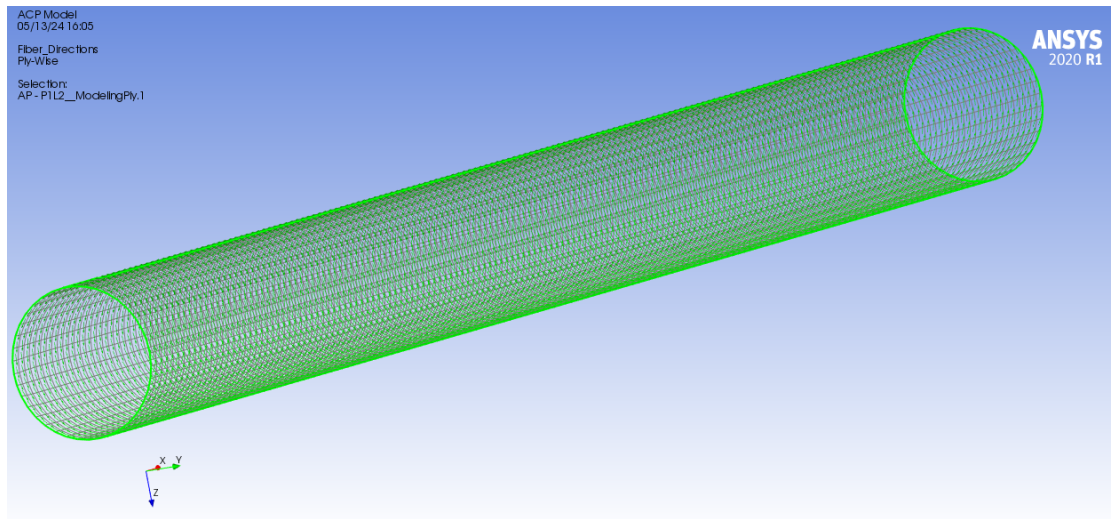


Figure 7.1: The fuselage in the Ansys ACP(Post) environment, with the vector field describing the fibres visible

From the workbench environment in Ansys Workbench 2020R it is possible to create a structural analysis of composite materials by using the features ACP(pre) and ACP(post) along with structural analysis. This chapter will describe this process and the results from the analyses.

Step by Step Utilizing Ansys Workbench

ACP(pre)

Step 1: Add ACP(pre) to the project schematic.

Step 2: Edit engineering data from workbench.

Step 3: Add a new material called GF_3030 and add the following Material.

- Orthotropic elasticity
- Orthotropic stress limits
- Orthotropic strain limits
- Tsai-Wu constants
- Ply-type

Step 4: Add the appropriate values, the values are displayed in Table A.1 & Table A.2.

Step 5: Edit Geometry from workbench

Step 6: Sketch a circle with $D = 152.5\text{mm}$ in the XY-plane. This diameter is chosen because it marks the average diameter of the Fuselage with respect to the outer and inner diameter.

Step 7: Utilize the pull function to create a surface the shape of a tube with a length of 2000mm.

- It is essential to remove the circular surface generated where the circle was drawn to ensure that only the surface boundary of the cylinder remains.

Step 8: Edit Model from workbench

Step 9: Insert refinement under mesh and add the cylinder as the surface.

Step 10: Insert Face meshing under mesh and add the cylinder as the surface.

Step 11: Insert Sizing under mesh and add the cylinder as the surface, set the element size to 25mm

Step 12: Mesh the model.

- Perform a visual check

Step 13: Under geometry set the thickness = 2.5mm

Step 14: Edit setup from workbench

Step 15: Create a fabric with the following

- Material: GF_3030
- Thickness = 0.00125 (This is read as meters)

Step 16: Create a stackup with the following fabrics and angle

- GF_3030 with angle 70deg
- GF_3030 with angle -70deg

Step 17: Create a rosette of the type Radical and name Rosette.1

Step 18: Create a Oriented Selection Set given the name OSS.1 with the following

- Element sets: "All_Elements"
- Point: Click on any point on the cylinder
- Rosette: Rosette.1

Step 19: Under "create Modelling group" Create plies with the following

- Oriented Selection set: OSS.1
- Ply material: Stackup

Static Structural

Step 1: Add Static structural to the project schematic and Connect setup from from ACP(pre) to model in Static structural

Step 2: Edit Setup in Static structural and add the following to the tube

- Fixed support on the edges
- Add inward pressure with value 52.3KPa, from section 3.2

ACP(post)

Step 1: Add ACP(post) to the project schematic and connect Engineering data, Geometry, and model from ACP(pre) to ACP(post). Connect the Solution from static structural to results in ACP(post).

Step 2: Edit Results in ACP(post)

Step 3: Under definitions create Failure criteria named FailureCriteria.1 with the following taken into account.

- Max Strain
- Max Stress
- Tsai-Wu
- Von mises

Step 4: Under Solutuion.1 Generate the following Solutions.

- Failure (utilizing FailureCriteria.1)
- Deformation

FEA on the Fuselage

Failure Analysis

Because the Fuselage’s dimensions are determined after the Tsai-Wu criterion, it is fitting to implement a final failure analysis of the entire fuselage with all the dimensions utilizing the Tsai-Wu criterion.

This analysis implements the fixed supports at each end of the structure and the external pressure, this results in the edges being more prone to Failure as depicted in Figure 7.2. Opposed to the previous simulations this analysis takes into account the existence of multiple layers, factoring in both layers of plies improves the structural integrity of the fuselage, resulting in a Tsai-wu failure index lower than previously estimated. The maximum failure index resulting from this analysis is $FI = 0.019466$ from Figure 7.2. This result is a constructive improvement compared to the previous simulations to optimize fiber angle, this yields in a more effective and durable design than previously assumed.

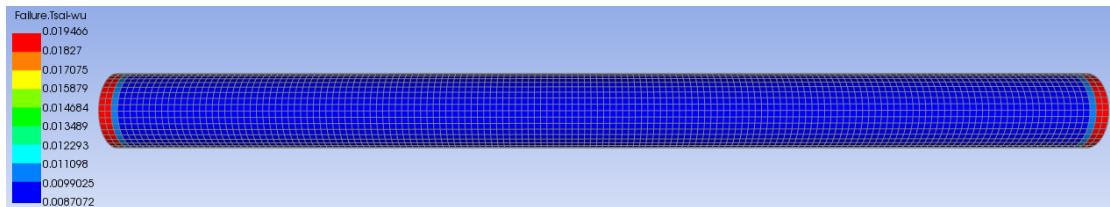


Figure 7.2: Tsai-Wu Analysis of the Fuselage

Deformation Analysis

The strength of the fiber material is greatly depicted and well represented through the deformation analysis shown below, Figure 7.3. From the figure, it can be seen that the predicted deformation is $\delta_{def} = 4.39 * 10^{-6}mm$. The value representing deformation is small enough to consider the effect on the fuselage. as well as other projects on the program. negligible.

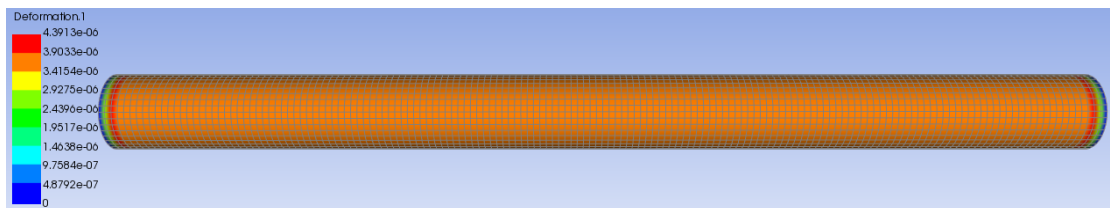


Figure 7.3: Deformation Analysis of the Fuselage

Addressing the Assumptions

Several assumptions are made for the simulation. Due to the design of the inner structure of the rocket, it is expected that there will be no tension or compression on the fuselage except for the thrust force. The engine is expected to provide a thrust of 3kN. Compression is considered negligible due to the lack of retention on the upper part of the fuselage. Fixed supports at both open ends of the fuselage are included because of a coupler at one end, and a radax-coupler at the other end.

The fundamental assumption that need to be considered when analysing the results is that the final design is not exactly equal to the design-parameters. These design parameters include; the thickness of the two plies and the continuously exact precision fiber angles. Due to the nature of the manufacturing process and the standard sizing of the fibers, it is not implied that there will be complete cover for both angles. However, it is anticipated that any areas lacking full coverage from both angles will be negligible in extent. The precision of the fiber angle cannot be guaranteed to be exact, as it is influenced by numerous variables including surface roughness and friction. Consequently, minor inaccuracies are expected to occur. Considering the assumptions, slight discrepancies are reflected in the numerical outcomes. Nevertheless, it is presumed that these variances are inconsequential, leading to the determination that the analysis possesses satisfactory precision.

Chapter 8

Manufacturing



Figure 8.1: The rocket fuselage, view of both the front and back side

This chapter will be explaining the manufacturing process itself. The chapter will be arranged sequentially according to the order of the steps taken.

Setup

After connecting all the mandrel components together, a crane was used to lift the mandrel in order to ease the process of connecting the mandrel to the machine. The winding machine proved to be sensitive to minor asymmetry in the alignment of the winding adapters, leading to difficulty in connecting the mandrel to the machine. The asymmetry was caused by minor angular imprecision's from welding the shaft together with the connector flange. Ultimately, by adjusting the spindle drives in order to compensate for this asymmetry the mandrel was mounted on the collection assembly platform.

Changes to the Angle

Before arriving at OPS Composite solutions, the fiber angle deemed as the best configuration was an angle of 70 degrees, leading to a pattern that would generate the closest match to the specified outer diameter while remaining strong enough for the purpose. However, during manufacturing the total bandwidth of the fiber material was changed from the initial specifications. Originally, a total bandwidth of 20mm was specified, but this was changed to 44mm. The reason being that the total bandwidth of the fiber prepared in the machine's carriage was 44mm. The change in total bandwidth led to a change in the winding patterns available, resulting in the need of finding a new pattern. Using CADWIND, a new pattern was found that proved even more effective than the original, according to the simulated graph shown in Figure 6.5. The chosen parameters are shown in Figure 8.2.

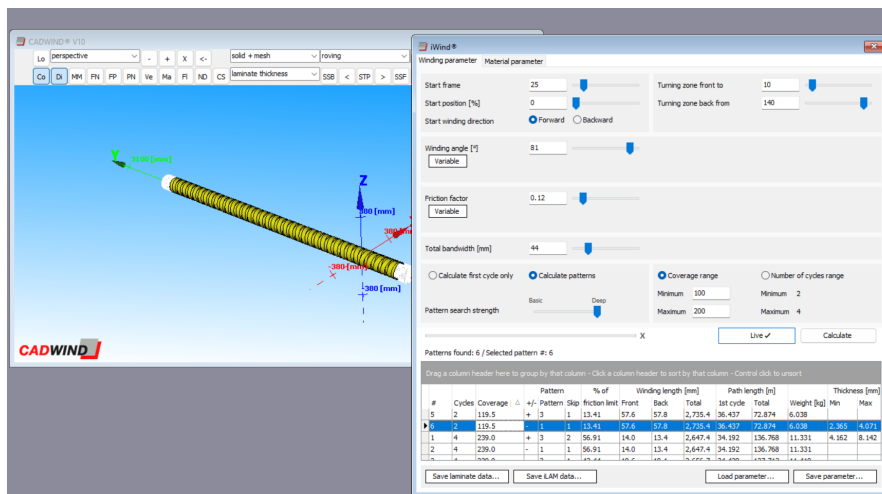


Figure 8.2: CADWIND parameters for 81 degrees

Winding

After preparing the mandrel, the next step is to transfer data from the winding program (CADWIND) to the machine's CNC control panel, Figure 8.3. Adjustments to certain operating conditions of the machine can be made at the control panel if necessary.



Figure 8.3: Control panel for winding machine

Due to imprecise manufacturing methods used to connect the adapters to the shafts, a slight uneven rotation was observed during production. This was attributed to slightly oversized holes in the winding adapters, causing the shafts, and consequently, the mandrel to rotate unevenly. However, the irregular rotation was deemed non-critical in cooperation with the supervisors at OPS Composite Solutions.

Dry Winding

Dry winding served to evaluate how well the selected winding pattern aligns with the mandrel. This method allows for adjustments to be made if the alignment falls short of expectations. If the pattern fails to align satisfactorily, the dry fibers can simply be removed and adjustments to the machine's input data can be made to achieve a better fit. The criteria for a satisfactory alignment include ensuring a constant fiber angle over a section covering the desired length specifications of the fuselage, providing lamination coverage that enables the extraction tool to function effectively - by extending the laminate almost to the very end of one side of the mandrel, and achieving a laminate thickness of approximately 2.5mm in the zone that adheres to the fuselage. However, it's important to note that the thickness of the dry wind may include minor differences from that of the wet wind.



Figure 8.4: Dry winding

Wet winding

After establishing a good alignment through dry winding, the next step is to apply the release wax and film before wet winding. The wax functions as a release agent, allowing the release film to slide off post-winding. Afterwards the mandrel's surface is covered with a layer of wet epoxy resin. This is essential for creating an even inner surface for the composite laminate. The fibers are then impregnated in the wet epoxy resin, before winding the fibers onto the mandrel using the same alignment and pattern deemed satisfactory during dry winding. Because the fibers are thoroughly coated in wet epoxy, maintaining constant rotation of the mandrel is crucial during both the winding process and overnight after winding. This ensures proper adhesion and prevents dripping, which could result in uneven distribution and shape of the composite laminate. After the composite laminate had dried sufficiently, the winding machine was stopped, and the mandrel with the composite laminate was removed from the machine.



Figure 8.5: Wet winding

Hardening

After the composite laminate had dried sufficiently, it was observed that the laminate had not achieved the required hardness necessary to maintain its form and shape upon extraction from the mandrel. Therefore, an initial heat treatment was deemed necessary before attempting extraction. This involved placing the mandrel in an industrial oven at 60 degrees Celsius for a duration of 3 hours as seen in Figure 8.6. The premise for not fully heat treating the composite before extraction was both due to time constraints and to preserve the ability to leverage heat expansion to aid in extraction, as higher temperature might be required if fully heat treated, potentially compromising the integrity of the film. Post-extraction, full heat treatment was conducted at UiS, at a temperature of 60 degrees Celsius for a duration of 8 hours.



Figure 8.6: Heat treatment Pre-extraction

Extraction

The extraction process proved to be challenging, despite the functionality of the extraction tool, as it successfully managed to move the laminate. The underlying issue stemmed from the significant friction and surface pressure between the mandrel and laminate, persisting after initial extraction. While the extraction tool was capable of moving the laminate, its limited range posed a problem. In response, a solution was sought that leveraged the same principle as the extraction tool, utilizing a hydraulic jack and a cylinder pipe to push and extract the laminate, as seen in Figure 8.7. The cylinder pipe used to extract the composite had a slightly larger inner diameter than the mandrel, yet remained within the range of the composite's diameter. This allowed it to effectively apply pressure onto the composite during the extraction process without risking adherence to the mandrel. The implementation of this method proved successful in effectively extracting the laminate from the mandrel.



Figure 8.7: Hydraulic jack extraction

Preparation

After the fuselage was brought back to UiS, the preparation for launch could begin. To fit the fuselage over the inner structure, the fuselage had to be sanded from the inside and cut to the correct length. This was all done in-house. Moreover, the decision was made to paint it black with stickers in white. To accomplish this, a layer of metallic black was applied to the fiberglass, necessitating some sanding to smooth out the bumpy exterior. The work was done by ProPaint, who is a sponsor for the project. Furthermore, white stickers were carefully affixed onto the black paint for added detail.

The assembled middle air-frame of Borealis II can be seen in the picture to the right, Figure 8.8. This was taken during the first integration test of the fuselage. This test was done multiple times to make the assembly as easy as possible. Sanding on the inside of the fuselage and turning down the aluminium parts at the top and bottom were done to ensure a snug fit.



Figure 8.8: Assembled middle fuselage before painting



Figure 8.9: Assembled middle fuselage after painting

The end result after painting, stickers and holes for the cameras is shown in the picture above, Figure 8.9.

Chapter 9

Results

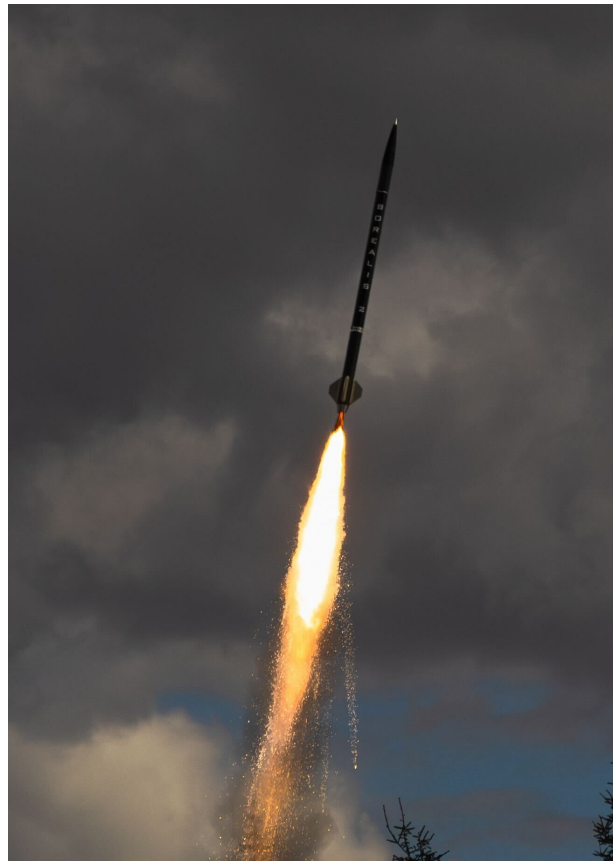


Figure 9.1: Stunning picture of the flight of Borealis II. Photo:

In this chapter the results of the thesis will be presented. The launch of the rocket Borealis II being the main focus.

Testing

Several preliminary tests were conducted this year, and all appeared promising. Although there were some issues with the avionics systems, the fuselage was completed two days before departure for the launch site, alleviating concerns in that regard. To address the avionics problems, the bachelor group responsible for them worked late nights to ensure readiness for launch. Despite encountering some issues upon arrival at Helleland, they were manageable enough to be resolved on-site.

One of the most important tests were a dress-rehearsal. A dress-rehearsal takes the team through the whole process of the launch and checks that all the procedures are correctly made and nothing is missing. The rehearsal took place right outside of UiS, and was the first time the rocket was placed in the new launch rail, created by a small team of engineers. Notably, aspects such as the full assembly of the launch rail and fuel loading, which is a one-time procedure, were not tested during this rehearsal. The dress rehearsal proceeded smoothly, with all necessary preparations completed satisfactorily. A photograph from this rehearsal is depicted in Figure 9.2.



Figure 9.2: Dress-rehearsal with Borealis II on the launch rail

Launch day

The launch was held at Helleland Spaceport, just like the launch of Borealis I, as mentioned in Section 1.2.1. The aviation authorities granted the launch permit in early March, setting the launch window from April 20th to May 5th. The decision for a two-week window primarily aimed to account for the unpredictable weather in Stavanger, where favorable conditions are crucial for rocket launches. This year, April 27th was chosen for the launch, strategically positioned midway through the window and aligning perfectly with optimal weather conditions and logistical considerations.

The countdown commenced at 12:00 local time, with a targeted launch time of 16:00, requiring every step to be completed within a four-hour timeframe. Impressively, the schedule was adhered to almost precisely, a testament to the thorough training and preparation made. Although certain procedures exceeded their estimated durations, time was compensated by efficiencies in other steps. Closing in on the launch time, the rocket was placed on the launch rail, with all systems indicating readiness. A picture of this can be seen in Figure 9.3.



Figure 9.3: Borealis II on the launch rail minutes before launch

Following a misfire and subsequent rewiring of the launching mechanism, Borealis soared into the skies, ascending to an altitude of approximately 2100 meters above sea level at a maximum velocity of 950 km/h, according to the data collected by the avionics system, Figure 9.5. The entire ascent of the rocket was meticulously captured from various angles and is available for viewing on UiS Aerospace's [YouTube](#) channel.

No data from the descent could be gathered due to the loss of telemetry following the deployment of the parachutes. Despite this telemetry loss, the chutes were deployed correctly, thanks to safety measures implemented by the recovery team. The chutes deployed correctly for the first time in UiS Aerospace history, deploying at apogee. Although the main chute, intended to deploy at approximately one kilometer above ground, accidentally deployed at apogee, UiS Aerospace still considers this a success. Figure 9.4, to the right, shows Borealis II after the chute deployment, indicating that the chutes were partially deployed.



Figure 9.4: Borealis II hanging from chutes

During the separation process, the aft air-frame was lost due to undersized screws securing the avionics system. Consequently, the rocket drifted longer than simulated, traveling approximately two kilometers before landing gently.

Ole Dokka, CEO of Spaceport Norway, emphasized that this was the first rocket to land safely on Norwegian soil, marking a remarkable achievement.

Results from launch

Following the rocket's recovery, the team gathered for a group photo with the rocket at the center, as shown in Figure 9.6. In the image, the effectiveness of the fuselage constructed in this thesis is evident, as it successfully maintained structural integrity and withstood both the dynamic pressure experienced during flight and the 18g forces encountered during parachute deployment, as illustrated in the data plot presented in Figure 9.5. Upon closer examination, no visible damage or permanent deformation was observed in the fiberglass.

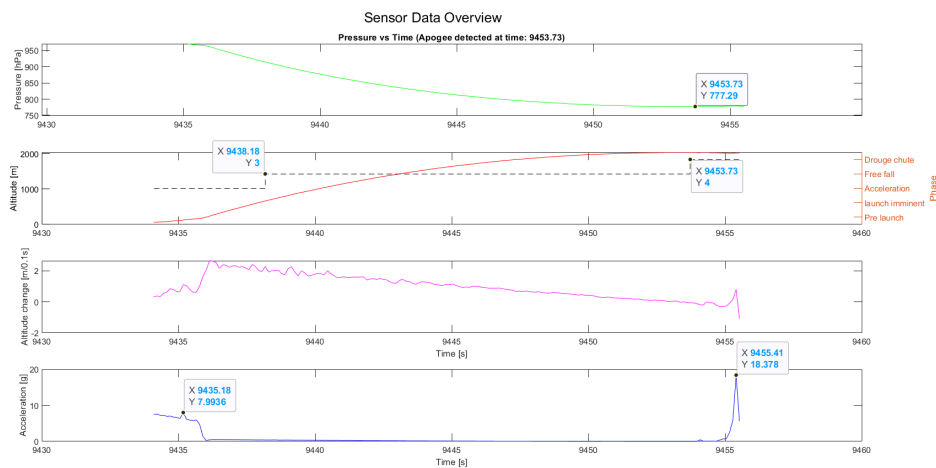


Figure 9.5: Data from the launch of Borealis II



Figure 9.6: Group photo with everyone involved with the launch

Dynamic Pressure from collected data

The dynamic pressure calculated from the flight data is depicted in the plot and prompt below: Figure 9.7 and 9.8, respectively. The plot clearly illustrates that the maximum pressure occurred during the ascent phase. Unfortunately, telemetry ceased around apogee, resulting in a lack of data for the remainder of the flight. However, based on predicted data in Figure 6.3, it's expected that dynamic pressure during descent was minimal due to parachute deployment, which slowed the velocity. Although there are spikes in the data, these anomalies do not affect the maximum dynamic pressure and are therefore disregarded. The prompt provides the maximum pressure experienced during the flight.

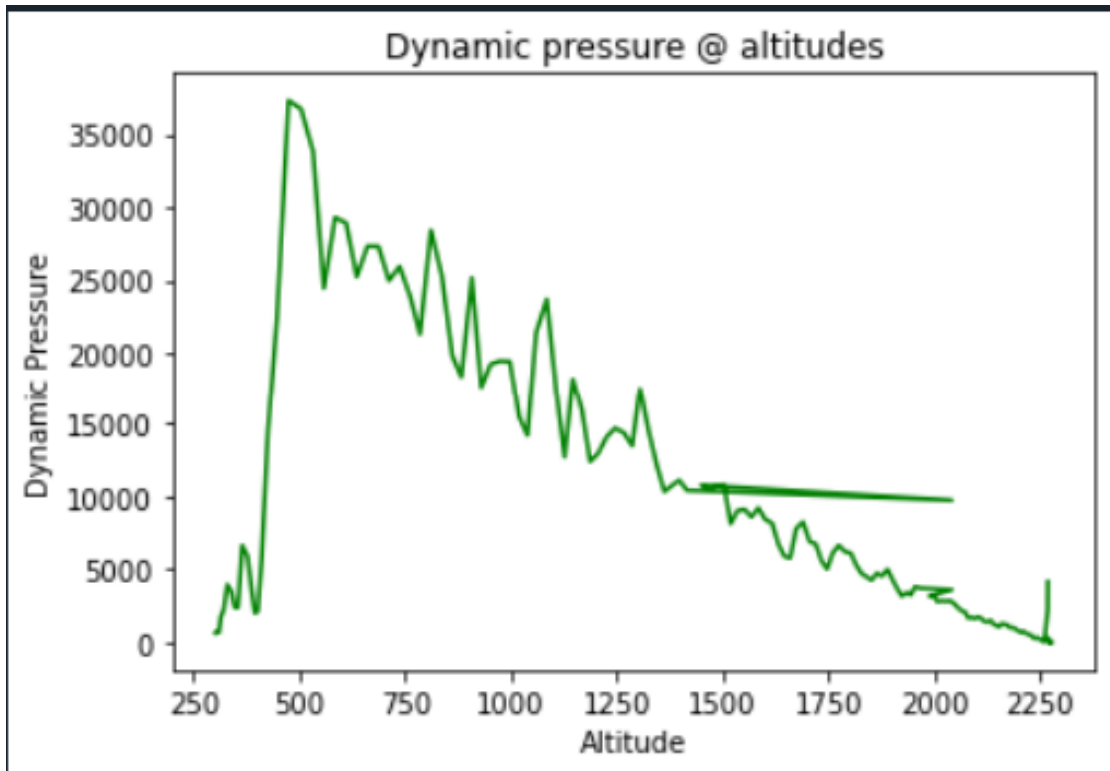


Figure 9.7: Plot produced using data collected during flight

```
Max Q is: 37327.34 Pa. Which is 36.84% of the static pressure
```

Figure 9.8: Max dynamic pressure using data collected

Chapter 10

Discussion and Conclusion



Figure 10.1: Borealis at the moment of ignition

In this chapter the production process and finalized product will be evaluated and discussed, to highlight problems and achievements regarding the thesis.

Production Process & Filament Winding

This section will cover the production process, including the manufacturing of the mandrel and its utilization along with the winding machine to create the glass fiber fuselage. The production process will mainly focus on time management and time constraints. Additionally, the benefits and problems arising from the design of the mandrel will be discussed in relation to the usage of the winding machine.

Production process

A tentative week for fuselage production was established in the initial stages of the mandrel production process, following a meeting with OPS Composite Solutions. The week was set for early March, due to production backlog at their facility. This resulted in a relatively short production process for the mandrel, leaving little time for design refinement and manufacturing. Consequently, minor flaws occurred that could have been avoided with more optimized design and precise manufacturing. The tentative production week, though, could not be upheld due to a loss of workforce at the firm. This resulted in a delayed production, causing the completion of the glass fiber to be just in time for launch, but with minimal spare time.

If the production timeline had been planned earlier there could have been less stress towards the end and the end product could have been better prepared. The initial production date being early made for a hectic production of the mandrel, while the delay of production caused hectic preparation of the glass fiber. The uncertainty in when the product was to be produced inflicted how the production process was executed, some parts of the mandrel needed more time to be optimized for production while at the same time the glass fiber was rapidly prepared for launch. In addition to this, the delayed laminate manufacturing also led to a rushed preparation of the fuselage before launch. ProPaint, one of the UiS Aerospace sponsors, did not have enough time to smooth out all the bumps, and the stickers did not arrive on time, resulting in additional work. A more reliable timeline would sufficiently improve the time management and make for a smoother process.

Filament Winding & Mandrel Use

Upon commencing the production of the fuselage the orientation of the adapters caused minor difficulties in mounting the mandrel to the winding machine. Specifically, the orientation and fastening method of the adapters posed unexpected challenges. If one of the adapters was rotated significantly more, compared to the other, it could have posed a difficult-to-fix problem. This issue stemmed from a lack of knowledge regarding the winding machine. Additionally, the fastening method between the adapters and shafts was sub-optimal resulting in a slight uneven rotation on the mandrel. This was, however, still deemed satisfactory in collaboration with the supervisors at OPS Composite Solutions.

The extraction process proved to be demanding with the extraction tool having limited ability. Coning of the mandrel was advised by OPS Composite Solutions early in the process, but could not be implemented due to the geometry of the rocket being purely cylindrical. Indeed, such an incline would contradict the product specifications set by UiS Aerospace. Utilization of a slight inclined shape would facilitate the extraction by significantly reducing the contact surface between the mandrel and the composite after initial extraction. Working around these issues resulted in the fuselage lacking a coned shape, allowing it to adhere to the specified geometry requirements.

The Fuselage

This section will discuss the results attained from analysis and calculations compared with the testing of the fuselage. The fuselage will mainly be evaluated on its geometry, structural integrity and practicality. From this, a conclusion can be drawn.

Geometry

The fuselage's dimensions were nearly exact, with the main discrepancy found in the outer diameter. The pattern chosen during production resulted in a glass fiber thickness of 2.365mm. However, after sanding and spray coating, the total outer diameter was measured to 154.8mm. Comparing this to the specified outer diameter of 155mm from UiS Aerospace, the difference in diameter was determined to be negligible for the performance of the final product. The remaining dimensions were methodically sanded down to meet the design parameters predetermined by UiS Aerospace.

Structural integrity

The analysis conducted in Ansys predicted minimal deformation and indicated almost no risk of failure. While nothing can be definitively concluded about deformation during flight, observing the fuselage completely intact and undeformed suggests that any deformation was well within the range for elastic deformation. Since the fuselage remained intact and returned to its undeformed shape, it can be deduced that it withstood the dynamic pressure with a reliable factor of safety.

Upon comparing the collected data with the estimated data on dynamic pressure, it's evident that there's a discrepancy of approximately 15 kPa. This indicates that the estimated Max Q was somewhat exaggerated, resulting in the fuselage being overdimensioned for its purpose. The discrepancy is likely attributed to the fuel being of a weaker grade than initially predicted, leading to the rocket reaching a height of 2100m instead of the projected 2700m. Consequently, the rocket also achieved a lower maximum velocity, resulting in a reduced Max Q.

Practicality

Considering the practical benefits of the fuselage, the greatest advantage lies in the material properties of glass fiber compared to carbon fiber. The ability to communicate with the electronics aboard the rocket without mounting antennas on the outside is a significant benefit, ensuring the safety of the antennas and the electronics. However, one major drawback is the time needed to disassemble the middle air-frame of the rocket to access the the main avionics unit. This could have a significant impact during the launch procedure, if Ground Control loses contact with the rocket before launch and needs to reset their systems, delaying the launch with up to an hour. Addressing this issue would make problem-solving on the day of launch faster and easier.

Chapter 11

Further Work

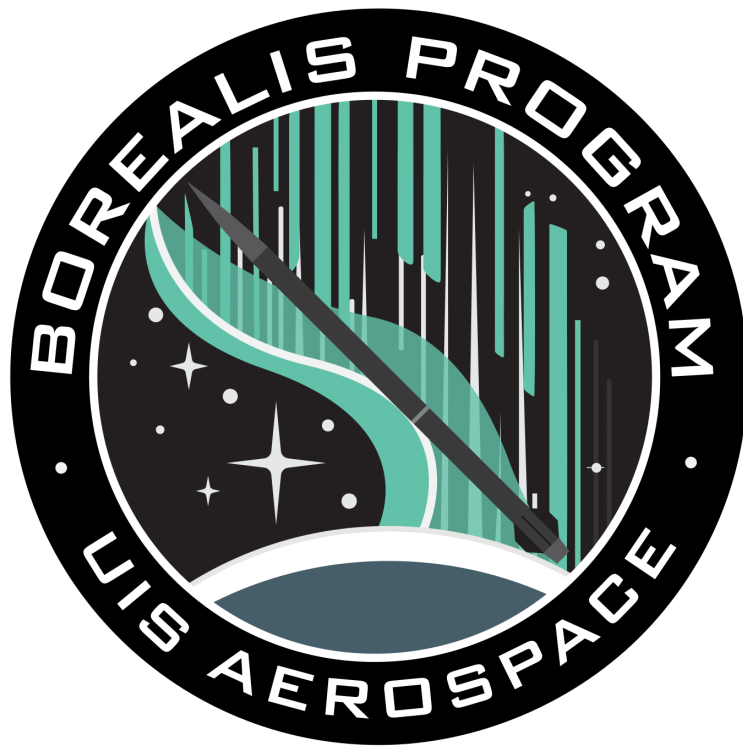


Figure 11.1: Borealis Program Mission Patch

This chapter will focus on what can be done to further develop the fuselage of Borealis. Both things considered during this project and wishes from UiS Aerospace will be mentioned.

Nose cone

UiS Aerospace intends to explore the possibility of manufacturing the nose cone from either carbon fiber or glass fiber in the future. Initially, this was intended to be part of this thesis, but was ultimately shelved early due to workload constraints. According to OPS Composite Solutions, producing a cone in glass fiber presents significant challenges. It was suggested that using the molding technique would better suit the shape of the cone and could potentially offer a simpler implementation compared to winding. However, the specific approach for this task will be entirely at the discretion of the team that eventually decides to do it.

Below is the first version of how the nosecone mandrel would have looked, Figure 11.2. This takes into consideration about the end-winding, slippage and aerodynamics focused around the subsonic velocity regime and transitional phase between subsonic and transonic velocities. These factors call for thorough consideration by future teams.

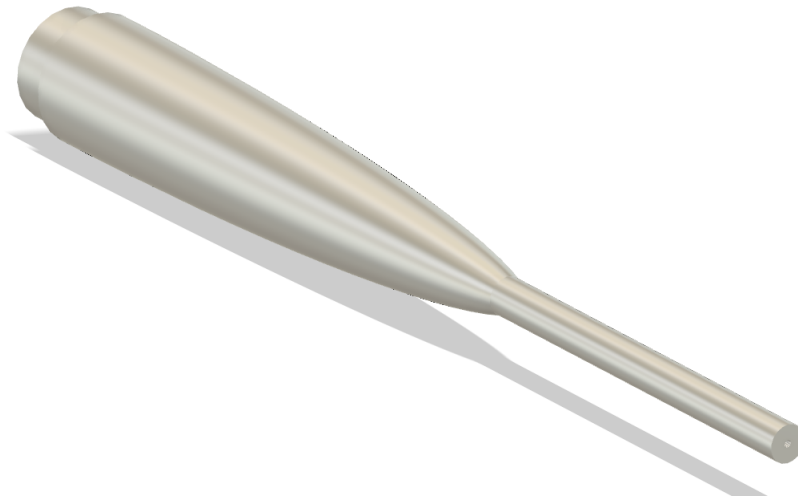


Figure 11.2: 3D model of the nosecone on the mandrel

Multiple layers/fiber angles

This thesis primarily focuses on Max Q, emphasizing the importance of maintaining structural integrity during this critical phase of aerodynamic stress. The decision to solely calculate for Max Q stemmed from both limited experience and constraints imposed by the specifications of the glassfiber material used. With a thickness rating of one millimeter, the fuselage design could accommodate no more than two layers of fiber, thereby restricting the number of possible fiber angles. Typically, laminates incorporate multiple angles to distribute forces efficiently, optimizing the strength of the fibers. As a consequence of these limitations, the fuselage design prioritizes structural integrity during Max Q, but may not adequately address crash scenarios.

Introducing a different fiber with a smaller thickness could simultaneously address the Max Q phase, crash events, and other scenarios. This adjustment will not substantially increase the workload, and the fuselage's weight should remain relatively unchanged. This would also utilize the full potential of the filament winding method.

Panels in the fuselage

The request for panels in the fuselage originated from the avionics department early in the project. They sought improved accessibility to facilitate easier resets of the electronics system once the fuselage was fully assembled. This need arose from the experience with Borealis I, where communication was lost between ground control and the rocket while it was mounted onto the launch rail. Although the mechanical team began examining the impact of the panels, they were unable to complete the assessment due to other pressing issues. The preliminary design of the panels are shown in the Figure 11.3 below. The matter was then shelved before commencing the thesis work.

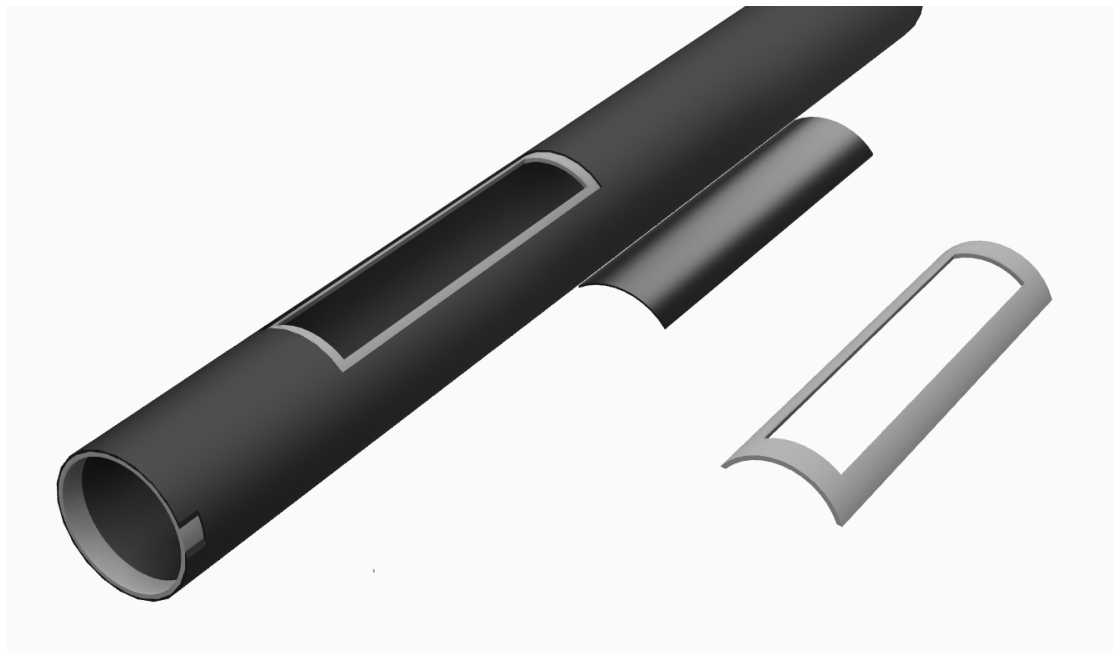


Figure 11.3: Preliminary design of the panels solution

The issue, however, resurfaced some two weeks prior to the launch. This time, the request was escalated, calling for two sizable panels. One panel was designated for the MAVION, while the second was intended for the rideshare program, which included three groups with a 1U CubeSat each. Consequently, the panels were expected to be around 400mm in length each, totaling approximately 50% of the fuselage's length. Due to time constraints, there was no opportunity to verify how integration of panels could impact the anisotropic properties of the glass-fiber fuselage. As it could potentially compromise the integrity of the glass fiber material, rendering it unfit for launch. It was therefore determined that there would be no such panels for Borealis II. However, smaller incisions were made, sized adequately to accommodate a camera lens for recording from the rockets perspective. It was determined that these modifications would not compromise the fuselage's integrity, ensuring that it remains suitable for launch.

Bibliography

- [1] Dimitrios G. Pavlou. *Composite Materials in Piping Applications*. DEStech Publications, 2013.
- [2] William D. Callister Jr. and David G. Rethwisch. *Materials Science and Engineering*. John Wiley & Sons, 9th edition, 2011.
- [3] N.K. Chhapakhane P.V. Vunjavate and S.B. Kumbhar. Experimental determination of critical buckling load for glass composite laminate. *International Journal of Advanced Engineering Research and Studies*, 1:106–108, 2012.
- [4] J.N. Reddy. *Theory and Analysis of Elastic Plates and Shells*. CRC Press, 2007.
- [5] Raphael T. Haftka Albert A. Groenwold. Optimization with non-homogeneous failure criteria like tsai–wu for composite laminates. *Struct Multidisc Optim*, 32:183–190, 2006.
- [6] Yunus A Çengel. *Fundamentals of thermal-fluid sciences*. McGraw-Hill Education, 2017.
- [7] NASA and U.S Air Force. *U.S Standard Atmosphere*. U.S. Government Printing Office, 1976.
- [8] ISO 286-1:2010 - Geometrical product specifications (GPS) — ISO code system for tolerances on linear sizes — part 1: Basis of tolerances, deviations and fits. International Organization for Standardization, 2010. ISO Standard.
- [9] ISO 286-2:2010 - Geometrical product specifications (GPS) — ISO code system for tolerances on linear sizes — part 2: Tables of standard tolerance classes and limit deviations for holes and shafts. International Organization for Standardization, 2010. ISO Standard.
- [10] Hirpa G.Lemu. *Dimensjonering av Maskinelementer, kompendium i fag MSK 210 Maskin konstruksjon*. University of Stavanger, 2020.
- [11] EHA Composite Machinery GmbH. *User manual - Fiber winding machine (FWA V / 5 / 1)*, 2012.
- [12] Geoffrey Allen and John C. Bevington. *Comprehensive Polymer Science and Supplements*. Elsevier, 1996.
- [13] Sotiris KOUSSIOS. *Filament Winding: a Unified Approach*. PhD thesis, Delft university of technology, 2004.
- [14] Stan T. Peters. *Composite Filament Winding*. ASM International, 2011.
- [15] Richard G.Budynas and J.Keith Nisbett. *Shigley’s Mechanical Engineering Design, 11th Edition, Si Units*. McGraw-Hill Education, 2021.

- [16] L.Kolarik, K.Kovanda, M. Valova, P. Vondrous, and J.Dunovsky. Weldability test of precipitation hardenable aluminium alloy EN AW 6082 T6. *MM Science Journal*, 2011.
- [17] William D.Callister jr and David G.Rethwisch. *Materials Science and Engineering: An Introduction, 10th Edition*. Wiley, 2018.

Appendix A

Tables

Table A.1: Glassfiber Material Properties

Specification	Name/Type	Producer	
OPS Material Designation	FW-SE3030-AMPREG31	OPS	
Fiber	SE3030	3B	
Resin	Ampreg 31	Gurit	
Hardener	3X Extra-slow	Gurit	
Production Method	Filament Winding	OPS	
Curing Schedule	12h, 60C	OPS	
General	Property	Value	Unit
Fiber orientation, x=0deg	θ_i	0	deg
Density of laminate	ρ	1,88	kg·dm-3
Fiber Volume Fraction	v_f	50	%
Fiber Weight Fraction	w_f	70	%
Ply Thickness	h	1,0	mm
Orthotropic Elasticity	Property	Value	Unit
Tensile modulus, fiber direction	E_x	41,05	GPa
Tensile modulus, traverse direction	E_y	6,43	GPa
Tensile modulus, normal to plane	E_z	6,43	GPa
Poisson's Ratio, XY plane	ν_{xy}	0,325	ul
Poisson's Ratio, YZ plane	ν_{yz}	0,325	ul
Poisson's Ratio, XZ plane	ν_{xz}	0,325	ul
Shear Modulus, XY plane	G_{xy}	2,38	GPa
Shear Modulus, YZ plane	G_{yz}	2,38	GPa
Shear Modulus, XZ plane	G_{xz}	2,38	GPa
Orthotropic Strain Limits	Property	Value	Unit
Tensile X Direction, Mean	ϵ_{xt}	0,0235	ul
Tensile X Direction, Std.		0,0014	ul
Tensile X Direction, COV		60,869	%
Tensile X Direction, km factor		2,1	ul
Tensile X Direction, Charact. Value		0,0205	ul
Tensile Y Direction, Charact. Value	$\hat{\epsilon}_{yt}$	0,0031	ul
Tensile Z Direction, Charact. Value	$\hat{\epsilon}_{zt}$	0,0009	ul
Compressive X Direction, Charact. Value	$\hat{\epsilon}_{xc}$	0,0140	ul
Compressive Y Direction, Charact. Value	$\hat{\epsilon}_{yc}$	0,0041	ul
Compressive Z Direction, Charact. Value	$\hat{\epsilon}_{zc}$	0,0039	ul
Shear XY, Charact. Value, Linear Limit	$\hat{\epsilon}_{xy}$	0,0049	ul
Shear XY, Charact. Value, Failure		0,0170	ul
Shear YZ, Charact. Value	$\hat{\epsilon}_{yz}$	0,0031	ul
Shear XZ, Charact. Value	$\hat{\epsilon}_{xz}$	0,0031	ul

Table A.2: Glassfiber Material Properties (Continued)

Orthotropic Stress Limits	Property	Value	Unit
Tensile X Direction, Mean	$\hat{\sigma}_x^t$	963,70	Mpa
Tensile X Direction, Std.		59,94	Mpa
Tensile X Direction, COV		62,197	%
Tensile X Direction, km factor		2,1	ul
Tensile X Direction, Charact. Value		837,83	Mpa
Tensile Y Direction, Charact. Value	$\hat{\sigma}_y^t$	19,93	Mpa
Tensile Z Direction, Charact. Value	$\hat{\sigma}_z^t$	5,79	Mpa
Compressive X Direction, Charact. Value	$\hat{\sigma}_x^c$	574,70	Mpa
Compressive Y Direction, Charact. Value	$\hat{\sigma}_y^c$	26,36	Mpa
Compressive Z Direction, Charact. Value	$\hat{\sigma}_z^c$	25,08	Mpa
Shear XY, Charact. Value, Linear Limit	$\hat{\tau}_{xy}$	11,66	Mpa
Shear XY, Charact. Value, Failure		40,46	Mpa
Shear YZ, Charact. Value	$\hat{\tau}_{yz}$	7,38	Mpa
Shear XZ, Charact. Value	$\hat{\tau}_{xz}$	7,38	Mpa

The orientations described in the table above are as follows: X represents the fiber direction, previously labeled as 1; Y indicates the direction perpendicular to the fibers, earlier denoted as 2; and Z signifies the direction normal to the plane, previously labeled as 3.

Table A.3: Aluminium properties table

Properties aluminium	Value
Modulus of elasticity E	69GPa [17]
Density	2.7g/cm ³ [17]
Weld properties EN AW-6082 T6	Value
Weld assured yield strength S_y	240MPa [16]
Weld assured tensile strength S_{ut}	295MPa [16]
Weld failure criteria	limit
For weld yield strength	0.4 S_y [15]
For weld ultimate tensile strength	0.3 S_{ut} [15]

Appendix B

Python Code

```
1 import matplotlib.pyplot as plt
2 import itertools
3
4 # Make lists
5 altitude = []
6 velocity = []
7
8 # Open file, split lines and add data to each list
9 with open("OpenRocket_simulation.csv", "r") as r:
10     for line in r:
11         if line[0] == "#":
12             continue
13         else:
14             parameters = line.split(",")
15             altitude.append(float(parameters[1]))
16             velocity.append(float(parameters[2]))
17
18
19 # Setting up list for dynamics pressure = 1/2 * density * velocity ^2
20 dynamic_pressure = []
21 density = []
22
23 r = 287.05 # J/kg-K
24 t = 10 + 273.15 # Assume 10 degrees Celsius
25
26 for z in altitude:
27     p = 101325 * (1 - z * 0.0000225577)**5.2559
28     density.append(p / (r*t))
29
30 for (v,d) in zip(velocity, density):
31     q = (1/2) * d * (v**2)
32     dynamic_pressure.append(q)
33
34 print(f'Max Q is: {max(dynamic_pressure) / 1000:.3f} Kpa')
```

Figure B.1: Open Rocket dynamic pressure Calculation

```
1
2 import numpy as np
3 import math as m
4
5 p = 51496.46
6 dia = 0.15
7 NP = 2
8
9 E_1 = 41.05*(10**9)
10 E_2 = 6.43*(10**9)
11 v_12 = 0.325
12 G_12 = 2.38*(10**9)
13
14 sigma_1_T = 963.7*(10**6)
15 sigma_1_C = 574.7*(10**6)
16 sigma_2_T = 19.93*(10**6)
17 sigma_2_C = 26.36*(10**6)
18 tou_12_F = 40.46*(10**6)
19
20 F_1 = (1 / sigma_1_T) + (1/ sigma_1_C)
21 F_2 = (1 / sigma_2_T) + (1/ sigma_2_C)
22 F_66 = (1 / tou_12_F) **2
23 F_11 = - 1 / (sigma_1_T * sigma_1_C)
24 F_22 = - 1 / (sigma_2_T * sigma_2_C)
25
26
27 z = []
28
29 #Creates a list of length, z, for each layer, from the top.
30 for i in range(0,3):
31     z.append(i*10**-3)
32
33 h = 2.5*10**(-3)
34
35
36 N_y = 1/2 * p * dia #Force from external pressure on a pressure vessel
37
38 angle = np.linspace(0,(np.pi / 2) , 10000)
39 tsai_wu1 = []
40 tsai_wu2 = []
41 failure = []
42
43 S11 = 1 / E_1
44 S12 = - (v_12 / E_2)
45 S22 = 1 /E_2
46 S66 = 1 / G_12
47
48 Q11 = S22 / ((S11 * S22) - (S12 * S12))
```

```

49 Q12 = - S12 / ((S11 * S22) - (S12 * S12))
50 Q22 = S11 / ((S11 * S22) - (S12 * S12))
51 Q66 = 1 / S66
52
53 def Local_Stresses(phi):
54     x = [phi, -phi]
55
56     A11 = 0; A12 = 0; A16 = 0; A22 = 0; A26 = 0; A66 = 0
57     B11 = 0; B12 = 0; B16 = 0; B22 = 0; B26 = 0; B66 = 0
58     D11 = 0; D12 = 0; D16 = 0; D22 = 0; D26 = 0; D66 = 0
59
60     for k in range(NP):
61         QQ11 = Q11 * (m.cos(x[k])**4) + 2 * ((Q12 + 2 * Q66) * (
62             m.sin(x[k])**2) * (m.cos(x[k])**2)) + Q22 * m.sin(x[k])**4
63         QQ12 = (Q11 + Q22 - 4*Q66)*(m.sin(x[k])**2) * (
64             m.cos(x[k])**2) + Q12*(m.sin(x[k])**4 + m.cos(x[k])**4)
65         QQ16 = (Q11 - Q12 - 2*Q66)*(m.sin(x[k]))*(m.cos(x[k])**3) + (
66             Q12 - Q22 + 2*Q66)*(m.sin(x[k])**3)*(m.cos(x[k]))
67         QQ22 = Q11*(m.sin(x[k])**4) + 2*(Q12 + 2*Q66)*(m.sin(x[k])**2)*(
68             m.cos(x[k])**2) + Q22*(m.cos(x[k])**4)
69         QQ26 = (Q11 - Q12 - 2*Q66)*(m.sin(x[k])**3)*m.cos(x[k]) + (
70             Q12 - Q22 + 2*Q66)*m.sin(x[k])*(m.cos(x[k])**3)
71         QQ66 = (Q11 + Q22 - 2 * Q12 - 2 * Q66)*(m.sin(x[0])**2)*(
72             m.cos(x[k])**2) + Q66 * ((m.sin(x[k])**4) + m.cos(x[k])**4)
73
74         A11 += QQ11 * (z[k+1] - z[k])
75         A12 += QQ12 * (z[k+1] - z[k])
76         A16 += QQ16 * (z[k+1] - z[k])
77         A22 += QQ22 * (z[k+1] - z[k])
78         A26 += QQ26 * (z[k+1] - z[k])
79         A66 += QQ66 * (z[k+1] - z[k])
80
81         B11 += (1/2) * QQ11 * (z[k+1]**2 - z[k]**2)
82         B12 += (1/2) * QQ12 * (z[k+1]**2 - z[k]**2)
83         B16 += (1/2) * QQ16 * (z[k+1]**2 - z[k]**2)
84         B22 += (1/2) * QQ22 * (z[k+1]**2 - z[k]**2)
85         B26 += (1/2) * QQ26 * (z[k+1]**2 - z[k]**2)
86         B66 += (1/2) * QQ66 * (z[k+1]**2 - z[k]**2)
87
88         D11 += (1/3) * QQ11 * (z[k+1]**3 - z[k]**3)
89         D12 += (1/3) * QQ12 * (z[k+1]**3 - z[k]**3)
90         D16 += (1/3) * QQ16 * (z[k+1]**3 - z[k]**3)
91         D22 += (1/3) * QQ22 * (z[k+1]**3 - z[k]**3)
92         D26 += (1/3) * QQ26 * (z[k+1]**3 - z[k]**3)
93         D66 += (1/3) * QQ66 * (z[k+1]**3 - z[k]**3)
94
95
96     ABD = np.array([[A11, A12, A16, B11, B12, B16],
97                    [A12, A22, A26, B12, B22, B26],

```

```

98         [A16, A26, A66, B16, B26, B66],
99         [B11, B12, B16, D11, D12, D16],
100        [B12, B22, B26, D12, D22, D26],
101        [B16, B26, B66, D16, D26, D66]])
102
103    abd = np.linalg.inv(ABD)
104
105    epsilon_x0 = abd[0,1] * N_y
106    epsilon_y0 = abd[1,1] * N_y
107    gamma_xy0 = abd[2,1] * N_y
108    k_x0 = abd[3,1] * N_y
109    k_y0 = abd[4,1] * N_y
110    k_xy0 = abd[5,1] * N_y
111
112    epsilon_x = epsilon_x0 + (h/2) * k_x0
113    epsilon_y = epsilon_y0 + (h/2) * k_y0
114    gamma_xy = gamma_xy0 + (h/2) * k_xy0
115
116    QQ = np.array([[QQ11, QQ12, QQ16],
117                  [QQ12, QQ22, QQ26],
118                  [QQ16, QQ26, QQ66]])
119
120    [sigma_x, sigma_y, tou_xy] = np.matmul(QQ,
121                                          [epsilon_x, epsilon_y, gamma_xy])
122
123    T = np.array([[m.cos(phi)**2, m.sin(phi)**2, 2* m.cos(phi) * m.sin(phi)],
124                 [m.sin(phi)**2, m.cos(phi)**2, -2 * m.cos(phi) * m.sin(phi)],
125                 [-m.cos(phi) * m.sin(phi), m.cos(phi) * m.sin(phi),
126                 m.cos(phi)**2 - m.sin(phi)**2]])
127
128    [sigma_1, sigma_2, tou_12] = np.matmul(T, [sigma_x, sigma_y, tou_xy])
129
130
131
132
133
134    return [sigma_1, sigma_2, tou_12]
135
136    def Tsai_wu(stress):
137        return (F_1 * stress[0]) + (F_2 * stress[1]) + (F_11 * (stress[0]**2)) + (
138            F_22 * (stress[1]**2)) + (F_66 * (stress[2]**2)) - (
139            m.sqrt(F_11 * F_22) * stress[0] * stress[1])
140
141    def Quad_safe(stress):
142        a = (F_11 * (stress[0]**2)) + (F_22 * (stress[1]**2)) + (
143            F_66 * (stress[2]**2)) - (m.sqrt(F_11 * F_22) * stress[0] * stress[1])
144        b = (F_1 * stress[0]) + (F_2 * stress[1])
145        d = (b**2) + (4*a)
146        sol1 = (-b-m.sqrt(d))/(2*a)

```

```
147     sol2 = (-b+m.sqrt(d))/(2*a)
148     return [sol1, sol2]
149
150
151 for phi in angle:
152     failure.append(Quad_safe(Local_Stresses(phi)))
153     tsai_wu2.append(Tsai_wu(Local_Stresses(phi)))
154
155 for solution in failure:
156     if min(solution) <= 0:
157         tsai_wu1.append(max(solution))
158     else:
159         tsai_wu1.append(min(solution))
```

Figure B.2: Optimal Angle Code

```
1 from Angle_Optimization import tsai_wu1, tsai_wu2, angle
2 from scipy.interpolate import CubicSpline
3 import numpy as np
4 import matplotlib.pyplot as plt
5
6
7 f = CubicSpline(angle* (180 / np.pi), tsai_wu1, bc_type='clamped')
8 g = CubicSpline(angle* (180 / np.pi), tsai_wu2, bc_type='clamped')
9 x_new = angle * (180 / np.pi)
10 y_new1 = f(x_new)
11 y_new2 = g(x_new)
12
13
14 for i in range(len(x_new)):
15     if y_new2[i] == min(y_new2):
16         x_min2 = x_new[i]
17
18 for i in range(len(x_new)):
19     if y_new1[i] == max(y_new1):
20         x_max1 = x_new[i]
21
22
23 #Plot 1: Safety Factor
24 plt.subplot(1, 2, 1)
25 plt.plot(x_new, y_new1, 'b')
26 plt.xlabel('Fiber Angle')
27 plt.ylabel('Safety Factor')
28
29 plt.plot(x_max1, max(y_new1), 'go')
30
31 #Plot 2: Tsai-Wu
32 plt.subplot(1, 2, 2)
33 plt.plot(x_new, y_new2, 'b')
34 plt.xlabel('Fiber Angle')
35 plt.ylabel('Tsai-Wu')
36
37 plt.plot(x_min2, min(y_new2), 'go')
38
39 plt.suptitle("Optimal Angle by Safety Factor and Tsai-Wu")
40 plt.tight_layout(pad=2.0)
41 plt.show()
42
43 print(f"The optimal angle is {x_max1:.8f} degrees")
44 print(f""""The safety factor here is {max(y_new1):.8f} with
45     a Tsai-Wu of {min(y_new2):.8f}""")
```

Figure B.3: Optimal Angle Plot Code

Appendix C

Technical Drawings

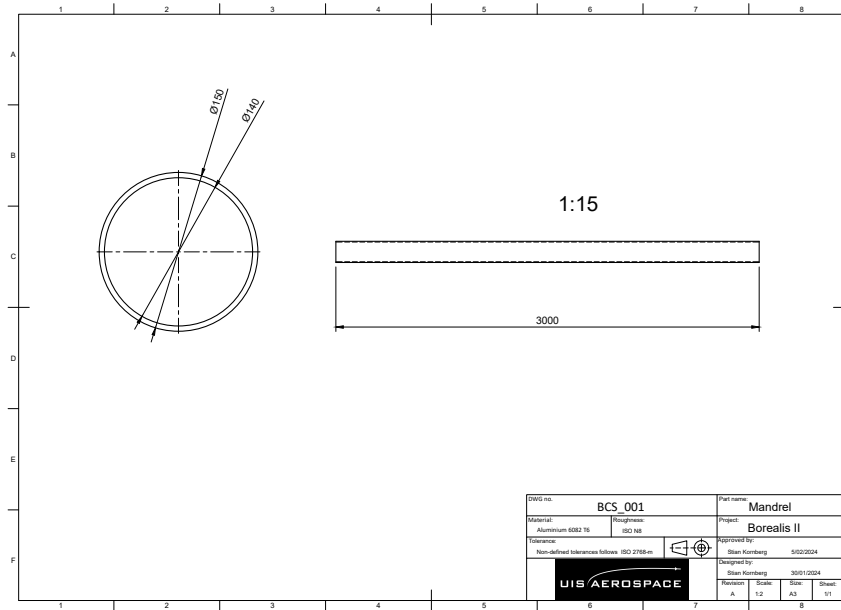


Figure C.1: Mandrel Tube Drawing

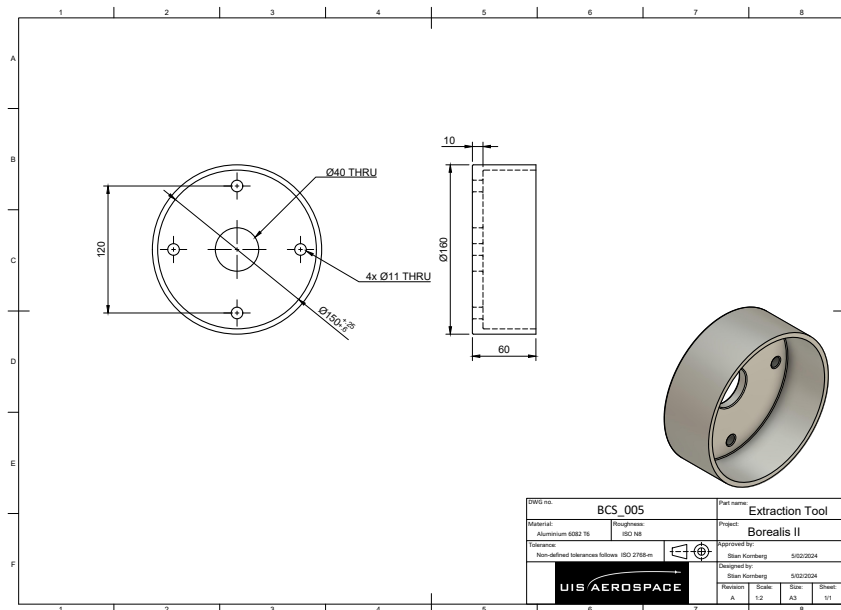


Figure C.2: Extraction Tool Drawing

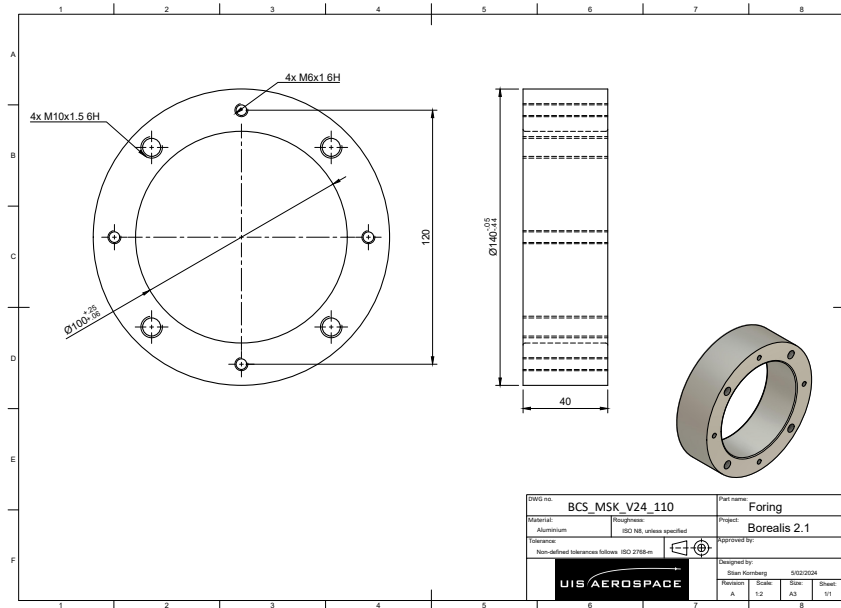


Figure C.3: Reduction Liner Drawing

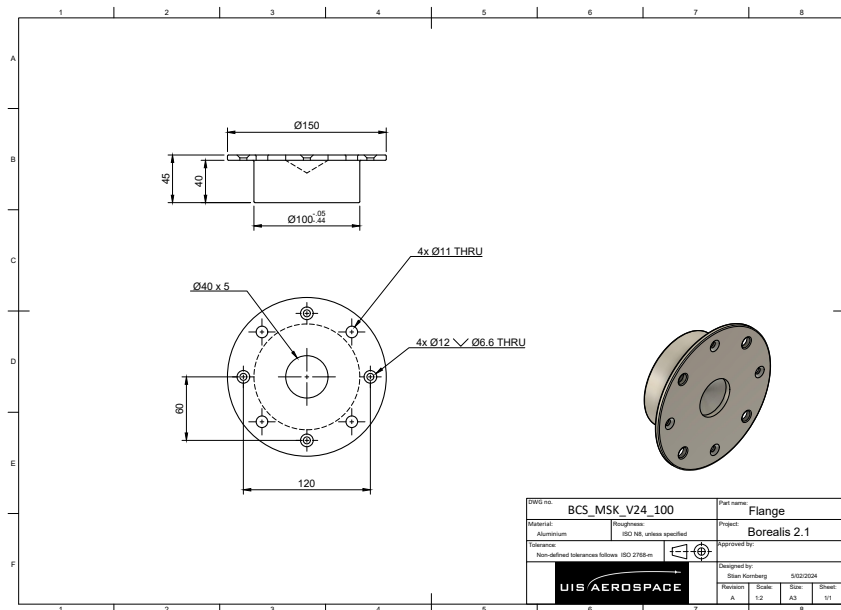


Figure C.4: Flange Drawing

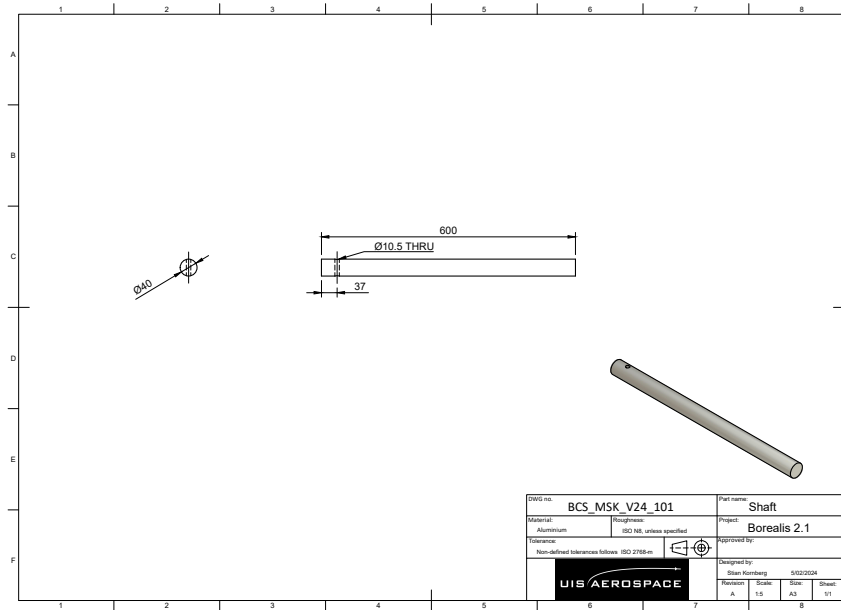


Figure C.5: Shaft Drawing

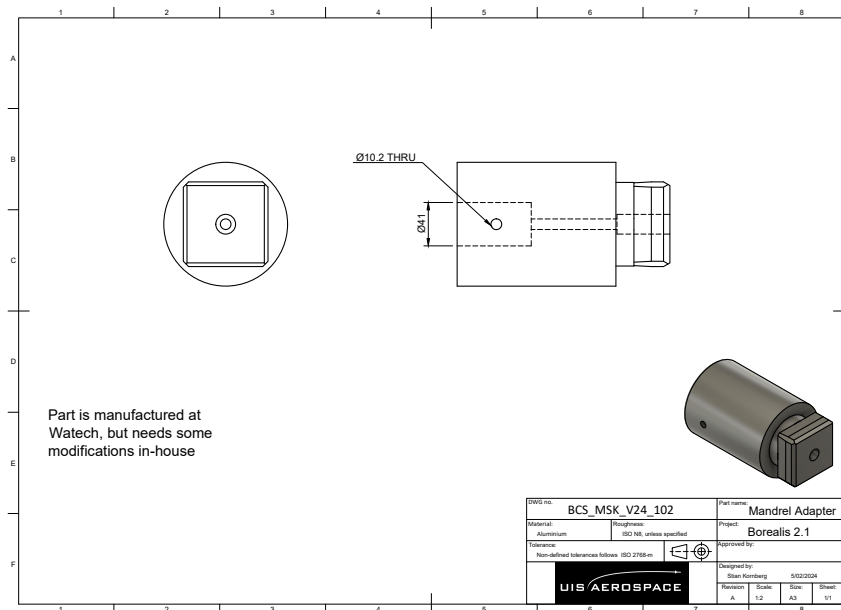


Figure C.6: Winding Adapter Drawing

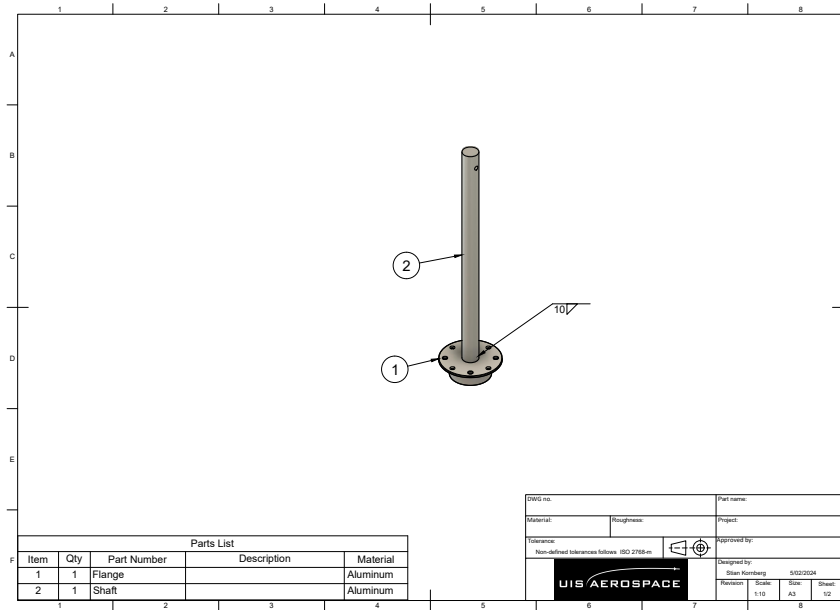


Figure C.7: Flange Assembly Drawing

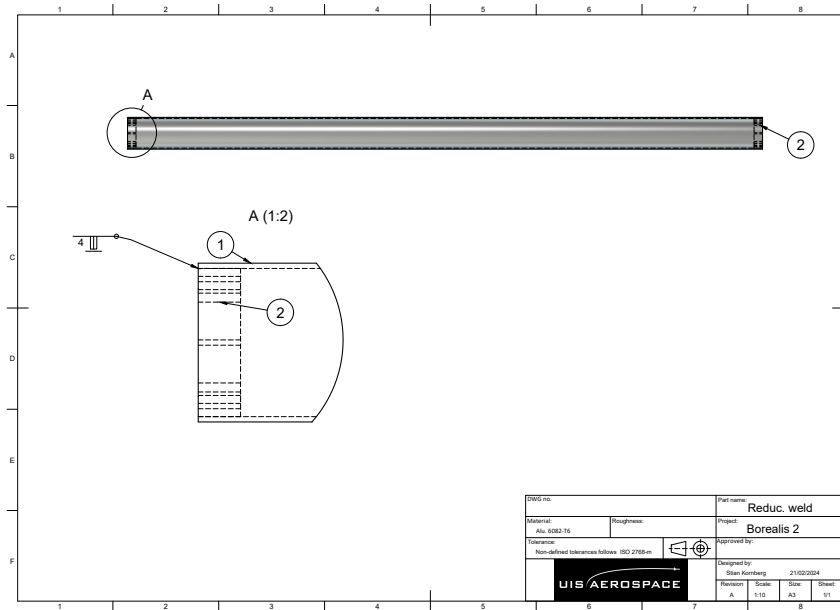


Figure C.8: Mandrel Assembly Drawing

Appendix D

Equations

Engineering Constants

The following engineering constants [1] are defined as

$$S_{11} = \frac{1}{E_1} \quad (\text{D.1})$$

$$S_{12} = -\frac{\nu_{21}}{E_2} \quad (\text{D.2})$$

$$S_{13} = -\frac{\nu_{31}}{E_3} \quad (\text{D.3})$$

$$S_{21} = -\frac{\nu_{12}}{E_1} \quad (\text{D.4})$$

$$S_{22} = \frac{1}{E_2} \quad (\text{D.5})$$

$$S_{23} = -\frac{\nu_{32}}{E_3} \quad (\text{D.6})$$

$$S_{31} = -\frac{\nu_{13}}{E_1} \quad (\text{D.7})$$

$$S_{32} = -\frac{\nu_{23}}{E_2} \quad (\text{D.8})$$

$$S_{33} = \frac{1}{E_3} \quad (\text{D.9})$$

$$S_{44} = \frac{1}{G_{23}} \quad (\text{D.10})$$

$$S_{55} = \frac{1}{G_{13}} \quad (\text{D.11})$$

$$S_{66} = \frac{1}{G_{12}} \quad (\text{D.12})$$

Material constants

The material constants [1] C_{ij} of the stiffness matrix [C] can be obtained:

$$C_{11} = \frac{S_{22}S_{33} - S_{23}^2}{S} \quad (\text{D.13})$$

$$C_{12} = \frac{S_{13}S_{23} - S_{12}S_{33}}{S} \quad (\text{D.14})$$

$$C_{13} = \frac{S_{12}S_{23} - S_{13}S_{22}}{S} \quad (\text{D.15})$$

$$C_{21} = C_{12} \quad (\text{D.16})$$

$$C_{22} = \frac{S_{33}S_{11} - S_{13}^2}{S} \quad (\text{D.17})$$

$$C_{23} = \frac{S_{12}S_{13} - S_{23}S_{11}}{S} \quad (\text{D.18})$$

$$C_{31} = C_{13} \quad (D.19)$$

$$C_{32} = C_{23} \quad (D.20)$$

$$C_{33} = \frac{S_{11}S_{22} - S_{12}^2}{S} \quad (D.21)$$

$$C_{44} = \frac{1}{S_{44}} \quad (D.22)$$

$$C_{55} = \frac{1}{S_{55}} \quad (D.23)$$

$$C_{66} = \frac{1}{S_{66}} \quad (D.24)$$

where

$$S = S_{11}S_{22}S_{33} - S_{11}S_{23}^2 - S_{22}S_{13}^2 - S_{33}S_{12}^2 + 2S_{12}S_{23}S_{13} \quad (D.25)$$

The members, Q_{ij} , are called reduced stiffnesses, given by the following equations [1]:

$$Q_{11} = C_{11} - \frac{C_{13}^2}{C_{33}} \quad (D.26)$$

$$Q_{12} = C_{12} - \frac{C_{13}C_{23}}{C_{33}} \quad (D.27)$$

$$Q_{22} = C_{22} - \frac{C_{23}^2}{C_{33}} \quad (D.28)$$

$$Q_{66} = C_{66} \quad (D.29)$$

Strain Transformation

combining the equations 3.5, 3.16, and 3.18 gives the transformed reduced compliance matrix [1]:

$$\begin{Bmatrix} \epsilon_x \\ \epsilon_y \\ \gamma_{xy} \end{Bmatrix} = \begin{bmatrix} \bar{S}_{11} & \bar{S}_{12} & \bar{S}_{16} \\ \bar{S}_{12} & \bar{S}_{22} & \bar{S}_{26} \\ \bar{S}_{16} & \bar{S}_{26} & \bar{S}_{66} \end{bmatrix} \begin{Bmatrix} \sigma_x \\ \sigma_y \\ \tau_{xy} \end{Bmatrix} \quad (D.30)$$

Where

$$\bar{S}_{11} = S_{11}m^4 + (2S_{12} + S_{66})n^2m^2 + S_{22}n^4 \quad (D.31)$$

$$\bar{S}_{12} = (S_{11} + S_{22} - S_{66})n^2m^2 + S_{12}(n^4m^4) \quad (D.32)$$

$$\bar{S}_{16} = (2S_{11} - 2S_{12} - S_{66})nm^3 - (2S_{22} - 2S_{12} - S_{66})n^3m \quad (D.33)$$

$$\bar{S}_{22} = S_{11}n^4 + (2S_{12} + S_{66})n^2m^2 + S_{22}m^4 \quad (D.34)$$

$$\bar{S}_{26} = (2S_{11} - 2S_{12} - S_{66})n^3m - (2S_{22} - 2S_{12} - S_{66})nm^3 \quad (D.35)$$

$$\bar{S}_{66} = 2(2S_{11} + 2S_{22} - 4S_{12} - S_{66})n^2m^2 + S_{66}(n^4 + m^4) \quad (D.36)$$

using notations $m = \cos \theta$ and $n = \sin \theta$ the parameters \bar{S}_{ij} are called transformed reduced compliances [1].

Inverse Transformation Matrix

The inversed transformation matrix $[T]^{-1}$ can be used to define σ_x , σ_y , and τ_{xy} [1]:

$$\begin{Bmatrix} \sigma_x \\ \sigma_y \\ \tau_{xy} \end{Bmatrix} = [T]^{-1} \begin{Bmatrix} \sigma_1 \\ \sigma_2 \\ \tau_{12} \end{Bmatrix} \quad (\text{D.37})$$

where the inversed transformation matrix $[T]^{-1}$ is given by [1]:

$$[T]^{-1} = \begin{bmatrix} \cos^2\theta & \sin^2\theta & -2\sin\theta\cos\theta \\ \sin^2\theta & \cos^2\theta & 2\sin\theta\cos\theta \\ \sin\theta\cos\theta & -\sin\theta\cos\theta & \cos^2\theta - \sin^2\theta \end{bmatrix} \quad (\text{D.38})$$

Strain-displacement relations

Equations showing the relationship between displacement and strain [1]:

$$\varepsilon_x = \frac{\partial u}{\partial x} \quad (\text{D.39})$$

$$\varepsilon_y = \frac{\partial v}{\partial y} \quad (\text{D.40})$$

$$\varepsilon_z = \frac{\partial w}{\partial z} \quad (\text{D.41})$$

$$\gamma_{xy} = \frac{\partial v}{\partial x} + \frac{\partial u}{\partial y} \quad (\text{D.42})$$

$$\gamma_{xz} = \frac{\partial w}{\partial x} + \frac{\partial u}{\partial z} \quad (\text{D.43})$$

$$\gamma_{yz} = \frac{\partial w}{\partial y} + \frac{\partial v}{\partial z} \quad (\text{D.44})$$

Appendix E

Calculations

Reaction Forces

Starting by defining the necessary reaction forces, that will be needed for both the welding calculations as well as the deflection calculations. For the worst case scenario, the force due to torque acts in the middle of the mandrel. The magnitude of the weight force will be located in the middle, this is because of the mandrel and its components symmetrical design, resulting in an even-distribution of weight throughout its entirety. From basic structural engineering principles, evenly distributed loads will always have its force magnitude centered.

$$R_A = R_B = \frac{F_y}{2} = \frac{W_{total} + F_{Torque}}{2} \quad (E.1)$$

Here, $R_A = R_B$, because the forces are acting in the center with supports evenly spaced on both sides. F_{Torque} is derived from the project specifications, in section 2.3, W_{total} is the total weight force of all the components except the winding adapters, calculated by taking the aluminium density, table A.3, the volume of the components, and the gravitational acceleration $g = 9.82m/s^2$. The winding adapters are excluded because they will work as supports for the mandrel and its components.

$$W_{total} = W_{Mandrel} + 2 \cdot W_{shaft} = 217N + 2 \cdot 20N = 257N \quad (E.2)$$

W_{Shaft} being the weight force of one shaft. $W_{Mandrel}$ being the weight force of the mandrel, the connector flanges, and the reduction liners. This gives

$$R_A = R_B = \frac{257 + 295}{2} = 276N \quad (E.3)$$

Deflection

There are multiple ways to calculate of displacement. For this particular calculation the curvature surface method will be used [10].

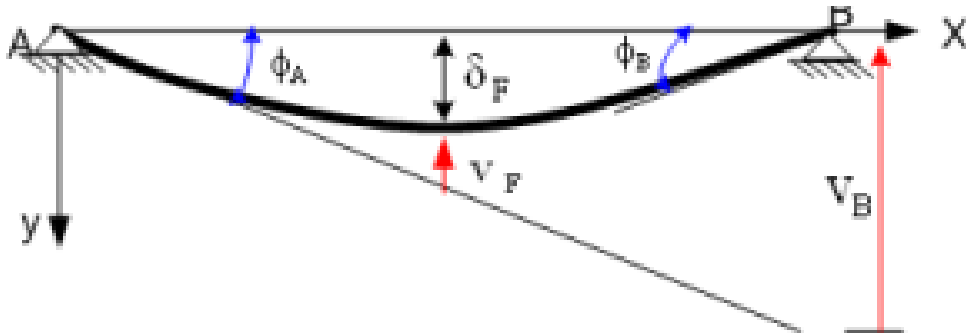


Figure E.1: Curvature surface method [10]

δ_F is the given deflection at specific points on the system, Figure E.1. Finding δ_F at the critical point will give us the largest deflection of the system [10]. This gives

$$\delta_F = \phi_A \cdot a - \nu_F \quad (E.4)$$

where and

$$\phi_A = \frac{\nu_B}{L} \quad (\text{E.5})$$

where a represents the point of deformation [10]. Max deformation will occur at the middle-point, $\frac{L}{2}$, as seen in Figure E.2. Calculating the maximum deformation using this, leads to

$$\delta_F = \frac{\nu_B \cdot L}{L \cdot 2} - \nu_F = \frac{\nu_B}{2} - \nu_F \quad (\text{E.6})$$

To find the max deflection δ_F at the critical point, a , is found through the use of the curvature diagram. Using the following formula

$$K(x) = \frac{M}{EI} \quad (\text{E.7})$$

From here, the inertias and moments must be calculated to establish the curvature diagram. Starting with finding the inertias I_i of the shafts and the mandrel [10],

$$I_1 = I_3 = \frac{\pi \cdot d_{shaft}^4}{64} = \frac{\pi \cdot 0.04^4}{64} 1.26 \cdot 10^{-7} m^4 \quad (\text{E.8})$$

where d_{shaft} is the diameter of the shaft, and I_1 and I_3 is the inertia of the shafts.

$$I_2 = \frac{\pi \cdot (d_{oMandrel}^4 - d_{iMandrel}^4)}{64} = \frac{\pi \cdot (0.15^4 - 0.14^4)}{64} = 5.99 \cdot 10^{-6} m^4 \quad (\text{E.9})$$

where $d_{oMandrel}$ is the outer diameter of the mandrel, $d_{iMandrel}$ is the inner diameter of the mandrel and I_2 is the inertia of the mandrel pipe .

By combining the inertia's with the modulus of elasticity E of the aluminium gives the following values:

$$E \cdot I_1 = E \cdot I_3 = 8.694 \cdot 10^3 Nm^2 \quad (\text{E.10})$$

$$E \cdot I_2 = 4.13 \cdot 10^5 Nm^2 \quad (\text{E.11})$$

where the modulus of elasticity E for the aluminium alloy 6081-T6 is $E = 69GPa$, see table A.3.

Constants

For further calculations some constants need to be introduced:

- The length of the mandrel is $L_{mandrel} = 3m$
- The length of the shaft is $L_{shaft} = 0.6m$
- The diameter of the shafts $d_{shaft} = 0.04m$
- The outer diameter of the mandrel is $d_{oMandrel} = 0.15m$
- The inner diameter of the mandrel is $d_{iMandrel} = 0.14m$.

Next step is to find the moments M_1 , M_2 and M_3 , see the moment diagram below, Figure E.2.

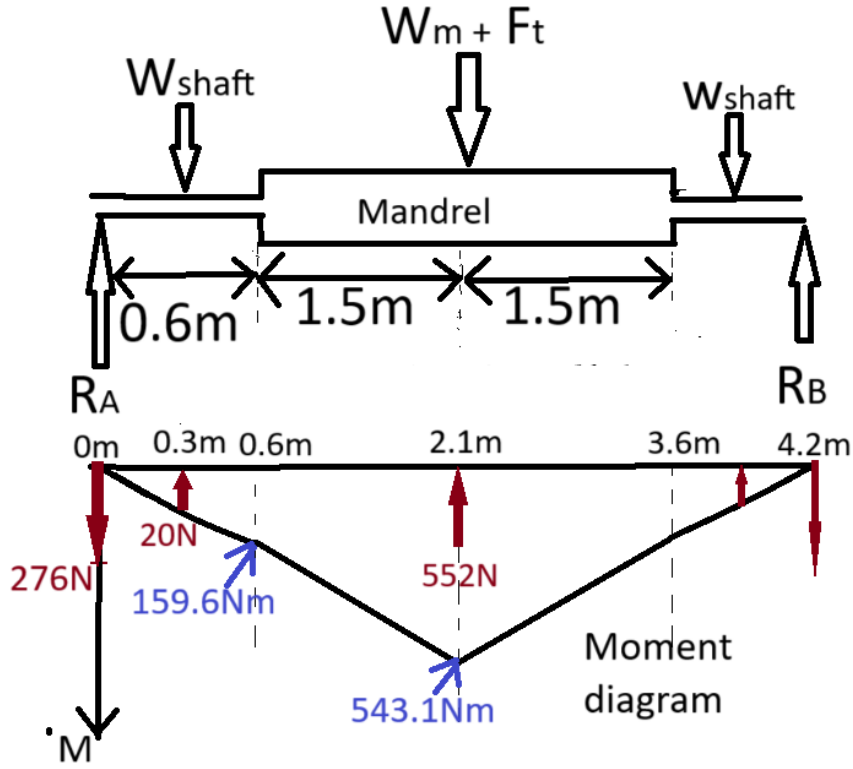


Figure E.2: Moment diagram

This gives

$$M_1 = M_3 = F_A \cdot L_{shaft} - W_{Shaft} \cdot \frac{L_{Shaft}}{2} = 159.6Nm \quad (E.12)$$

and

$$M_2 = R_A \cdot (L_{Shaft} + \frac{L_{mandrel}}{2}) - W_{shaft} \cdot (\frac{L_{shaft}}{2} + \frac{L_{mandrel}}{2}) = 543.1Nm \quad (E.13)$$

where R_A , W_{Shaft} , and $W_{mandrel}$ are given above. Using these moments M_i and the EI_i values, the curvature diagram $K(x)$ can be made using the previously mentioned equation [10],

$$K(x) = \frac{M}{EI} \quad (E.14)$$

This leads to

$$K_{11} = K_{33} = \frac{M_1}{E * I_1} = 1.84 * 10^{-2} \quad (E.15)$$

$$K_{12} = K_{23} = \frac{M_1}{E * I_2} = 3.86 * 10^{-4} \quad (E.16)$$

$$K_{22} = \frac{M_2}{E * I_2} = 1.31 * 10^{-3} \tag{E.17}$$

Plotting the diagram of these values gives us the needed information to find the angle of deflection θ , which is derived from the areas presented in the diagram below, Figure E.3. Marked as red dots are the locations of specific area centers in relation to the x-direction. The \bar{X}_i are the x distance from origo to to their respective Area center A_i . [10]

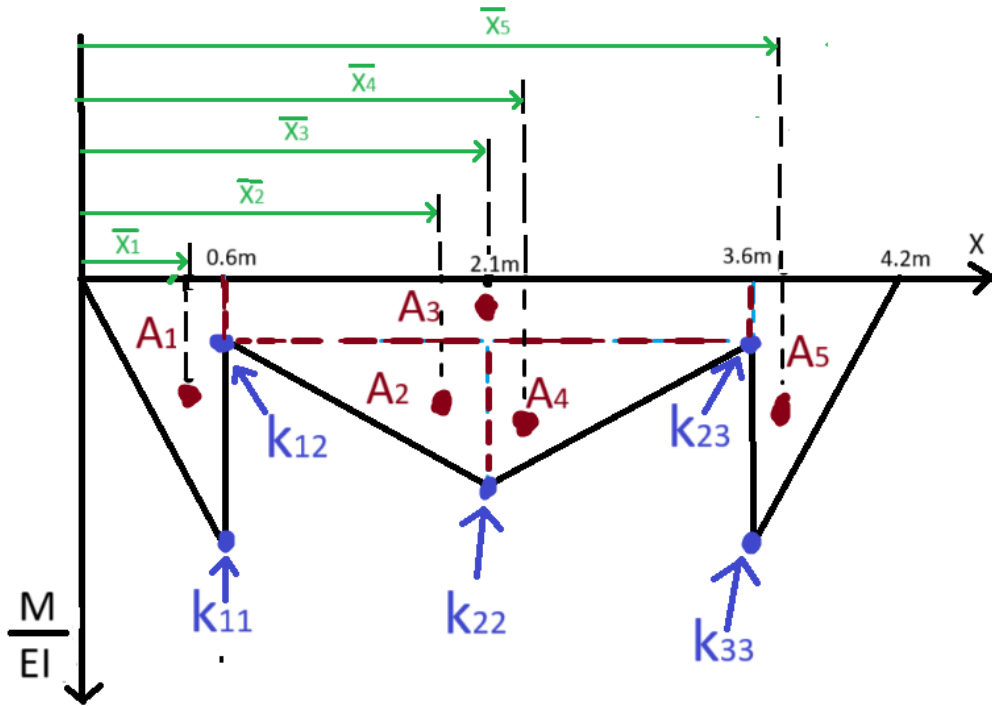


Figure E.3: Curvature diagram

To find δ_F , the values of ν_F and ν_B are needed, which can be derived from the following equation. [10]

$$\nu = \bar{x} * \theta \tag{E.18}$$

From this equation both \bar{x} and θ is needed, where θ is described in the following equation [10]:

$$\theta = \frac{1}{EI} \int_0^L M dx \tag{E.19}$$

According to the curvature surface method, these θ_i will be equal the areas A_i , found in the curvature diagram. From the curvature diagram, Figure E.3, it can be concluded that the following areas A_1, A_2, A_4, A_5 are of triangular shape, while the area A_3 is of a rectangular shape. This lets us find the areas A_i and therefore the angles θ_i by using simple geometry [10].

$$\theta_1 = \theta_5 = \frac{0.6 * K_{11}}{2} = 5.52 * 10^{-3} \tag{E.20}$$

$$\theta_2 = \theta_4 = 1.5 * \left(\frac{K_{22}}{2} - K_{12} \right) = 4.04 * 10^{-4} \quad (\text{E.21})$$

$$\theta_3 = 3 * K_{12} = 1.16 * 10^{-3} \quad (\text{E.22})$$

Using these values the \bar{x}_i can be found. This will be the x-distance from $x = 0$ to each respective area center, see Figure E.3. This leads to

$$\bar{x}_1 = \frac{2 * 0.6}{3} = 0.4m \quad (\text{E.23})$$

$$\bar{x}_2 = 0.6 + * \frac{2 * 1.5}{3} = 1.6m \quad (\text{E.24})$$

$$\bar{x}_3 = 0.6 + 1.5 = 2.1m \quad (\text{E.25})$$

$$\bar{x}_4 = 2.1 + \frac{1.5}{3} = 2.6m \quad (\text{E.26})$$

$$\bar{x}_5 = 3.6 + \frac{0.3}{3} = 3.7m \quad (\text{E.27})$$

With all \bar{x}_i and θ_i values ν can be found, by summing the values to get the total deflection that occurs on the system. By using the equation for ν , equation E.18, ν_B and ν_F can be defined as the area moment of the curvature surface at point B, and will be the area moment of the curvature surface about the load point F, respectively [10]. This leads to the equations

$$\nu_B = \sum_{i=1}^4 \theta_i * \bar{x}_i = 6.34 * 10^{-3}m \quad (\text{E.28})$$

$$\nu_F = \sum_{i=2}^4 \theta_i * \bar{x}_i = 1.70 * 10^{-3}m \quad (\text{E.29})$$

Using the formula from earlier, equation E.6, the maximum deflection at point "a" can be calculated.[10]

$$\delta_F = \frac{\nu_B}{2} - \nu_F = 1.47 * 10^{-3}m = 1.47mm \quad (\text{E.30})$$

According to these calculations, the total deflection on the system is 1.47 mm located in the center of the mandrel, which is within the permissible limits.

Welds

In this section, the welds on the mandrel will be calculated.

Reduction liner mandrel weld

Due to the uncertainty of the exact axial force applied from the extraction tool, a guesstimate was made defining it as 12kN. The bending moment are calculated from the weight load located in the middle of the pipe, 1.5 meters, from the weld. The weld will take the form of the complete circumference around the reduction liner, as seen in Figure C.3. The following equations is employed to calculate the weld strength [15],

$$A = 1.414 * \pi * h * r \quad (\text{E.31})$$

A is the area of the weld, where h is the height and r is the radius of the weld. Further on, the moment of inertia is needed, using the following formula

$$I = 0.707 * h * I_u \quad (\text{E.32})$$

where

$$I_u = \pi * r^3 \quad (\text{E.33})$$

The formulas above into can be used in the the welding stress equations like this [15]:

$$\tau' = \frac{F_a}{A} \quad (\text{E.34})$$

$$\tau'' = \frac{M * r}{I} \quad (\text{E.35})$$

$$\tau = \sqrt{(\tau')^2 + 3 * (\tau'')^2} \quad (\text{E.36})$$

Because the welds are uniformly spaced from center, the reactions forces will remain the same as found earlier in section E.1.

$$M = M_{bending} = R_A * \frac{L}{2} \quad (\text{E.37})$$

where $L = 3m$ is the length of the mandrel. Using equations E.31 - E.36, with $h = 4mm$ and $r = 70mm$, yields the following:

$$\tau' = \frac{12000}{1.414 * \pi * 4 * 70} = 9.65MPa \quad (\text{E.38})$$

$$\tau'' = \frac{276 * 1500 * 70}{0.707 * 4 * (\pi * 70^3)} = 9.51MPa \quad (\text{E.39})$$

$$\tau = \sqrt{9.65^2 + 3 * 9.51^2} = 19.09MPa \quad (\text{E.40})$$

The result shows that the resulting stress that occurs on the weld is $19.09MPa$. According to [15], the weld following criteria must be upheld for the weld to be satisfactory, $\tau < 0.3S_{ut}$ and $\tau < 0.4S_y$. Using the following values $S_{ut} = 295MPa$ and $S_y = 240MPa$, from table A.3, leads to the values $0.3S_{ut} = 88.5MPa$ and $0.4S_y = 96MPa$. Since the criterias are upheld, the weld is within the permissible limit and therefore safe.

Connector flange weld

Considering the weld on the connector flange, seen in Figure C.7, the axial force applied from the extraction tool won't affect this part due to being applied after the winding process. The relevant forces on this weld is the reaction force due to the torque applied on the mandrel and the weight force of the system given as R_A or R_B , calculated in section E.1. The form of this weld will be the same as for the weld reduction liner to mandrel weld, in the previous section leading to the same equations, E.31 - E.36. Using these formulas with the values $r = 20, h = 10, R_B = R_A = 276$ and $M = 276 * 1500$ yields, [15]

$$\tau' \approx 0MPa \quad (E.41)$$

$$\tau'' = \frac{276 * 1500 * 20}{0.707 * 10 * (\pi * 20^3)} = 46.60MPa \quad (E.42)$$

$$\tau = \tau'' = 46.60MPa \quad (E.43)$$

Using the same criteria as for the Reduction liner mandrel weld, it is clear that this weld is also within the permissible limits and therefore safe.

Tensile capacity of the extraction tool bolts

The tensile capacity of the bolts is calculated by using the yield strength R_e of the bolts specific strength class, as well as their specific tension area A_s . For the strength class 4.8, yield strength $R_e = 320MPa$, and for M10 bolts tension area $A_s = 58mm$. which leads to the following tensile capacity [10]

$$R_e * A_s = 18.56KN \quad (E.44)$$